Università degli studi di parma
dipartimento di fisica e scienze della terra

Hydrogen storage in light alkali-cluster intercalated fullerides

A thesis submitted for the degree of Ph.D. in Physics

Supervisor: Prof. Mauro Riccò
Coordinator: Prof. Pier Paolo Lottici

XXVI CICLO - January 2014

AUTHOR'S ADDRESS

Mattia Gaboardi

Dipartimento di Fisica e Scienze della Terra

Università degli Studi di Parma

Parco Area delle Scienze, via G.P. Usberti 7/A

I-43124 Parma, Italy.

E-mail: *mattiagianandrea.gaboardi@fis.unipr.it*

Hell, there are no rules here - we're trying to accomplish something

Thomas A. Edison

Contents

Chapter 1

Introduction

The fossil fuels depletion combined to greenhouse effect (caused by increasing emissions of CO_2) are two basic factors to face up for a sustainable future. A significant breakthrough was made thanks to common renewable resources although the effect they have on the economy is still small. In this context, hydrogen would represent an ideal substitute of fossil fuels: it will not be the answer to the energy problem (at least not alone), but it could definitely solve the problems related to environmental pollution.

1.1 Hydrogen storage

Hydrogen is the element with the lowest mass and size and with the highest diffusion coefficient ($D \sim 1.285$ cm^{2}s^{-1}). It is also the most abundant substance in the Universe. It has the $1s^1$ electronic configuration when it is in form of atom but the first shell can be filled with 2 electrons and this allows four different processes:

- formation of H^+ by donation of its valency electron (*e.g.*: HCl, HF);
- formation of the hydride ion H^- by accepting one electron (as in NaH, CaH_2);
- sharing its valency electron to form a covalent bond (*e.g.*: H_2, H_2O, hydrocarbons);

- ≻ share the electron to an ensemble of atoms forming a metallic bond H^0 (like in PdH_x, NiH_x).

The hydrogen covalent bond is one of the most stable present in nature. The average dissociation energy for H_2 is ∼428.2 kJ/mol (4.438 eV) and for this reason the molecular hydrogen is the stable form of this element on the Earth, although is most commonly present in molecular form bound to other elements. Free molecular hydrogen, in fact, does not occur naturally in quantity (only 0.55 ppm by volume in the atmosphere), but can be generated with different methods (mainly from steam reformation of hydrocarbons and water electrolysis). When the hydrogen reacts with oxygen a combustion occurs, with the reaction:

$$H_2(g) + \frac{1}{2}O_2(g) \longrightarrow H_2O(l) + 286 \text{ kJ } (\sim 2.96\ eV).$$

The great heat released in this process can be utilized as energy source. On this point of view, hydrogen has to be considered as an energy carrier, rather than an energy source (as in the case of nuclear fusion). The use of hydrogen as an energy vector falls within the context of the so-called "hydrogen economy". In this context, of prominent relevance would be the use of hydrogen as fuel for the automotive industry, as a substitute of petroleum and derivatives: thanks to its "green" emissions (free of CO_2 and NO_x), upon the combustion in air, and its relatively easy production (from water electrolysis, fossil sources, biomass), with low environmental impact. In fact, the major fossil fuel dependence in western economies is for transport. Unfortunately, one of the greatest obstacles to the adoption of hydrogen as a fossil fuel replacement is related to its volumetric density. If compared with other substances, the hydrogen stands out for its remarkable energy density by mass (141.86 MJ/kg, about 3 times the one of gasoline, Diesel or propane). On the contrary, as often happens, things seem to be too good to be true and the downside is that the volumetric energy density is one of the lowest (*e.g.*: 4.5 MJ/L for H_2 compressed at 690 bar at 15 °C and about 8.5 MJ/L for the liquid, respect to about 34.2 MJ/L for gasoline). In Fig. 1.1 various substances are displayed as a function of the energy density obtainable from

their characteristic reaction (chemical, electrochemical, electrical) with external components. Because of its poor volumetric energy density, the use

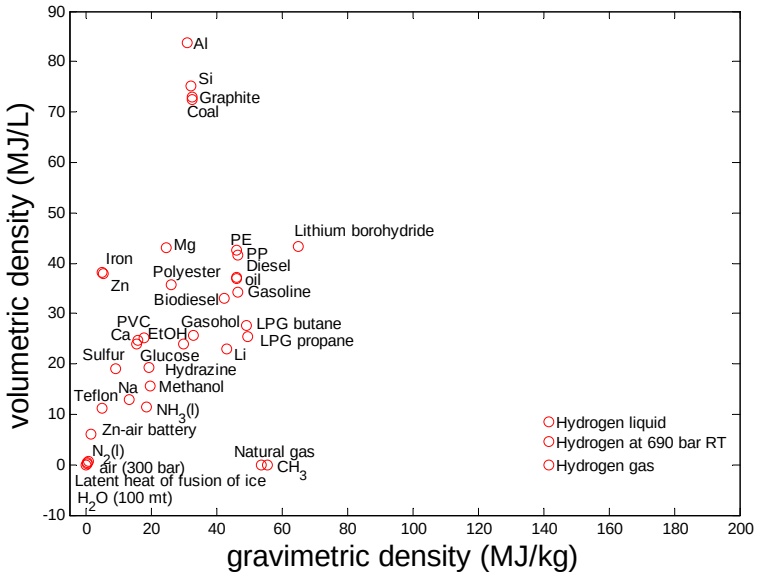

Figure 1.1: Energy densities of systems that require external components, such as oxidizers or a heat sink or source. These figures do not take into account the mass and volume of the required components as they are assumed to be freely available and present in the atmosphere.

of hydrogen as fuel in the automotive industry has to be accompanied by a clever storage. In its gaseous form is practically useless and the only way to achieve a performance efficiency comparable to that of a petrol-powered vehicle is to increase its density. Practically speaking, about 8 kg of H_2 would be necessary for a family saloon to achieve a range of 400 km [1] (4 kg for an electric car with a fuel cell), while the same distance would be covered with about 24 kg of petrol in a combustion engine. The problem is that 4 kg of H_2 at room temperature and room pressure would occupies about 45 m^3 of volume (in terms of size more than a weather balloon), so that it will hardly fits the vehicle's storage system. The easiest way to reduce this volume is by compressing the gas. Novel carbon-fiber high pressure tanks are tested to resist up to 600 bar and can be filled up to 450 bar for regular use but

they have to be protected in the inner surface by special coating in order to prevent reaction between the gas and the polymer. Aluminum (light and inert) is commonly used for methane's store systems and can be adopted also for H_2. In this way is technically possible to achieve 4 % hydrogen stored by mass, but there would be some issues to overcome: for example the problem of pressure dropping from 450 bar to zero overpressure, so that an additional pressure control is essential. Moreover, the risk arising to a high pressure system is a matter to be taken into account in terms of safety. A second opportunity is given by the condensation of H_2 into liquid form. At its boiling point the hydrogen density becomes 70.8 kg/m^3. However, the condensation temperature at room pressure is rather prohibitive (-252 °C) due to the expensive cooling system necessary to keep hydrogen as liquid. Furthermore, the enthalpy of vaporization at the boiling point amounts to 452 kJ/kg thus the heat transfer through the container leads directly to the loss of hydrogen.

Actually, the most promising system is the hydrogen storage in solid and liquid materials. Hydrocarbons contain large amounts of chemically bound hydrogen and are available in liquid and solid form: cyclohexane (C_6H_{12}), for example, can reversibly desorb 7.1 mass% H_2 forming benzene (C_6H_6). Of course, the health and environmental risks associated to this substance make it inadvisable to use. On the other hand, an inorganic system like NH_3 is able to store 5.9 mass% H_2, although its corrosive nature does not makes it attractive for applications. Of great relevance is the hydrogen storage in metal hydrides, many of them capable to reversibly absorb and desorb large amounts of the gas. In this field several materials have been investigated by the "hydrogen community": metal hydrides, mixed metal hydrides, light metal borohydrides and alanates.

The U.S. Department of Energy (DoE) imposed clear targets for mobile application within 2015 [2]:

- a gravimetric capacity of 5.5 mass% hydrogen for the tank, in order to achieve system-level capacities of 1.8 kWh/kg system,
- a volumetric capacity if 0.040 kg hydrogen/L (1.3 kWh/L ∼4.7 MJ/L),

and the ultimate targets of 2.5 kWh/kg system (7.5 wt.% hydrogen) and 2.3 kWh/L (∼8.3 MJ/L, 70 g/L of hydrogen) for the long-therm period. The overall storage system must also comply all the problems concerning fast kinetics of hydrogen charge and discharge and cyclability. At the current state of the art no system fully satisfies all of these requirements. The lighter metal hydrides LiH or MgH_2 can easily absorb about 12.7 and 7.7 mass% H_2 respectively, but the kinetics of absorption/desorption is very slow and high temperatures are necessary to overcome the energy barrier required to dissociates the hydrogen molecule on the surfaces of Li and Mg. For those reasons, alanates are preferable because of their relatively mild

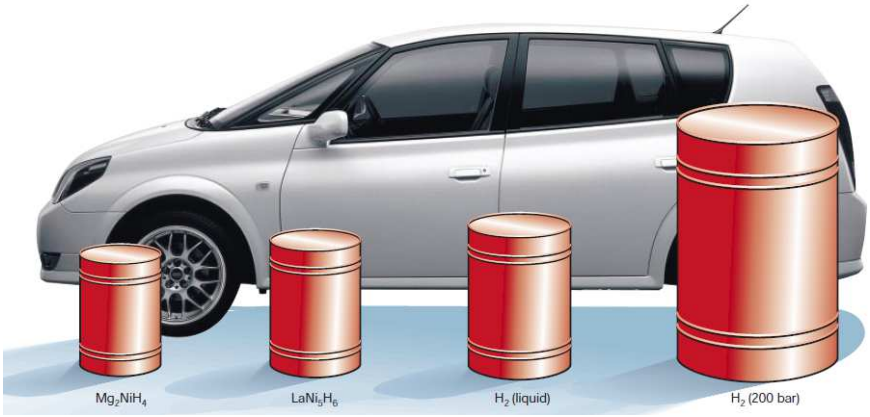

Figure 1.2: Volume of 4 kg of hydrogen compacted in different ways, with size relative to the size of a car [3].

condition of hydrogenation (de-hydrogenation) [4]. The most studied are, for example, $NaAlH_4$ (which decomposes in 2 steps forming $Al+NaH+\frac{1}{2}H_2$ and desorbing 5.6 mass% of hydrogen [5]), $LiAlH_4$ (about 7.9 mass% H_2 desorbed in two steps through formation of LiH [6]), $Mg(AlH_4)_2$ (about 6.6 mass% H_2 released in the first step at 163 °C through production of MgH_2, which can subsequently decomposes at 380 °C leading to a total of 9.3 mass% [7]). $LiBH_4$ can reversibly store 8-10 mass% hydrogen at 300 °C (100 bar) [8] but is a very expensive compound. Materials such as intermetallic hydrides like $LaNi_5H_6$ (1.37 mass% H_2 at 298 K), TiV_2H_4 (2.6 mass% H_2 at 313 K)

have also been considered for hydrogen storage applications. These materials possess in general low gravimetric energy density but high energy density by volume.

All the above mentioned compounds exhibits a peculiar behavior: they store hydrogen by means of a more or less strong chemical interaction, or chemisorption (except in the case of intermetallic hydrides in which hydrogen is in neutral form). Another approach consists on physisorption: porous systems such as clathrates [9], carbon nanostructures (nanofibers, carbon nanotubes, activated carbon) [10], zeolites [11] and Metal-Organic Frameworks (MOFs [12]) are a widely studied class of materials. In all these compounds the interplay between the specific surface area and porosity is of fundamental importance in determining the ability to adsorb hydrogen. Generally, the adsorption in these materials occurs at low temperature (liquid nitrogen) and relatively low pressure of hydrogen and they desorb at room temperature or slightly above. It is the variation of attractive surface

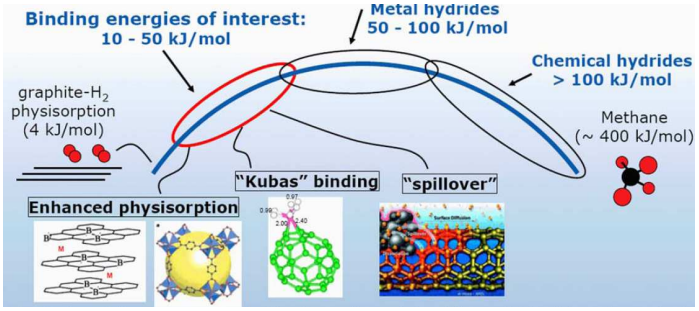

Figure 1.3: Overview of the binding energies for different hydrogen storage materials [10].

forces as a function of distance from the surface which decides whether physisorption or chemisorption takes place. In the former case the hydrogen remains as a molecule and its electronic structure is barely perturbed upon adsorption, leaving intact the surface. The fundamental interaction which drives this process are the van der Waals forces and the interaction energy is usually in the order of 10-100 meV (1-10 kJ/mol). In contrast, when chemisorption occurs, a chemical reaction between the adsorbate and the

surface leads to the generation of new chemical bonds. In this type of sorption the energies involved are generally greater than 0.5 eV (>50 kJ/mol). In Fig. 1.3 the landscape of possible interactions is depicted. Energetically speaking, the useful range for a good hydrogen storage material is 10-50 kJ/mol, which is, in some way, borderline between physisorption and chemisorption. In this region two are the most considered processes which could take place between hydrogen and the ad/absorber:

- ≻ Kubas interaction
- ≻ Spillover effect

A deepening of these processes will be given in the following paragraphs.

1.1.1 Kubas Binding

The so called Kubas interaction draws its name from a famous article of Gregory Kubas [13]. The process involves a transition metal (M) and a hydrogen molecule and results in the formation of a dihydrogen complex. In its simplest sense it is a three center 2-electron bond in which a molecule of H_2 acts as a two electron sigma donor to the metal center. A typical dihydrogen complex is formed in the second step of the subsequent reaction:

$$L_nM + H\text{—}H \rightleftharpoons L_nM \longleftarrow \begin{matrix} H \\ \vdots \\ H \end{matrix} \rightleftharpoons L_nMH_2, \tag{1.1}$$

where L_n represents one or more ligands (such as CO, Cl or phosphine) attached to M. The Kubas binding occurs before a typical oxidative addition to form a metal hydride (third step eq. 1.1): the hydrogen molecule thus acts as a neutral σ-donor. The electrons donated by the ligands and occupying one of the filled atomic d-orbitals on M are donated to the σ^*-molecular orbitals (MO) of H_2 and back-donated on the unoccupied metal's orbitals, forming an η^2-complex. The H—H bond is stretched about 20 % over its value in free H_2 (0.74 Å). The process is similar to the Dewar

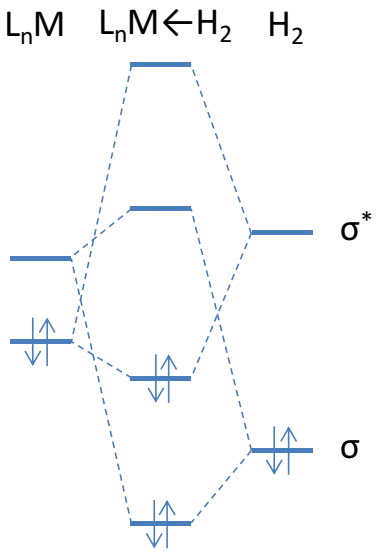

Figure 1.4: MO scheme showing the interaction between the frontier orbitals of H_2 and an metal fragment, adapted from [14]. One of the occupied and one of the unoccupied AO of metal hybridises the LUMO and the HOMO of H_2. An intermediate state is stabilized in energy.

coordination of olefines with metals, in which the retrodative donation of electrons from a filled metal d-orbital to the π^*-orbitals of a $C{=}C$ bond link a π molecule (such as CH_2CH_2) to the metal. A review of this interaction in organometallic compounds can be found here [15].

1.1.2 Spillover effect

The tendency of transition metal atoms to cluster makes, in some cases, the Kubas effect hard to produce in many compounds. However, the formation of metallic nanostructures can lead to the formation of a different mechanism. The spillover effect was first studied by Khoobiar on Pt/Al_2O_3 (0.5 wt.% Pt) catalyst [16]. To take place, this mechanism needs a metal particle (for example a clusters of few atoms of Pt, Pd or Ni), which has to be dispersed upon an inert support (receptor or carrier). The real absorber is the receptor surface while the metal particle has the role of dissociating

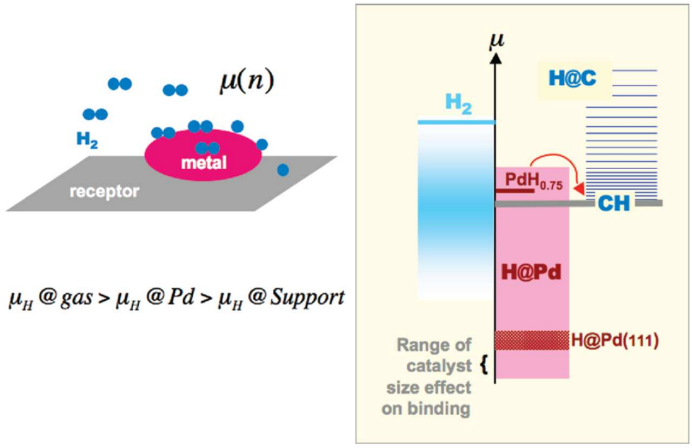

Figure 1.5: Left: schematics of spillover process in real space. The inequality shows the range of chemical potential H favorable for spillover. Right: model of spillover in energy space for Pt supported on graphene. The relative energy (chemical potential) of hydrogen is displayed in different states. The gray, dark-red, and blue lines show the H in fully hydrogenated graphene (CH), in metal hydride ($PdH_{0.75}$), and in the H_2 molecule, respectively. The pink and dark-red blocks show the range of energies of H at the catalyst and at the $Pd(111)$ surface with the H coverage varying form 25 to 100 %. The family of thin dark-blue lines corresponds to the energies of H bound to graphene. From [17].

the incoming hydrogen molecules. The process can only work if the carrier is able to allow the diffusion of hydrogen chemisorbed on its surface. The metal has the role of lowering the energy pathway for gaseous species which are firstly adsorbed by it and then diffuse on the plane of the carrier. Thanks to diffusion of atomic hydrogen onto the carrier surface, the metal particle is always virtually free to continuously split new H_2 molecules. If one consider the hydrogen chemisorption process, let assume that n_M is the total number of metal atoms forming the cluster, $n_{M(s)}$ the number of surface metal atoms and n_H the number of chemisorbed hydrogen atoms: the n_H/n_M ratio is given by:

$$\frac{n_H}{n_M} = \frac{n_H}{n_{M(s)}} \cdot \frac{n_{M(s)}}{n_M},$$

which allows one to calculate the crystallite size or metal cluster area knowing the value of $n_H/n_{M(s)}$. It is commonly accepted that hydrogen spillover occurs whenever the n_H/n_M ratio for a supported metal being grater than that exhibited by the same metal in the unsupported state (and having the same particle size). Since this comparison is virtually impossible, usually the spillover reasonably occurs when the n_H/n_M ratio for the supported metal exceeds the $n_H/n_{M(s)}$ value for the unsupported metal [18]:

$$(n_H/n_M)_{supported} > \left(n_H/n_{M(s)}\right)_{free}.$$

For example, unsupported platinum catalyst at different temperatures and hydrogen pressure have always a value of $n_H/n_{Pt(s)} \lesssim 1$ [19], while Boudart *et al.*, found a maximum value of n_H/n_M of 75 for platinized carbon [20].

Up to now only the hydrogen chemisorption was considered. Actually, many catalysts are capable of absorbing relatively large amounts of atomic hydrogen to form a non-stoichiometric hydride (for example, Pd is known to form α and β hydrides). Singh *et al.* studied the hydrogen spillover in terms of thermodynamics for small clusters of Pd and Ni on graphene receptor [17]. In Fig. 1.5 a conceptual diagram of spillover is reported. The process is energetically favored when the chemical potential of hydrogen on the receptor is lower than the same in the metal and in its gaseous state. In order to achieve this condition the hydrogen has to almost saturate the metal particle: the first incoming hydrogen molecules is dissociated by the metal forming an hydride cluster (*e.g.*: Pd_4H_2). The subsequent H_2 addition do not fully dissociates the molecule, but rather bind to PdH_x via Kubas interaction until saturation. At this point, any further H_2 is energetically unstable upon adsorption on PdH_x and is favored to migrate to the graphene receptor.

1.2 Fullerides

1.2.1 The fullerene molecule (C_{60})

Fullerene C_{60} was first discovered by Harold Kroto *et al.* [21] in 1985 studying the formation of long carbon chains in the interstellar space. The name fullerene (or buckyball) comes from the the name of the architect Buckminster Fuller, whose geodesic domes resembles the shape of the molecule. The structure can be ascribed by a truncated icosahedron (I_h point group symmetry) made of 20 hexagons and 12 pentagons of carbon atoms (each pentagon is surrounded by 5 hexagons). The van der Waals (v.d.W.) diameter of the molecule is about 1.1 nm while 0.71 nm is the nucleus to nucleus diameter. The average carbon to carbon bond length is about 1.4 Å and

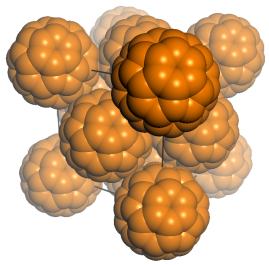

Figure 1.6: Schematic representation of the *fcc* structure of C_{60} fulleride.

can be considered a double bond. The electronic state of carbon on C_{60} is a mixture of sp^2 and sp^3 hybridized orbitals: each C atom is bound to 3 other carbons and its p_z orbital owns a dangling bond for which the electron density is pronounced toward the external surface (although the electronic wave functions of the molecular orbitals slightly extend also inside the sphere). Whereas the C-C bond length in sp^2-hybridised carbon is $\sim$1.42 Å (*e.g.*: in graphite) while it is $\sim$1.54 Å for sp^3-hybridised carbon (*e.g.*: in diamond), in C_{60} there are two kinds of bond length: the edges shared by 2 hexagons are in the order of 1.46 Å while the those between an hexagon and a pentagon are around 1.40 Å. For the sake of simplicity, the longer bond-length is generally considered a single σ bond and the shortest a π double bond, although this may be an oversimplified assumption.

C_{60} can be synthesized from graphite through arc-discharge in inert atmosphere. This process generates a soot of carbon allotropes for which C_{60} is the most abundant species (∼80 %) [22] and can be easily separated through chromatography. Fullerene exists as a black crystalline solid (fullerite), ordered in the $Fm\overline{3}m$ spatial group ($a = 14.17(1)$ Å at 300 K, $d_{C_{60}-C_{60}} \simeq 10.2$ Å) [23, 24]. The asymmetric unit, centered in the $4a$ Wyckoff site (000), is orientationally disordered among different positions and for this reason fullerite is a plastic crystal. This structure presents large octahedral (O_h) and tetrahedral (T_h) voids. The rotational disorder is significantly lowered below 260 K, where the crystal undergoes a first order transition and the symmetry is reduced to simple cubic (sc) with $Pa\overline{3}$ spatial group ($a = 14.04(1)$ Å at 11 K) [23]. Since there are two different ways of placing a fullerene into a cubic environment which preserves the same number of symmetry operations, the low temperature phase can be understood by thinking a *fcc* arrangement of C_{60} wherein neighbouring molecules are still in motion, but the rotational axes lie along different [111] directions. Moreover, below about 90 K all the rotations are entirely frozen, although the merohedral disorder can be still present [25]. Some important properties of C_{60} are reported in table 1.1. In its molecular form, C_{60} owns a high grade of degeneracy in its molecular

average C-C distance	1.44 Å
C_{60} mean diameter	6.86 Å
C_{60} outer v.d.W. diameter	11.18 Å
C_{60} inner v.d.W. diameter	3.48 Å
1^{st} ionization potential	7.58 eV
2^{nd} ionization potential	11.5 eV
electron affinity	2.65 eV
fcc lattice constant (300 K)	14.17 Å
fullerite density	1.72 g/cm^3
O_h site radius	2.07 Å
T_h site radius	1.12 Å
thermal expansion	$6.2 \cdot 10^{-5}$ cm^3/K
Band gap	1.6 eV

Table 1.1: Main physical properties of C_{60} molecule and crystal.

orbital states, due to the high grade of symmetry. This high degeneracy is also reflected in the electronic structure. C_{60} orbitals are schematized in Fig. 1.7. In the ground state, the 60 valence electrons are localized on only 7 energy states. The h_u level ($l = 5$) is completely filled by the ten remaining electrons, becoming the highest occupied molecular orbital (HOMO), and the t_{1u} levels become the lowest unoccupied molecular orbitals (LUMO), while the LUMO+1 levels have t_{1g} symmetry. The HOMO-LUMO gap is about 2 eV. The molecular character is in some way preserved also in the

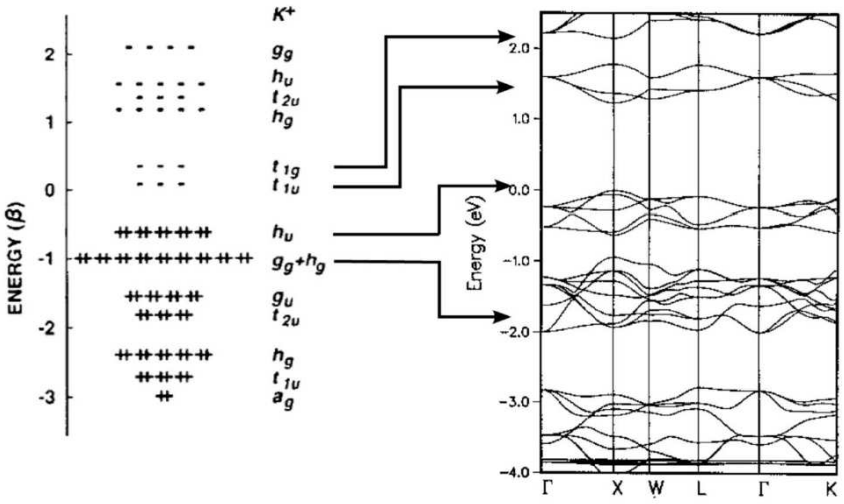

Figure 1.7: Left: scheme of the molecular orbitals of C_{60}, as calculated by Hückel model with the relative degeneracy and symmetry. Right: derived electronic band structure in the *fcc* fullerite crystal. From [26].

crystal fullerite, where the overlap of the π orbitals broadens the levels to bands (Fig. 1.7). The HOMO-LUMO band gap is ∼1.5 eV [27].

1.2.2 The alkali intercalated fullerides

The ability of C_{60} to easily accept electrons on its LUMO orbitals is widely exploited in the synthesis of charge transfer salts (or *fullerides*). It is well known that the molecule can receive up to 6 electrons on its t_{1u}-LUMO levels [28, 29, 30]. Moreover, the large intermolecular space in the *fcc* structure

allows the diffusion of ionic species, such as alkali and alkaline earth metals (*e.g.*: *Li*, *Na*, *K*, *Rb*, *Cs*, *Ca*, *Mg*, *Sr* and *Ba*), exohedrally to C_{60}. Much harder is rather the doping with transition metals, such as *Ti*, *V*, *Fe*, *Co*, *Ni*, *Hg*, *Pt* and *Pd*, due to the high cohesive energy of these elements and the poor tendency to donate their charge to C_{60} [31, 32, 33, 34, 35, 36, 37]: in these cases the synthesized solids are often amorphous or polymeric. Fullerides of rare earths have also been synthesized but up to now remain of purely fundamental interest [38, 39, 40]. A wide variety of intercalated fullerides were synthesized since the discovery of C_{60}, with interesting applications, for example in superconductivity [65] and energy storage [51, 66]. Whereas the undoped fullerite is a semiconductor, when it is doped with electron donor atoms the conduction bands are progressively filled leading to the formation of metallic and insulating phases. Of particular interest for the purposes of this thesis are the alkali intercalated fullerides, M_xC_{60} (M = *Li*, *Na*, *K*, *Rb*, *Cs*), whose main properties are summarized in Table 1.2 (in Fig. 1.8 the structure is schematized). This class of intercalated compounds was widely studied in the last 25 years. The so called A_3C_{60} (A = *K*, *Rb*, *Cs*) are known to be type-II metallic superconductors at relatively high critical temperature (T_c ∼18, 28 and 38 K respectively) and crystallize in a *fcc* system. The A_4C_{60} and A_6C_{60} crystallize in a *bco* and *bcc* lattice respectively and are small band-gap semiconductors [47]. Li_xC_{60} and Na_xC_{60} systems deserve a brief deepening, due to their different behavior and since they are topic of this thesis. Lithium and sodium are the smallest alkali metals and this allows a relatively easy intercalation in the fullerite lattice. Unlike the A_xC_{60}, their phase diagrams are not well defined and the originated phases often depend on the adopted method of synthesis. Moreover, the Li_xC_{60} and Na_xC_{60} are the only known alkali fullerides that permit the existence of small "metallic" clusters in the *fcc* fullerite lattice, for a high grade of stoichiometry (typically $x \geq 6$). The NaC_{60}, Na_2C_{60} and Na_3C_{60}, synthesized by vapour phase deposition of Na on C_{60}, are diamagnetics and present a *fcc* structure with absence of superconductivity in the Na_3C_{60} phase [63]. Na_4C_{60} and Li_4C_{60} are isostructural and crystallize in a *bco* lattice (space group $I2/m$) forming a polimeric crystals in which fullerenes produce a 2-

fullerite	stoichiometry	lattice	remarks
C_{60}	$x = 0$	*sc* / *fcc*	order-disorder (260 K) [23]
A_xC_{60}	$1 < x < 3$	*fcc* / *bco* / polymer	[41, 42, 43, 44, 45]
	$x = 3$	*fcc*	type − II superconductors, merohedral disorder (except *Cs*) [46, 44]
	$x = 4$	*bct*	semiconductors [44, 47]
	$x = 6$	*bcc*	semiconductors [48, 44, 47]
Li_xC_{60}	$x < 4$	*fcc*	merohedral disorder [49]
	$x = 4$	polymer / *fcc*	super − ionic conductor polymer − monomer transition [50, 51, 52]
	$x > 5$	polymer + *fcc*	*Li* clusters [53, 54, 55, 56]
Na_xC_{60}	$x < 4$	*fcc*	merohedral disorder[57, 58, 59]
	$x = 4$	*fcc* / *bct*	polymer-monomer transition[60, 61, 62]
	$4 < x < 11$	*fcc* / *hex*	orientational order, *Na* clusters [58, 63, 59, 64]

Table 1.2: Some properties of alkali intercalated fullerides.

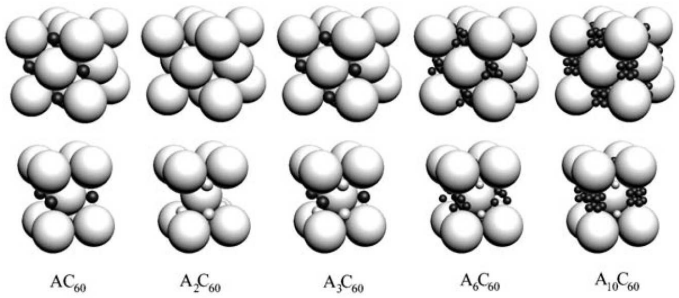

Figure 1.8: Structure of alkali-doped C_{60} compounds derived from the *fcc* structure of undoped C_{60}. The upper and lower rows display identical structures in terms of a cubic and a tetragonal unit cell, respectively, for better view. A_3C_{60} is made with K, Rb and with a mixture of Cs and other alkali metals, so that the Cs occupies the octahedral sites (black atoms). From [25].

dimensional array of molecules linked together by covalent bindings between sp^3-hybridised carbons. The alkali ions reside in the pseudo-octahedral and pseudo-tetrahedral voids of the lattice [60, 52]. In particular, Li_4C_{60} displays a typical super-ionic behavior with possible applications as a solid electrolyte in lithium-ion batteries [51]. For $x > 4$ the issue becomes more complex: C_{60} can virtually accept up to 6 electrons in its t_{1u} LUMO and 6 others in the t_{1g} LUMO+1 states, for a total of 12 electrons. Anyhow, such a large charge transfer is hardly feasible in the solid state and only the t_{1u} orbitals are actually occupied (although rare cases of t_{1g} occupied orbitals have been reported [67, 68, 69, 70]). This causes the alkali metal to partially donates its charge onto the C_{60} molecule yielding to the formation of alkaline clusters in the octahedral voids of the *fcc* lattice. Such alkali cluster intercalated fullerides present diamagnetic behavior (usually 6 electrons fill the t_{1u} orbitals bringing to a singlet ground state) [55]. If only the $T_h(\frac{1}{4}\frac{1}{4}\frac{1}{4})$ and $O_h(\frac{1}{2}\frac{1}{2}\frac{1}{2})$ voids of the *fcc* fullerite were completely filled by, for example, an alkali ion (M^+), the maximum theoretical stoichiometry will be M_3C_{60}. For this reason the lattices of A_4C_{60} and A_6C_{60} ($A = K$, Rb, Cs) are respectively *bct* and *bcc* (the body centered system can in principle accommodate up to 12 ions, depending on their radius). However, in the case

of Li and Na, the small ionic radius of these elements allows to fill the octahedral voids of *fcc*-C_{60} with more than one atoms. For example, Na is small enough for more than one of it to fit into the *fcc* O_h site and Na_6C_{60} and $Na_{11}C_{60}$were made [59, 64]. Lithium is also smaller and Li_xC_{60} compounds were synthesized with $x = 12$, 15, 28 without segregating the element from C_{60} [71, 72, 53]. In the past, it has been suggested that lithium can forms a cubic cluster in the O_h void, with both the body and the faces centered by other Li ions/atoms occupying partially or completely the $32f$ (xxx), $4b$ $(\frac{1}{2}\frac{1}{2}\frac{1}{2})$ and 24e $(\frac{1}{2}\frac{1}{2}y)$ sites of the $Fm\bar{3}m$ lattice respectively. This allows a maximum of $x = 17$ Li for Li_xC_{60}. Nevertheless, different structures could be generated when $x > 17$.

1.3 Hydrogen storage in fullerene and fullerides

Carbon nanostructures were widely studied in the past as an alternative to commons hydrogen storage materials. The reason is mainly to be found in the attractive properties of these system: carbon is abundant, cheap and relatively light element. It can be synthesized in different allotropes (*e.g.*: diamond, graphite, graphene, carbon nanotubes, fullerenes, onions, nanohorns) and easily interacts with hydrogen forming hydrocarbons. In particular, carbon nanotubes seemed to be the answer to the hydrogen storage problem when Northwestern University group found more than 60 mass% of H_2 in specific carbon fibers [73]. "Long story short, we hear a story too good to be true – it ain't", in fact, this fantastic result has never been reproduced anymore and was probably originated by experimental errors. A more reliable study has allowed to establish an empirical law for hydrogen adsorption on carbon based materials: 1.5 mass% H_2 per 1000 m^2/g of specific surface area [3], although during this work it was demonstrated that transition metal nanoparticles can improve the adsorption on graphene outside of this scheme [74]. This is true, in general, for the physisorption.

The binding energy of hydrogen molecule to carbon structures represents the main problem. For example, thinking about graphene (the single layer of graphite), which displays an enormous surface area (2630 m^2/g), one can

estimate a 7.7 mass% of chemisorption if each carbon binds one hydrogen (producing the so called graphane). Unfortunately, only at very high temperature this can be possible, because of the high energy barrier to overcome for the dissociation of H_2 on graphene. Moreover, the $C-H$ graphene bond has a binding energy of 140 kJ/mol, still far from the target value of 10-50 kJ/mol which represents the optimal value for near room temperature applications. On the other hand, the binding energy for physisorption is too low (5 kJ/mol) [75]. Is common knowledge that *in medio stat virtus* and the optimal energy range could be fit taking into account some considerations.

- ≻ **The binding energy of hydrogen is enhanced in curved carbon sheets.** This is due to a "transition" from the sp^2 hybridization of flat carbon to a partial sp^3 carbon hybridization. For this reason nanostructures like carbon nanotubes and fullerenes, which displays a high grade of sp^3 hybridization, are more promising for this purpose. It was calculated that the binding energy increases with the curvature [76].

- ≻ **The binding energy increases if the curved sheet is charged.** Both nanotubes and fullerenes show this feature. In a past work Chen *et al.* reported 15-20 mass% H_2 stored on alkali doped nanotubes [77]. Although these high values have never been confirmed and were ascribed to errors, it was, however, confirmed the improvement in the properties with respect bare carbon nanotubes (finally, a more reliable value of $\sim$2 mass% H_2 was measured doping with lithium [78]).
  On the theoretical point of view, DFT calculations clearly show that the binding strength of molecular hydrogen on either positively or negatively charged fullerenes can be dramatically enhanced to 18-22 kJ/mol [79]. In both cases the enhancement is attributed to the polarization of the hydrogen molecule by the electric field generated near the surface of the charged nanostructure.

- ≻ **Metal ions can bind** H_2. The enhanced physisorption (or "mild chemisorption") which occurs in the intermediate range of 10-50 kJ/mol

may be favored by catalyzers. As previously described in paragraph 1.1.1, metal ions can, in principle, bind hydrogen molecules by means of **orbital interaction** [80] (named Kubas interaction in case of metals which possess available *d* orbitals). Similarly, light alkali metal ions can polarize the hydrogen molecule through **electrostatic interaction**. Finally, the spillover can lead to a low energy chemisorption if a metallic cluster is present, supported on good receptor, able to accept hydrogen atoms (as discussed in paragraph 1.1.2).

All these features may be very useful in the design of the hydrogen storage material.

Fullerene molecule presents many advantages since it is indeed a curved carbon plane (rolled up to itself to form a ball) and its ability to accept large degrees of charge is well known (see paragraph 1.2.2). In the last 8 years many theoretical works contributed to increase the interest in this nanostructure. In 2005, Yildirim *et al.* calculated that Ti, Sc and Co can decorate a C_{60} molecule binding up to 56 H_2 via Kubas interaction, corresponding to a 7.5 mass% H_2 stored for $Ti_{12}C_{60}$ [81], with an average binding energy of 300-500 meV/H_2 (about 30 - 50 kJ/mol). In 2006, Sun *et al.* found that an isolated $Li_{12}C_{60}$ "superfulleroid" (a molecule of C_{60} whose pentagonal faces are coordinated by 12 atoms of Li) can store up to 120 hydrogen atoms (about 13 mass% of H_2) with a binding energy of 75 meV/H_2 (about 7.2 kJ/mol) [75]. At the same time, Shin *et al.*, calculated that $Ni_{30}C_{60}$ is capable of storing ∼6.8 mass% H_2 with hydrogen desorption activation barrier of 510 meV/H_2 (about 50 kJ/mol) [84]. In 2008, Yoon *et al.* studied the interaction of C_{60} with alkaline earth metals (Be, Mg, Ca, Sr) and predicted that $Ca_{32}C_{60}$ is able to store up to 8.6 mass% H_2 with an average binding energy of about 200 meV/H_2 (19 kJ/mol) [82]. In the same year, Chandrakumar *et al.*, predicted that the superfulleroid structure Na_8C_{60} can store up to 9.5 mass% H_2 with an average binding energy of about 87 meV/H_2 (∼8.4 kJ/mol) [83]. Some of these *superfulleroids* are depicted in Fig. 1.9. All these structures exhibit a relatively strong coordination of the metal onto the pentagonal ($Ti_{12}C_{60}$, $Li_{12}C_{60}$) and hexagonal

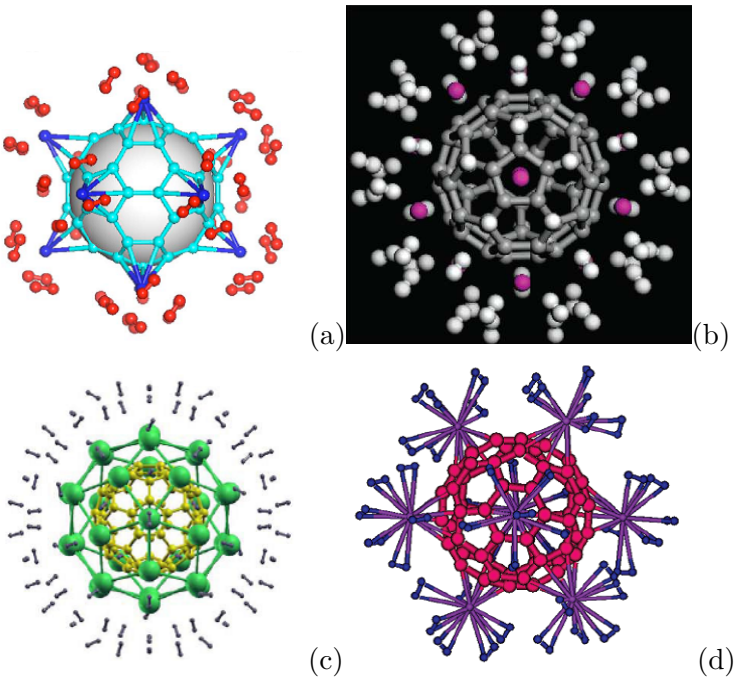

Figure 1.9: *Superfulleroid* structures theoretically predicted to absorb H_2 at mild conditions. (a) $[Ti(H_2)_4]_{12}C_{60}$ [81]. (b) $[Li(H_2)_5]_{12}C_{60}$ [75]. (c) $Ca_{32}C_{60}(H_2)_{92}$ [82]. (d) $[Na(H_2)_6]_8C_{60}$ [83].

(Na_8C_{60}, $Ca_{32}C_{60}$) faces of C_{60} or above the edges between two hexagonal rings ($Ni_{30}C_{60}$). The binding between alkaline earth or transition metals and C_{60} can be generally explained by a simple Dewar-Chatt-Duncanson model, where the interaction is promoted by donation of charge from the HOMO of the ligand (fullerene) to the metal empty states and a subsequent back donation from filled d orbitals to the lowest unoccupied orbital of the ligand. Subsequently, the hydrogen molecule is attracted on the metal by means of Kubas binding, in case of transition metal, or electrostatic interaction (the positive charge of the cation polarizes the hydrogen molecule). In the case of alkali metals, such as in $Li_{12}C_{60}$ and Na_8C_{60}, the strength of these bounds should ensure the existence of these organometallic clusters even outside the theoretical context, however, the stability of these structures in the solid state has never been considered. In fact, it is well

Figure 1.10: The most stable configuration of $Ti_{12}C_{60}$, as predicted by Sun *et al.*, is 24.8 eV lower in energy of the one showed in Fig. 1.9(a) [85]. The metal tends to clustering on the C_{60} surface significantly lowering the total amount of H_2 which is possible to store.

known that Li, Na and Ca exhibit a great tendency to clustering when their concentration exceeds a certain level [86, 59, 64, 54]. Moreover, the high cohesive energy of transition metals would make it very difficult to synthesize the Ti or Ni decorated fullerides avoiding clustering (for example, Sun *et al.* showed that the Ti atoms prefer to cluster on the C_{60} fullerene [85], as displayed in Fig. 1.10). Up to now any of these organometallic compounds has never been isolated in a solid form, while some of them have been produced in gaseous phase [87]. Anyway, a common feature of these systems is found in the type of bond formed between the supported metal and H_2, which is almost never split, remaining in its molecular form (only a slight weakening of the intramolecular bond occurs). This fact would allow a hydrogen adsorption/desorption in the energy range useful for applications.

A different approach to C_{60} hydrogenation considers the possibility of having a complete dissociation of H_2. Also without doping fullerene with metals, is possible to achieve a hydrogenated form of C_{60} (named *hydrofullerene*, or $C_{60}H_x$). Many reagents have been reported to reduce fullerenes to yield mixtures of products with different stoichiometries. Between the highly hydrogenated fullerenes, only the $C_{60}H_{36}$ and $C_{60}H_{18}$ have been thoroughly investigated. It is possible to hydrogenate fullerene by heating under high pressure of hydrogen and at high temperature (350-450

°C) and pressure. The process isn't reversible (prolonged treatment and

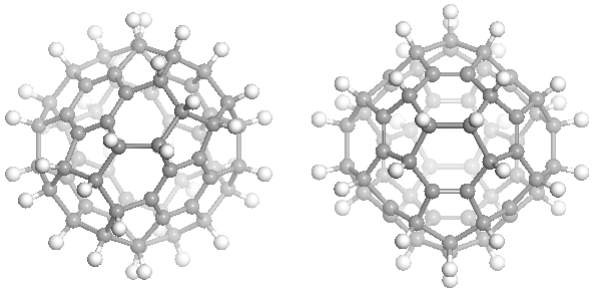

Figure 1.11: Two of the 10^{13} possible isomers of $C_{60}H_{36}$: the T (on the left) and the T_h (on the right) point groups.

desorption resulted in the fullerene cage fragmentation and formation of hydrogenated fragmented fullerenes) and the hydrogenation lead the formation of very different hydrofullerene species (mainly $C_{60}H_{18}$,$C_{60}H_{36}$, $C_{60}H_{44}$, $C_{60}H_{48}$,$C_{60}H_{52}$) [88, 89]. $C_{60}H_{36}$ is considered one of the most stable and reproducible forms of hydrofullerene. It stores approximately 4.8 mass% of H_2 and can be synthesized by means of Birch reduction [90]. It crystallizes in the *bcc* ($Im\bar{3}$ space group) system with lattice constant of 11.785 Å. After the reduction of C_{60} into $C_{60}H_{36}$, the cage undergoes severe distortion (due to the fact that each bound hydrogen turns an sp^2 carbon into sp^3) and there are roughly 10^{13} possible isomers of the molecule [91]. Of these isomers only few of them are considered effectively stables and many works have been published with the intention to determine which of them was the right one [92, 93, 94, 95, 96, 97, 98, 99]. To date, the most stable isomer is believed to be the one having T point group symmetry (see Fig. 1.11) [97, 96], in which hydrogenation takes place so as to leave four benzene rings intact. However, also D_{3d} and T_h isomers have been proposed [94] and debate is still open.

The light alkali metals doped fullerides (such as Li_xC_{60} and Na_xC_{60}) have aroused interest in the field of hydrogen storage applications just in the last 2 years. In 2012 Teprovich *et al.* reported that, under optimized conditions, the Li doped fullerane (with a molar ratio Li:C_{60} of 6:1) desorbs up to 5 mass% H_2 with an onset temperature of ∼270 °C [100]. This work was

carried out after the Teprovich's group had noticed improved performances in complex hydrides ($NaAlH_4$ and $LiAlH_4$) - C_{60} composite systems [101]. In the same period the group of Carbon Nanostructures of Parma University had started a similar work on alkali doped fullerides, as planned in the SNF HyCarbo project (Grant no. CRSII2-130509). In these systems the hydrogenation occurs through a chemisorption process which involves both the charged C_{60} molecules and alkali ions and without the apparent manifestation of Kubas or electrostatic interaction.

Chapter 2

Experimental techniques

2.1 Diffraction methods

A fundamental tool of investigation in the study of synthesized materials is provided by X-rays and neutron diffraction techniques. A detailed introduction to crystallography can be found in the *International Tables of Crystallography* [102].

The investigated samples were always in form of powders and this precludes the use of *direct methods* for the structural analysis. Even in the case of powders, however, is possible to determine the crystal structure by using different methods, such as Rietveld refinement or the Patterson analysis. The analysis of powder pattern can be approached as follows.

- ≻ **pattern indexing**: it consists in the determination of the lattice crystal symmetry. There are 230 space groups, belonging to 7 lattice systems and 32 crystallographic point groups (as reported in table 2.1).

- ≻ **structural model**: after the lattice is defined, atoms and molecules are inserted in the cell providing a model from which starting the refinement.

- ≻ **refinement of the structural model**: this is the last part and allows to find the correct positions of the atoms inside the lattice.

The determination of the space group is a very important step and is usually carried out by indexing the most intense peaks at low angles, assigning the *hkl* reflection for each peak. This can be done with several algorithms, usually implemented in various software suites. Depending on the algorithm, the indexing of peaks can be carried out through a trial & error routine (based on a permutation of the *hkl* Miller's indexes) or by direct variation in the direct space of the lengths (a, b, c) and angles (α, β, γ) of the unit cell (dichotomy method). The TREOR routine pertains to the first type of algorithm while DICVOL91 uses the latter. This first step allows to obtain which lattice system the unit cell belongs. Then, the correct set of symmetry operations of the crystal is obtained through the fitting of the intensity of the pattern's peaks (also called Le Bail analysis). Considering the systematic extinctions, it is possible to find which of the many space groups of the lattice better describes the crystal (or at least reduces the choices), generally the one with the best *figure of merit*. There is not a

crystal systems	lattice systems	crystal classes
triclinic ($a \neq b \neq c$; $\alpha \neq \beta \neq \gamma \neq 90°$)	$\bar{1}$	1,$\bar{1}$
monoclinic ($a \neq b \neq c$; $\alpha, \gamma = 90° \neq \beta$)	$2/m$	2, m, $2/m$
orthorhombic ($a \neq b \neq c$; $\alpha, \beta, \gamma = 90°$)	mmm	222, $mm2$, mmm
rombohedral ($a = b = c$; $\alpha = \beta = \gamma \neq 90°$)	$\bar{3}m$	3, $\bar{3}$, 32 $3m$, $\bar{3}m$
tetragonal ($a = b \neq c$; $\alpha, \beta, \gamma = 90°$)	$4/mmm$	4, $\bar{4}$, $4/m$, 422 $4mm$, $\bar{4}2m$, $4/mmm$
hexagonal ($a = b \neq c$; $\alpha = \beta = 90°$; $\gamma = 120°$)	$6/mmm$	6, $\bar{6}$, $6/m$, 622 $6mm$, $\bar{6}2m$, $6/mmm$
cubic ($a = b = c$; $\alpha, \beta, \gamma = 90°$)	$m\bar{3}m$	23, $m\bar{3}$, 432 $\bar{4}3m$, $m\bar{3}m$

Table 2.1: Table of crystalline groups in 3 dimensions and in the Hermann-Mauguin notation. The 230 space groups are derived from combinations of the 32 crystallographic point groups with the 14 Bravais lattices, each of the latter belonging to one of 7 lattice systems.

general method for build up the structural model. In fullerene systems, the geometry of the C_{60} molecule is normally known, while its arrangement in

the unit cell is unknown. Montecarlo based techniques (such as simulated annealing) or Patterson methods can be very useful at this stage. After defining a starting structural model, the refinement is usually carried out by means of Rietveld method. The Rietveld refinement consists in a least squares analysis which allows to refine a theoretical function (y_{calc}) until it matches the measured profile. The model is described by the function:

$$y_{calc} = y_i \left\{ \sum_h k_h \left| F_h \right|^2 m_h L_h P(\Delta_h) + y_{bgd} \right\}.$$

Here y_i is the scale factor, h is the index identifying the reflection, k_h is the multiplicity factor, F_h is the structure factor, $L_h P(\Delta_h)$ is the Lorentz-polarization factor (with Δ_h the offset between the calculated and the predicted Bragg peak) and y_{bgd} is a baseline function (usually polynomial) describing the background intensity. The least square method consists of a routine procedure which minimizes the normalized sum of residuals (weighted profile):

$$R_{wp} = \sqrt{\frac{\sum w \left(y_{obs} - y_{calc}\right)^2}{\left(\sum w y_{obs}^2\right)}},$$

where y_{obs} is the observed intensity and w a weight. The profile of the peaks can be simulated through many different functions but is generally well described by a pseudo-Voigt:

$$p.V.(\Delta\theta) = \eta L(\Delta\theta, \Gamma) + (1 - \eta) G(\Delta\theta, \Gamma)$$

which is a combination of a Lorentzian (L) and a Gaussian (G) lineshapes with correlated full width at half-maximum (Γ). The Γ parameter is commonly described by the Caglioti formula

$$\Gamma^2 = U \tan^2\theta + V \tan\theta + W$$

for the Gaussian component and by

$$\gamma = \frac{X}{cos\theta} + Y \tan\theta$$

for the Lorentzian one (U, V, W, X and Y are parameters to refine).

The analysis of the powder diffraction profiles presented in this work was performed by using the free software package GSAS/EXPGUI (General Structure Analysis System) [103].

In fullerene systems there are several problems to be addressed. First of all, carbon is a light element and this affects its X-rays scattering cross section (which is proportional to the atomic number) weakening the signal, especially with laboratory X-ray sources. This problem can be easily overcome by acquiring for longer time. Fullerides of light alkali metals have the same problem. In particular, Li is very difficult to localize both with laboratory and synchrotron sources of X-rays. By using neutrons, instead of X-rays, one can overcome some drawbacks. For example, carbon owns a good coherent cross section and zero incoherent cross section. Hydrogen is practically invisible with X-rays (only in some cases a depth analysis with synchrotron light can give more information) and with neutrons the incoherent signal completely cover the coherent one. However, is possible to

isotope	coh. xs (barn)	inc. xs (barn)
^1H	1.7583	80.27
D	5.592	2.05
^{12}C	5.559	0
^7Li	0.619	0.78
Na	1.66	1.62

Table 2.2: table of coherent and incoherent neutron cross section (xs) of the most representative isotopes for this thesis.

obtain structural information by replacing hydrogen with deuterium, whose coherent cross section is more than double that the incoherent one. In table 2.2 the neutron cross section are reported for ^1H, ^2H (or D), Na and the most abundant isotopes of carbon and lithium. It turns out that lithium is hardly visible with both neutrons and X-rays diffraction. Another problem of fullerene systems is the presence of intrinsic disorder: after the unit cell is found, the center of mass of C_{60} can be easily localized but its orientation is never obvious and often merohedral disorder occurs. Moreover, an amor-

phous phase is always present in fullerites, which affects the background signal.

2.1.1 X-ray diffraction experiments

The first analysis of the synthesized samples was performed with a laboratory source on a Bruker D8 discover with GADDS diffractometer, operating in Debye-Scherrer geometry and using a sealed tube generator (CuK_α). The beam is monochromatized and collimated by double cross-coupled Göbel mirrors, inserted between the generator and the specimen. This allows to select just the $K_{\alpha 1}$ line of copper ($\lambda = 1.540612$ Å). The diffracted beam is detected by a 2-dimensional HI-STAR area detector: this is a multi wire proportional counter (MWPC) of 11.5 cm diameter. The 2D image acquired on the detector is processed by the GADDS program and integrated. The specimen is generally in form of a sealed glass (or quartz) capillary filled with the sample powder. The capillary allows to hold an air sensitive sample without ever exposing it to external atmosphere. The Debye-Scherrer geometry allows to analyze also small quantities of sample. The main disadvantage of this diffractometer is presented by the low angular resolution in 2θ ($\sim 0.05°$ with detector at distance of 20 cm from the specimen), which is intrinsically linked to the density of wires in the detector's chamber.

The synchrotron diffractions were carried out at the European Synchrotron Radiation Facility (ESRF, Grenoble, FR) at the ID15b beamline. The scattering angle for the monochromator is almost fixed (10 % tunebility) by the beamline geometry. This determines the range of available energies. There are three monochromators providing 30, 60 or 90 keV radiation. The first two are 40 cm long bent Bragg crystals and the third one is a bent Laue-crystal. The instrument operates in Debye-Scherrer geometry and for pattern's detection the mar345 Image Plate Detector (345 mm of plate diameter, 100 µm^2 pixel size) was positioned at 60 cm from the sample with 2θ fixed to zero (a beamstopper was placed to shield the direct beam). A cold nitrogen gas blower allows to measure from 90 K to room temperature.

2.1.2 Neutron experiments

In-situ monitoring of deuterium absorptions were operated with the HRPT (High Resolution Powder diffractometer for Thermal neutrons) instrument at the SINQ facility of the Paul Scherrer Institut (PSI, Villigen, CH). The spallation neutron source SINQ is a continuous source which provides slow neutrons. The multi-detector diffractometer HRPT [104] is designed as flexible instrument for efficient neutron powder diffraction studies, also for small sample sizes. High resolution ($\delta d/d < 0.001$) is achieved by thermal neutrons, large scattering angles of the monochromator and of the sample (up to 165°). By means of primary collimators, a secondary slit system and by appropriate choice of the sample diameter, resolution and intensity can be optimized. Wide range of neutron wavelengths λ = 0.94-2.96 Å is available. Due to the use of a large position sensitive ^3He detector , simultaneous measurements are possible within a scattering angle range of 160° with angular step 0.1°. The detector can be positioned on air cushions also at intermediate positions and the angular step can be *e.g.* 0.05° or less. A small furnace was installed during the experiments (temperature range 300 -700 K).
Another instrument used in this work was the high-intensity two-axis diffractometer with variable resolution D20 [105], of the Institute Laue-Langevin (ILL) of Grenoble (FR). The variable monochromator take-off angle, up to 120°, increases the flexibility of the instrument, providing high resolution over the complete diffraction pattern at the highest take-off angle with a neutron flux of up to 10^7 $ns^{-1}cm^{-2}$ or a high flux of up to 10^8 $ns^{-1}cm^{-2}$ at medium resolution at lower take-off angle.

2.1.3 The extraction of the Pair Distribution Function (PDF)

In some cases the long range order, found in crystals, is compromised by disorder. This is the case of amorphous solids, nanocrystals and low crystalline materials. In all these systems the order is found only at short or medium range. The peaks of the diffraction pattern (if present) become broad and a quantitative (and often also qualitative) analysis is not possible. However, is still possible to obtain important informations by taking advantage of

the diffuse scattering. This can be very useful for extracting a real space function of the distribution of lengths inside the system.

The distribution of inter-atomic distances in the investigated sample is given by the set of r_{ij} lengths between i and j atoms through the so called *atomic pair density function*:

$$\rho(r) = \rho_0 g(r) = \frac{1}{4\pi N r^2} \sum_{i,j} \delta(r - r_{ij}),$$

where ρ_0 is the numeric density of a system with N atoms and $g(r)$ is the *atomic pair distribution function* (PDF). $g(r)$ displays a series of peaks centered to the lengths corresponding to the inter-atomic distances, $|r_i - r_j|$, and is proportional to the probability to find the i and j atoms at the r_{ij} distance. It is possible to define a reduced PDF:

$$G(r) = 4\pi r \left(\rho(r) - \rho_0\right) = 4\pi r \rho_0 \left(g(r) - 1\right).$$

The PDF can be extracted from the diffraction pattern by calculating the Fourier transform:

$$G(r) = \frac{2}{\pi} \int_0^\infty Q \left[S(Q) - 1\right] \sin(Qr) dQ,$$

where Q is the magnitude of momentum transfer of the scattered X-ray ($Q = 4\pi\lambda^{-1} \sin\theta$, for elastic scattering) and $S(Q)$ is the total scattering structure function. The latter is given by:

$$S(Q) = \frac{I_{coh}(Q) - \langle f(Q)^2 \rangle + \langle f(Q) \rangle^2}{\langle f(Q) \rangle^2}.$$

Here I_{coh} is the coherent scattering and $f(Q)$ is the atomic scattering factor which is averaged over all the atom types in the sample in order to obtain $\langle f(Q) \rangle$ and $\langle f(Q)^2 \rangle$. The therm $Q\left[S(Q) - 1\right]$ is also known as reduced structure function, or $F(Q)$. Since it is not possible to measure the diffraction patter between $Q_{min} = 0$ and $Q_{max} = \infty$, the quality of the extracted PDF

is given by the maximum exchanged momentum attainable in the diffraction experiment. This is mainly affected by the energy of the beam.

The extraction of the PDFs shown in this work was carried out by using the PDFgetX3 routine [106]. The analysis of the PDFs was made with the PDFgui program [107]. A more detailed explanation about the use of these programs can be found in the cited references. Further details about the total scattering experiment will be given in paragraph 3.5. More exhaustive and detailed treatment on the PDF analysis and examples may be found in subject related textbooks [108, 109] and articles [110, 111, 112].

2.2 Absorption measurements (pcT)

The most used method to characterise the hydrogen absorption/desorption properties of materials is volumetry, also known as manometric or Sievert method. With this technique is possible to evaluate the absorbed/desorbed amount of gas of the sample by making use of calibrated volumes. The knowledge of pressure and temperature of the system is sufficient to calculate the amount of the gas phase through an appropriate equation of state. The thermodynamics aspects of the absorption/desorption of hydrogen are described by means of concentration-pressure-isotherms (pcIs). In a typical hydrogenation process there is a *plateau* region in which the solid solution (α-phase) and the hydride phase (β-phase) coexist. The length of the plateau determines the amount of hydrogen stored while the center of the same is generally assumed as the equilibrium pressure (p_{eq}). The latter is related to changes of enthalpy of reaction and entropy of reaction (ΔH_r and ΔS_r respectively) by the van't Hoff equation:

$$\ln\left(\frac{p_{eq}}{p_0}\right) = \frac{\Delta H_r}{R}\frac{1}{T} - \frac{\Delta S_r}{R}, \tag{2.1}$$

where $p_0 = 1.013 \cdot 10^5$ Pa and R is the ideal gas constant. Therefore, temperature fixed, equation 2.1 allows to have the thermodynamics parameters from the equilibrium pressures. A pressure-composition-temperature (pcT) curve provide the relative mass changes allowing the quantitative estimation

of involved stoichiometry. The kinetics of reaction involved in the process follows the Arrhenius equation:

$$K = A \exp\left(\frac{-E_a}{RT}\right),$$

where K is the rate constant, A is an amplitude and E_a is the activation barrier for chemisorption. The dynamic pcT apparatus at EMPA laboratories is a home made instrument [113]. The system consists of the following components:

- hydrogen/deuterium gas supply with pressure regulator,
- reference volume,
- pressure meter,
- temperature controlled sample container,
- vacuum system.

By dynamic pcT measurements the hydrogen pressure is measured as a function of the amount of hydrogen absorbed at a constant temperature. In a typical pcT experiment the sample is loaded inside a high pressure cell and connected to the line. A fixed pressure is set inside the cell and the temperature is ramped to a fixed value. Through the measurement of the pressure inside the cell (which will decreases if an absorption process take places) is possible to derive the amount of absorbed hydrogen. The desorption experiment is carried out by measuring the increase of pressure due to the release of hydrogen inside the cell. It is possible to adopt the ideal gas law:

$$pV = nRT,$$

where p, V, T and n are the pressure, the volume, the temperature and the number of moles respectively, while R is the constant of ideal gases. This equation is valid since the compression factor of the gas is negligible for pressure lower than 200 bar. The relation between the variation of pressure

and the number of moles of the absorbed gas is given by

$$\Delta n_{abs/des} = \Delta p \frac{V}{RT}.$$

Here Δp and Δn are the variations of pressure and moles at the end of the absorption/desorption process. The mass percentage of absorbed/desorbed gas is:

$$mass\%\ H_2 = \frac{2M_H \Delta n_{abs/des}}{m_s},$$

where M_H is the molar weight of hydrogen (1.008 g/mol) and m_s the mass of the sample.

2.3 Muon Spin Relaxation (μSR)

The Muon Spin Relaxation is part of different techniques, known as Muon Spin Rotation/Relaxation/Resonance (μSR). Muons were discovered in 1933 by K. Kunze, who observed the path of this particle in a Wilson chamber. Muons exists as positive or negative charged particles with a mean lifetime of about 2.2 μs. Its charge is equal to the electron's charge and owns a 1/2 spin. The main properties of positive muons are reported in table 2.3. Muons are produced by decaying of pions (with a mean lifetime of about 26 ns) in the following reaction:

$$\pi^{\pm} \longrightarrow \mu^{\pm} + \nu_{\mu}(\bar{\nu}_{\mu}).$$

The weak nuclear interaction leads the pion decay, thus a parity violation takes place, leading the emerging muons to have negative helicity (which means momentum, $\mathbf{P}_{\mu}$, opposite to spin, $\mathbf{I}_{\mu}$). For the purposes of this thesis, only positive muons will be considered, while negative muons are too reactive and undergo nuclear capture, yielding not negligible effects in case of high atomic numbers are involved. At the ISIS large scale facility (Rutherford Appleton Laboratory, Didcot - UK), 100 % spin polarized positive muons are produced from pions generated by 800 MeV energetic protons colliding against a 10 mm thick graphite target. The spin is fully

μ^+ properties	value
charge (q_μ)	$e = 1.60217733(49)\cdot10^{-19}$ C
spin (I_μ)	1/2
mass (m_μ)	105.65839(34) MeV/c^2$\sim$ 0.12 $m_p$$\sim$205 m_e
magnetic momentum (μ_μ)	$4.88 \cdot 10^{-3}\mu_B \sim 8.9\mu_N$
gyromagnetic ratio ($\gamma_\mu/2\pi$)	135.53420(51) MHz/T
mean lifetime (τ_μ)	2.219703(4) μs

Table 2.3: Main properties of positive muon [114].

polarized in the opposite direction with respect the μ^+ linear momentum. After its implantation, the muon can interacts with matter undergoing depolarization. After its mean life-time, the μ^+ undergoes a three body decay, splitting into a positron and electronic and muonic neutrinos:

$$\mu^+ \longrightarrow e^+ + \nu_e + \bar{\nu}_\mu.$$

The kinetic energy of the emerging positron may vary continuously between zero and 52.83 MeV (corresponding to neutrinos traveling together and antiparallel to positron). Thanks to parity violation, all the positrons produced by this reaction are prevalently emitted in the direction that muon spin had before decaying, according to the following angular distribution:

$$W(\theta) = 1 + a\cos\theta. \tag{2.2}$$

Here θ is the angle between $\mathbf{I}_\mu$ and the direction of the emitted positron and a is the *asymmetry factor* which increases monotonically with the energy of the positron up to 1 (for a maximum energy of 52.83 MeV). As can be seen in Fig. 2.1, positrons are emitted mainly in the direction of $\mathbf{I}_\mu$ and the angular distribution integrated over all energies is shifted towards the muon's spin. In a typical μSR experiment, 100 % spin polarized muons are implanted in the sample with their spins oriented in the opposite direction to their motion. Due to their very high kinetic energy (∼4 MeV), the firsts instants are employed to the thermalization of the muon through deceleration. Finally, when the muon is thermalized, the particle found a convenient

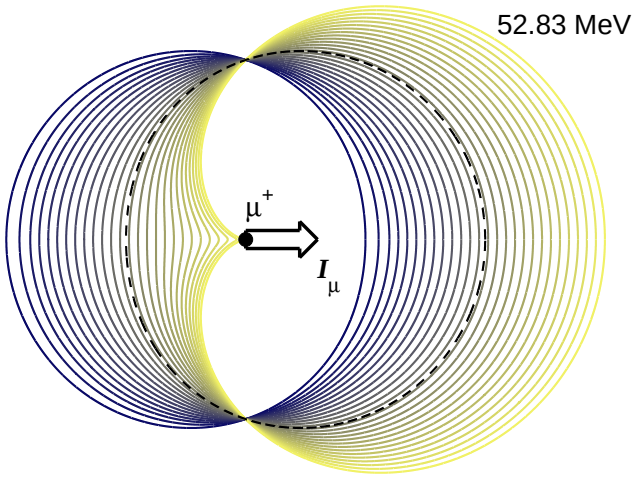

Figure 2.1: Muon decay: angular distribution of positrons from positively charged muons for various positron energies, according to equation 2.2, between zero and $\frac{1}{2}m_\mu c^2$. The black dashed line is the angular distribution integrated over all energies.

energy minimum and there its spin starts to precess around the local field. In Fig. 2.2 the muon is localized at the center (where the sample is placed) of two positrons detectors. When the muons decay, detectors count the emitted positrons. If, for example, the sample was diamagnetic, $\mathbf{I}_\mu$ would stays unperturbed and positrons would mainly detected in the backward counter. In case of paramagnetic substances fluctuation of internal fields would depolarizes the muon's spin leading a temporal decaying signal in both detectors. The evolution of the muon's polarization is described by the experimental asymmetry function (or muons polarization):

$$A(t) = a_0 P(t) = \frac{N_F(t) - \alpha N_B(t)}{N_F(t) + \alpha N_B(t)},$$

where $N_F(N_B)$ is the number of positrons counted at the forward (backward) detector as a function of time, a_0 is a scale factor and α is an experimental factor (mainly depending on sample position detector efficiencies) which is determined by previous calibrations. The behavior of $P(t)$ depends on the investigated material. If there is no time evolution of the muon polarization,

the positron count rate is:

$$N_i(t) = N_0 \exp\left(-\frac{t}{\tau_\mu}\right) + B_g,$$

where B_g is the background (usually very small). There are mainly three

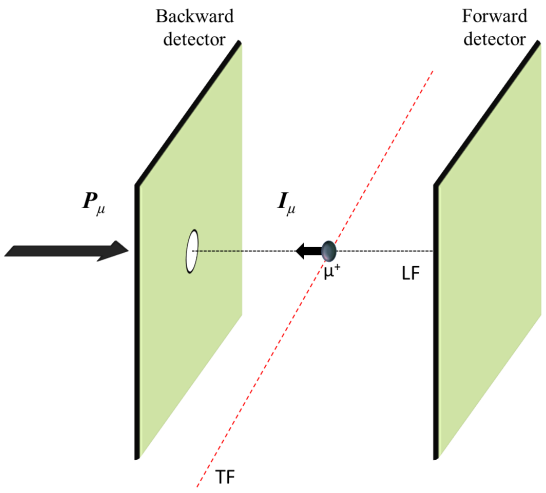

Figure 2.2: Instrumental setup of the positrons backward and forward detectors for a LF (ZF) experiment (external magnetic field parallel to $\mathbf{P}_\mu$) or TF experiment (field perpendicular to $\mathbf{P}_\mu$).

different experimental configuration for a μSR experiment:

- ≻ zero field (ZF),
- ≻ longitudinal field (LF) and
- ≻ transversal field (TF).

The former (ZF) is simply a measure of $P(t)$ without any applied field ($B = 0$). The LF experiment is made by applying a static external magnetic field along the axis parallel to $\mathbf{P}_\mu$. The TF experiment consists in the measure of the muon polarization under the influence of an external static field applied

along the axis perpendicular to $\mathbf{P}_\mu$. In this case, the positron count rate is:

$$N(t) = N_0 \exp\left(-\frac{t}{\tau_\mu}\right)(1 + a_0 P_z(0) cos\left(\gamma_\mu B t\right)).$$

In ZF and TF the μ^+ is forced to precess around the local field plus the external field (if $B \neq 0$) with the angular frequency:

$$\omega = \gamma_\mu (B + B_{loc}).$$

In this case the forward and backward positron count rates can be expressed as:

$$N_F(t) = N_0 \exp\left(-\tfrac{t}{\tau_\mu}\right)(1 + a_0 P_z(t))$$
$$\alpha N_B(t) = N_0 \exp\left(-\tfrac{t}{\tau_\mu}\right)(1 - a_0 P_z(t))$$

and $P_z(t)$ assumes a complex behavior that depends on the type of interactions involved.

When the muon is implanted in matter its behavior depends on the environment. For example, if μ^+ stops in a minimum of the electrostatic potential and experiences a static and randomly oriented distribution of fields (*e.g.*: originated from surrounding nuclear dipoles or electron momenta) its polarization will start to precess following a Gaussian decay and can be expressed by:

$$P_z(t) = \frac{1}{3} + \frac{2}{3}\left(1 - \sigma^2 t^2\right) \exp\left(-\frac{\sigma^2 t^2}{2}\right),$$

which is known as "Gaussian Kubo-Toyabe" function. In diluted regimes this can be also expressed through a Lorentzian Kubo-Toyabe:

$$P_z(t) = \frac{1}{3} + \frac{2}{3}(1 - \lambda t) \exp\left(-\lambda t\right).$$

Due to the initial spin-polarization of μ^+, $\frac{1}{3}$ of the polarization is already in the direction of the parallel oriented local field components and it won't precess. The remaining $\frac{2}{3}$ of the polarization will precess at the local field. In case of diffusive regimes the Kubo-Toyabe can be simply replaced by

Gaussian or Lorentzian functions (as will be better explained in paragraph 3.6). When the investigated sample presents a magnetic order (*e.g.*: ferromagnetic or antiferromagnetic order), the muon starts to precess at the local field and an oscillation in $P_z(t)$ can be seen, whose period is proportional to the local field.

In metals, the Yukawa potential screens the muon charge so that muon doesn't couple with electrons. When the density of free carriers is below the critical value of $n_c \sim 3 \cdot 10^{23}$ cm^{-3}, the electrostatic screening of the muon charge is not effective anymore and a bound state between muon and an electron may be formed [115]. The bound state is chemically equivalent to a hydrogen atom and is known as muonium, or Mu ($\mu^+ e^-$). For a free muonium in vacuum the hamiltonian can be written as:

$$\mathcal{H}/\hbar = \gamma_e \mathbf{S_e B} - \gamma_\mu \mathbf{I}_\mu \mathbf{B} + A_\mu \mathbf{S_e I}_\mu, \tag{2.3}$$

where γ_e and γ_μ are the gyromagnetic ratios of the electron and muon ($\gamma_e/2\pi$ = 27.992 GHz/T; $\gamma_\mu/2\pi$ = 135.5 MHz/T), S_e and I_μ are the muon and electron spins. The first two terms describe the Zeeman interaction. In the last term, the muon and electron spins are coupled by the hyperfine interaction through the hyperfine parameter A_μ (which is 4463.3 MHz for muonium). This can be expressed as:

$$2\pi A_\mu = \frac{2\mu_0}{3} \gamma_\mu \gamma_e \hbar \left|\psi(0)\right|^2, \tag{2.4}$$

were μ_0 is the vacuum magnetic permeability and $\psi(0)$ is the wave function at the muon position. The diagonalization of the hamiltonian of equation 2.3 leads to define the Breit-Rabi levels of Fig. 2.3, whose energies are described by the subsequent four $|e^-\mu^+\rangle$ spin *eigenstates*:

$$\begin{aligned} E_1 &= |\alpha_e \alpha_\mu\rangle \\ E_2 &= c\,|\alpha_e \beta_\mu\rangle + s\,|\beta_e \alpha_\mu\rangle \\ E_3 &= |\beta_e \beta_\mu\rangle \\ E_4 &= c\,|\beta_e \alpha_\mu\rangle - s\,|\alpha_e \beta_\mu\rangle \end{aligned} \tag{2.5}$$

Here α_i and β_i represents the spin states of the muon (electron), c and s are mixing coefficients. In equation 2.5, E_4 is the singlet state (the blue one in the upper left graph of Fig 2.3), relative to $J = 0$ and $m_J = 0$, while E_1, E_2 and E_3 are the triplet's states relative to $J = 1$ and $m_J = 1$, 0, -1.
The easiest way to study muonium is by means of a TF experiment in low field, which allows to split the triplet states and determine the $\Delta m = \pm 1$ transitions: ν_{12} and ν_{23} ($\nu_i = E_i/h$). In this case the hyperfine parameter can be determined by:

$$A_\mu = \frac{1}{2}\left[\frac{(\nu_{12} + \nu_{23} + 2\nu_\mu)^2}{\nu_{23} - \nu_{12}} + \nu_{12} - \nu_{23}\right].$$

In many cases the instrument measurable frequencies doesn't allow to see the very high precession signal of muonium: for example, the instrumental bandwidth in ISIS is 0.1-10 MHz, definitely too low to see the precession of Mu. In these case, is possible to detect the formation of muonium through a LF experiment by directly measuring the hyperfine parameter. This is possible by decoupling the spin of the muon from the electron spin in Paschen-Back regime at the hyperfine field:

$$B_{hyp} = A_\mu / \left(|\gamma_e| + \gamma_\mu\right). \tag{2.6}$$

When the field is off, half of the polarization is in the E_1 or E_3 states and half is a superposition of E_2 and E_4. In this condition half of the polarization undergoes precession while the other one is recovered at the hyperfine field. The field dependent longitudinal polarization (also known as *quenching curve*) may be expressed as:

$$P_z = \mathrm{tr}\left[\left(\mathbf{v}'\mathbf{I}_z\mathbf{v}\right)^2\right],$$

where $\mathbf{v}$ are the *eigen*-vectors of $\mathcal{H}$ (bottom graphs in Fig. 2.3).

In several cases, muonium isn't stable after its formation and quickly reacts with the sample forming radical species. This is typical of aromatic compounds (such as benzene or ethylene). In radicals, the Paschen-Back

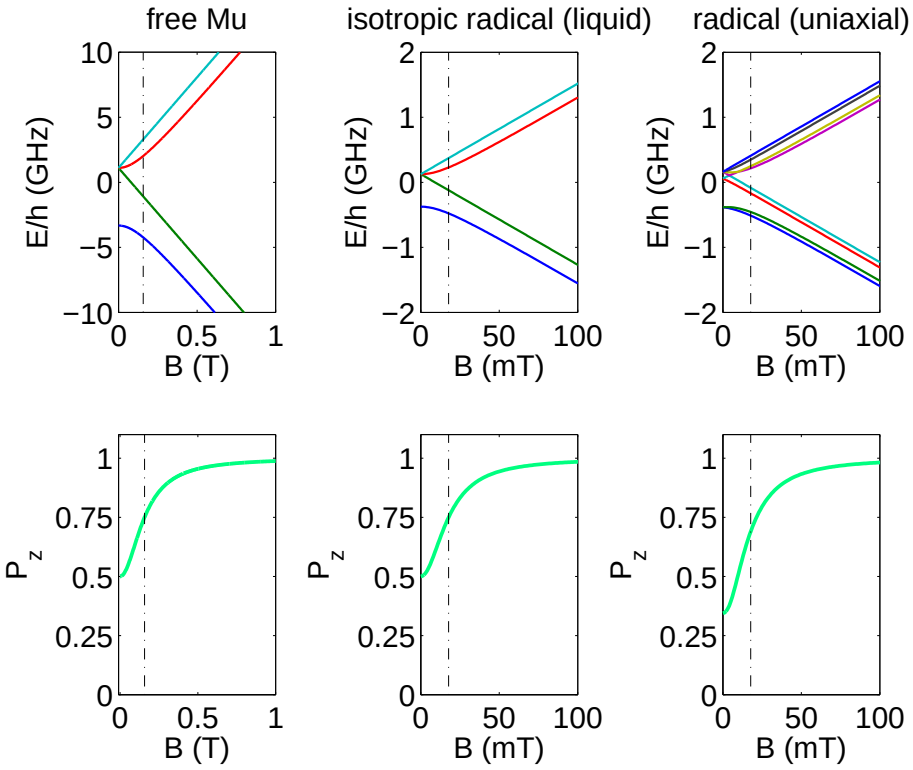

Figure 2.3: Calculated Breit-Rabi diagrams (top) and the relative simulated quenching curves (bottom) for free muonium in vacuum (left), a free radical in a isotropic environment (center) and for a radical coupled to a proton in benzene. The black vertical dashed line highlights the hyperfine field as calculated from eq. 2.6. The hyperfine frequency of the radical is fixed to 500 MHz and the proton frequency is 150 MHz.

regime is reached at lower fields because of the delocalization of the wave-function of the bound electron (ψ_{el} in equation 2.4) over many nuclei[1]. In liquid systems the behavior is quite similar to that of muonium (as can be seen in the upper central graph in Fig. 2.3). More in general, the symmetry of ψ_{el} is not spherical (*e.g.*: as in the $1s^1$ state in Mu) and in this case the hyperfine coupling becomes a tensor. A more exhaustive and detailed

[1]Here the Hamiltonian is $\mathcal{H}/\hbar = \gamma_e \mathbf{S_e B} - \gamma_\mu \mathbf{I}_\mu \mathbf{B} + A_\mu \mathbf{S_e I}_\mu + \delta\nu_0 S_e^z I_\mu^z + \mathcal{H}_{dip}$, where the fourth therm is due to the anisotropy of ψ_{el} ($\delta\nu_0$ is a non diagonal tensor), while the latter is the dipolar interaction with other nuclei.

treatments of this situation can be found in [116].

In this work the μSR measurements were done at the Rutherford Appleton Laboratory near Oxford in the UK. The ISIS facility is the World's most intense source of pulsed muons (single pulse of 80 nm FWHM, beam-size tunable from 10-27 mm FWHM) for condensed matter research. The experiments were performed on the EMU instrument: a 96-detector μSR spectrometer which is optimized for zero field and longitudinal field measurements. Fields of up to 5 kG can be applied in LF mode by means of Helmholtz coils. Sample temperatures can be tuned in the range of 50 mK to 1500 K by using a variety of sample environment equipment.

Chapter 3

Experimental Results and Discussion

In this chapter the synthesis and the physical study of the investigated materials is discussed. The shown samples are the most interesting and promising of a wide range of synthesized materials. The synthesis of different stoichiometric compounds of sodium intercalated fulleride (Na_xC_{60}, x = 6, 8, 10), calcium intercalated fulleride (Ca_xC_{60}, x = 6, 8, 12, 32), lithium intercalated fulleride (Li_xC_{60}, $x = 6, 12$), and transition metal intercalated/decorated fullerites/alkali doped fullerides (namely Ti_xC_{60}, Ni_xC_{60}, $(Ti, Ni)_x(K_3, Li_6, Na_{10})C_{60}$) were investigated. However, only $Na_{10}C_{60}$, $Li_{12}C_{60}$ and Li_6C_{60} were fully characterized, especially for their high values of absorbed hydrogen, the relatively fast kinetics of absorption process and the simplicity of the synthesis methods.

Preliminary X-ray measurements were performed in the XRD laboratory of Parma. Most of the various experiments were carried out in different laboratories. *In situ* neutron powder diffraction measurements were performed with the HRPT (High-Resolution Powder diffractometer for Thermal neutrons) instrument [104] at the Swiss spallation neutron source (SINQ) at the Paul Scherrer Institute (PSI), Villigen (CH). Hydrogen/deuterium absorption measurements were carried out by Dr. Philippe Mauron at Empa (Swiss Federal Laboratories for Materials Science and Technology, division

of "Hydrogen and Energy" Dübendorf, Switzerland) with a home built dynamic pcT (pressure, composition, Temperature) instrument [113] or by Dr. Chiara Milanese (Pavia Hydrogen Lab C.S.G.I. - Department of Chemistry - Physical Chemistry Division University of Pavia) with a PCTPro-2000 manometric instrument by Setaram. Muon spin relaxation experiments were carried out on the EMU spectrometer at the ISIS-Rutherford Appleton Laboratories (RAL), Didcot (UK).

3.1 Synthesis and first characterization of cluster intercalated fullerides

99.9+ % polycrystalline C_{60} was purchased from M.E.R. Corporation and purified in dynamic high vacuum at 250°C for 12 hours before using. Pure sodium (99.95 %) and granular lithium (99 %) were purchased from Alfa-Aesar and Sigma-Aldrich respectively. Anhydrous NaN_3 was purchased from Sigma-Aldrich and purified.
To produce $Na_{10}C_{60}$, a stoichiometric amount of sodium azide (NaN_3) was homogeneously mixed with C_{60} in a agatha mortar and grinded together in order to obtain a fine powder. The powder was then pelletized and the pellets were placed inside tantalum foil bags. The decomposition of NaN_3 and the subsequent diffusion of Na inside the C_{60} structure follows the formula:

$$C_{60} + x \cdot NaN_3 \Longrightarrow Na_xC_{60} + \frac{3}{2}x \cdot N_2$$

The pellets were sealed inside a Pyrex vial and the final product is reached by solid state reaction achieved by slow heating up to 450 °C and subsequent annealing for at least 5 hours in dynamic high vacuum. A typical thermal annealing is displayed in Fig. 3.1. The NaN_3 start to decompose at ∼365 °C.

Lithium intercalated fullerides Li_6C_{60} and $Li_{12}C_{60}$ were synthesized by cutting very small flakes of granular Li and joining in stoichiometric amount with C_{60} powder. About 500-600 mg of the reagents were grinded in a 3

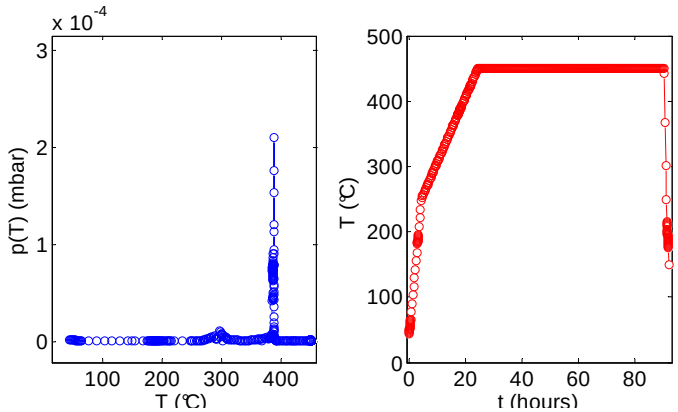

Figure 3.1: Thermal desorption of NaN_3/C_{60} (on the left) displayed as temperature dependent pressure inside the vial and profile of annealing (on the right).

spheres agatha high energy ball-mill (Fritsch Mini-Mill Pulverisette23) at 30 Hz for 60 min (which were divided in 10 minutes turns, each separated by 5 minutes of rest period). When the sample became a uniform black powder it was pressed in small pellets (∼100 mg). The pellets were put inside tantalum foil bags, sealed in high vacuum ($< 1 \cdot 10^{-5}$ mbar) in a Pyrex vial and heated at 270 °C for 36 hours so as to allow the diffusion of lithium.

A first characterization of the obtained compounds is reported in Fig. 3.2. $Na_{10}C_{60}$ and $Li_{12}C_{60}$ can be easily indexed with the *fcc* structure of fullerite. In the case of $Na_{10}C_{60}$ the Le Bail analysis with the $Fm\bar{3}$ space group gives an expanded lattice of $a = 14.49$ A (for comparison *fcc* fullerite has 14.17(1) Å at 300 K [117]). The fitted lattice parameter is in between of the relative to 14.381 Å value for $Na_{5.9}C_{60}$ [59] and the one of a =14.59 Å found by Yildirim *et al.* for $Na_{9.7}C_{60}$ [64]. In both the case of Na_6C_{60} and $Na_{10}C_{60}$ it was found a $Fm\bar{3}$ structure in which the *8c* tetrahedral sites $(\frac{1}{4}\frac{1}{4}\frac{1}{4})$ of the *fcc* ordered C_{60} fullerite were occupied by Na^+ cations as well as the central *4b* $(\frac{1}{2}\frac{1}{2}\frac{1}{2})$ octahedral void and *32f* (xxx) sites. In particular, the *4b*

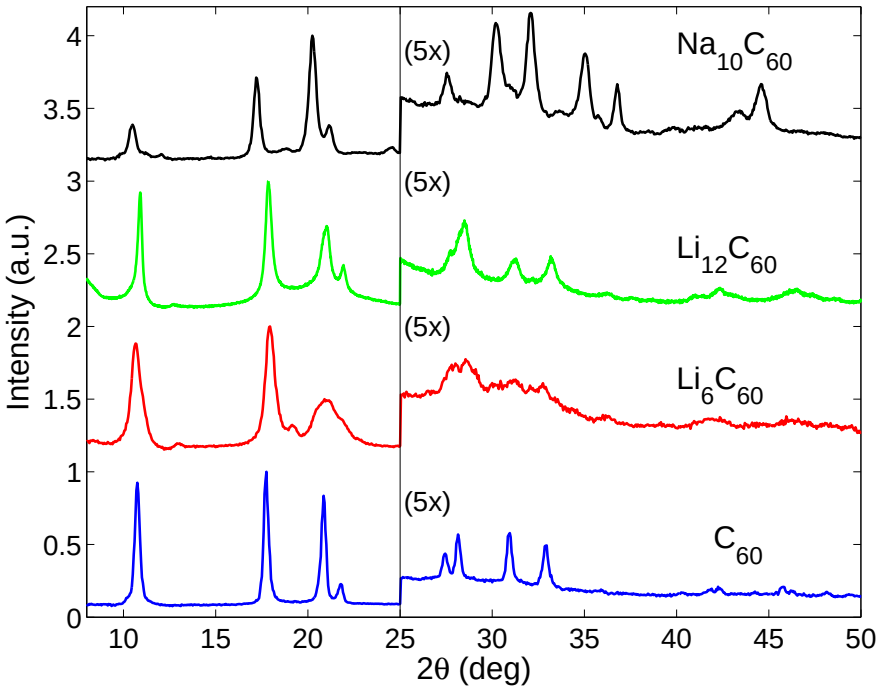

Figure 3.2: Room temperature XRD spectra of $Na_{10}C_{60}$, Li_6C_{60} and $Li_{12}C_{60}$ compared with the spectrum of pure C_{60}. The spectra were collected with laboratory instrument. Data were magnified (5x) for $2\theta > 25°$.

and the *32f* atoms form a *bcc* cluster of sodium. The Na_6C_{60} and $Na_{10}C_{60}$ structures, proposed by Rosseinsky and Yildirim [59, 64], are very similar: in both of them the octahedral void of *fcc*-C_{60} is filled by a cubic cluster of sodium atoms; in the Na_6C_{60} the cluster is simple cubic (*sc*) while in $Na_{10}C_{60}$ is body centered cubic (*bcc*), as shown in Fig.3.3. A simple linear interpolation of the known lattice constants for $Na_{9.7}C_{60}$ and $Na_{5.9}C_{60}$ gives $x \simeq 8.83$. Also for $Li_{12}C_{60}$ a fast analysis of laboratory XRD suggests the formation of a *fcc* structure. In that case the spectrum was fitted by means of Le Bail analysis using the $Fm\bar{3}m$ cell of C_{60} and the refined lattice constant was $a = 13.880(9)$ Å ($R_{wp} = 10.52\%$). The structure is contracted with respect to the pure fullerite (14.17(1) Å [23]) and this could be ascribed by the strong Coulomb interaction induced by the presence of Li^+ ions/clusters with the C_{60}^{n-} anions. It is well known that also with lithium the fullerene can

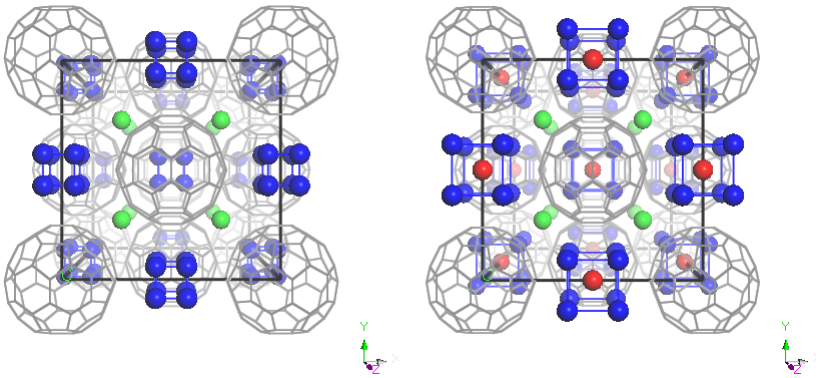

Figure 3.3: From left to right: Na_6C_{60} and $Na_{10}C_{60}$ structures. C_{60} molecules form the *fcc* structure occupying the corners (0 0 0) and the faces of the cell $(\frac{1}{2}\frac{1}{2}\frac{1}{2})$; Na atoms fill the *8c* (green spheres), *32f* (blue spheres) and *4b* (red spheres) Wyckoff positions.

produce cluster intercalated compounds. For example, when Li_4C_{60}, which is a polymeric phase, is heated up to 773 K, it becomes a *fcc* monomer with $Fm\bar{3}m$ structure (a = 14.122 Å) with a partially filled *bcc* cluster in the octahedral void [50]. In the case of Li_6C_{60} the XRD spectrum is more complex: while the (111) and (220) peaks of the *fcc* structure can be easily recognized, the (311) and (222) peaks are overlapped. Peaks of this phase appear broad, but can be easily indexed as *fcc* monomer phase belonging to the lithium intercalated fulleride plus a small fraction of monoclinic cell, isostructural to Li_4C_{60} polymer, accordingly to [51]. The large width of the peaks suggests that the *fcc* phase should present large disorder.

The Raman spectra of $Na_{10}C_{60}$ and Li_xC_{60} (x = 6, 12) were measured in Dübendorf (by Dr. Philippe Mauron, EMPA) and in Pavia (by Dr. Pietro Galinetto, Dipartimento di Fisica "A. Volta") respectively. The spectrum of $Na_{10}C_{60}$ was recorded at room temperature on a sample sealed inside a quartz capillary with a Bruker Senterra instrument with 3.5 cm^{-1} spectral resolution in combination with a 10x objective using a 532 nm laser. The laser power was limited to 0.2 mW in order to avoid polymerization of the fulleride [118]. The Li_xC_{60} were measured inside sealed glass capillary with a He-Ne laser (λ = 632.8 nm) with 1 mW power, spectral resolution of 1

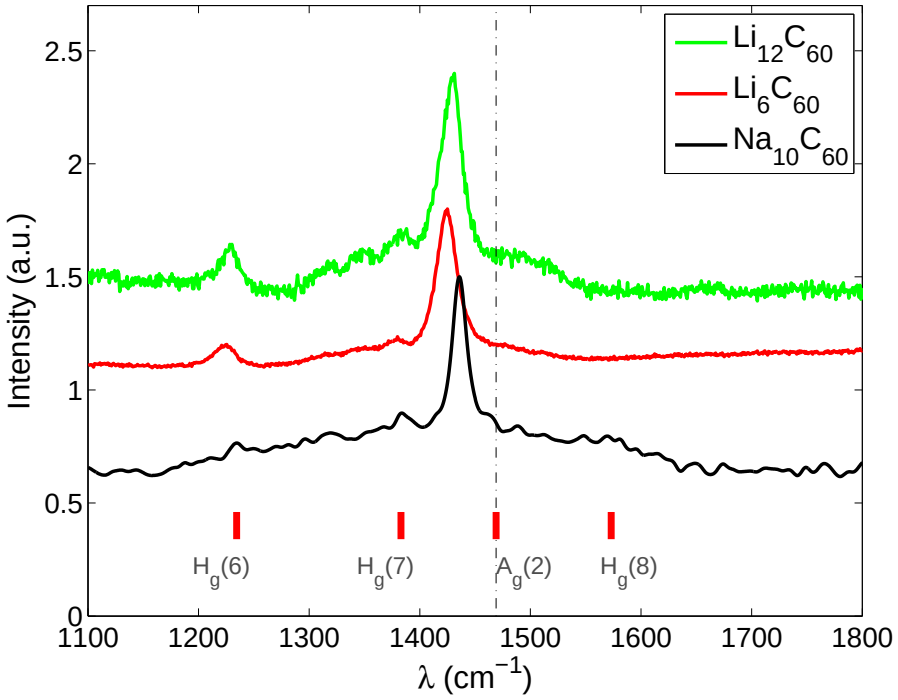

Figure 3.4: Raman spectra of $Na_{10}C_{60}$, Li_6C_{60} and $Li_{12}C_{60}$ as recorded at room temperature. The data have been normalized (and smoothed for $Na_{10}C_{60}$) and arbitrarily shifted along the vertical axis. Red signs represents significant peaks for pristine C_{60} (the $A_g(2)$ mode was evidenced as a black dashed line in order to highlight the shift in doped fullerides).

cm^{-1} and 50x magnification. The intensity was reduced by making use of a filter (optical density 0.6) in order to avoid polymerization. The Raman spectra of $Na_{10}C_{60}$ and Li_xC_{60} are reported in Fig. 3.4. It is well known that of the 174 vibrational modes ($3 \cdot 60$ -3 translations -3 rotations) of C_{60}, because of the I_h point group of the molecule, the number is reduced to 46 distinct eigenstates. The Raman active modes are reduced to the 2 times degenerate A_g and the 8 times degenerate H_g modes (while the IR active modes are the four T_{1u} vibrations). The eight H_g modes, fivefold degenerate each, retain an axis of fivefold symmetry. The two symmetric A_g modes are commonly known as *breathing* mode (every carbon moves radially from the

center of the molecule, $A_g(1)$) and the pentagonal *pinch* mode (in which the two bond lengths C_p-C_h and C_h-C_h are modulated, resulting in a variation of the area of the pentagon faces, $A_g(2)$). In particular, the $A_g(2)$ peak of C_{60} is very sensitive to polymerization and charge transfer. In pure C_{60} the $A_g(2)$ peak is located at 1469 cm^{-1} at 300 K and is shifted to lower wavenumbers by 6-7 cm^{-1} per electron transferred to the C_{60} due to the softening of the $C-C$ bond stretching modes as the electrons enter the antibonding molecular orbitals. In the case of polymerization it is downshifted about 5.5 cm^{-1}/ polymer bond on the molecule [119]. These rules are of empirical origin and only allow a qualitative evaluation of the effective charge transfer sustained by C_{60}. The Raman experiment is summarized in table 3.1. In

	$\lambda_{A_g(2)}$ at 300 K (cm^{-1})	shift (cm^{-1})	n for C_{60}^{n-}
C_{60}	1469	0	0
$Na_{10}C_{60}$	1436	33	5.1
Li_6C_{60}	1425	44	6.8
$Li_{12}C_{60}$	1430	37.7	5.8

Table 3.1: $A_g(2)$ peak, its displacement with respect to 1469 cm^{-1} for pristine C_{60} and estimated number of electrons for C_{60}^{n-}, calculated with the rule of 6.5 cm^{-1}/charge.

the case of $Na_{10}C_{60}$ the $A_g(2)$ peak is centered at 1436 cm^{-1}, corresponding to a charge transfer of ∼5.5 electrons with an adopted downshift of 6 cm^{-1} per charge (4.7 electrons if 7 cm^{-1}/ charge is assumed). This is consistent with the presence of a non completely ionized cluster of sodium atoms in the octahedral void. The Li_6C_{60} spectrum shows an $A_g(2)$ peak shifted down to 1425 cm^{-1} which correspond to about 7.3 electrons per C_{60} (6.3 electrons if 7 cm^{-1}/ charge is assumed) while in the case of $Li_{12}C_{60}$ the $A_g(2)$ mode is at ∼1430 cm^{-1} which results in 6.5 electrons (6.3 for 7 cm^{-1}/ charge). The interpretation of these data is not trivial at all: while the empirical rule suggest different types of charge transfer, depending on the fulleride, the error could be of a certain size. In the case of $Na_{10}C_{60}$ a charge transfer of about 5 electrons on the fulleride suggest a triplet spin state on the molecule. Nevertheless, the sample was also investigate by means of SQuID

magnetometry and it was confirmed to be diamagnetic, with a very small fraction of paramagnetic impurities. Therefore, the number of electrons on fullerene has to be even. The disagreement between the Raman and SQuID measurements could be explained by the fact that if the cluster's orbitals interact with the molecular orbitals of a charged C_{60}^{n-} they may incur reciprocal hybridization thus modifying the Raman spectrum [120, 48], forming a LUMO-metal hybrid band at the Fermi level. The same effect could be present in the Li_xC_{60} compounds, where the shift in the $A_g(2)$ peak can be ascribed by a full filling of the t_{1u} MO. The diamagnetic behavior of both Li_6C_{60} and $Li_{12}C_{60}$, as measured by means of SQuID magnetometry, is indicative of a singlet spin state which means that 6 electrons, rather than 5 or 7, are populating the antibonding molecular orbitals of C_{60}. In the case of Li_6C_{60} the presence of a minority phase of polymer can affect the Raman spectrum.

Comparing these results with diffraction, for the $Na_{10}C_{60}$ and $Li_{12}C_{60}$, the alkali metals donate only partially their charge while the rest of the electron density will be possibly moved to the alkaline cluster. On the other hand, the Li_6C_{60} is more difficult to interpret: the *fcc*-like structure detected by X-ray diffraction suggests the presence of aggregates. In fact, the cubic structure of C_{60} can accommodate two non equivalent atoms (A) in the tetrahedral and octahedral voids leading to a maximum of A_3C_{60} stoichiometry, therefore the only way to obtain a *fcc*-A_6C_{60} is to add almost one more inequivalent atom, leading to the formation of clusters. The Raman measurement shows a full charge transfer, so the cluster has to be completely ionized. This fact is partially in conflict with the interpretation suggested by the µSR experiment, as will be discussed in paragraph 3.6, but a possible explanation will be given.

3.2 Structural analysis of alkali intercalated fullerides

The structural study of the $Na_{10}C_{60}$ and $Li_{12}C_{60}$ phases is of fundamental importance for well understanding the differences of these systems from the previous studied alkali intercalated fullerides, such as the superconducting A_3C_{60}, the semiconducting A_4C_{60}, A_6C_{60} ($A = K$, Rb and Cs) and the polymeric crystals (*e.g.*: Na_4C_{60} and Li_4C_{60}). Lithium and sodium are the smallest alkali atoms on the periodic table (some of their physical properties are reported in table 3.2). This characteristic permits in principle the intercalation inside the big voids of C_{60} lattice and have proved in the past to allow the formation of clusters, differently from what observed with heavier alkali metals.

	Ion. r. (Å)	Cov. r. (Å)	Met. r. (Å)	T_m(°C)	E_1(kJ/mol)
Li	0.68	1.34	1.52	180.5	518.8
Na	0.95	1.54	1.92	97.8	497.9

Table 3.2: Main physical properties of Li and Na elements. Ionic , covalent and metallic radius, melting point, vapor pressure and the first ionization energy.

The as prepared $Na_{10}C_{60}$, obtained from thermal decomposition of sodium azide, was investigated by means of X-rays synchrotron radiation at the ID15B beamline of the European Synchrotron Radiation Facility (ESRF). The wavelength was fixed to 0.22235(1) Å. The sample was sealed inside a borosilicate capillary of 0.7 mm diameter and spinned while measuring. Data were collected at 90 and 300 K and no structural transitions were found between these temperatures. Image data were masked in order to remove the beam-stopper shadow and integrated using the Fit2D software [121]. The diffraction pattern presents quite narrow peaks, evidencing good crystallinity, and a small background contribution, mainly due to the invariably present amorphous fraction of the sample and glass capillary. The low number of peaks and the similarity with the diffraction pattern of pristine C_{60} suggest the formation of a face centered cubic structure, as also observed

with laboratory X-ray diffraction at room temperature (Fig. 3.2). A small fraction of hexagonal phase of sodium fullerite is present and was removed from further calculations. Le Bail analysis indicated that reflections can well described by the $Fm\bar{3}$ space group proposed by Yildirim *et al.* [64] and Rosseinsky *et al.* [59]. The Rietveld refinement of data (displayed in Fig. 3.5) with the model proposed by Yildirim *et al.* (see Fig. 3.3) confirmed that the structure is *fcc,* with a *bcc* sodium cluster located in the octahedral voids. The lattice constant increases from $a = 14.448(1)$ Å at 90 K to 14.564(5) Å at 300 K, slightly smaller than the room temperature value of 14.59 Å for $Na_{10}C_{60}$ of [64]. The main differences between the structure of Yildirim and the refined one are in the different occupancies of Na: the alkali atom in the central *4b* site refine to the full occupancy here while it was about 0.4 in the previously published structure. The *32f* sites refine to 0.695(6) (respect to 0.89) and the *8c* to 0.910(14) (0.88). These discrepancies can be originated by different method of synthesis. The most relevant refined parameters are reported in Table 3.3.

Space group	$Fm\bar{3}$
a (300 K)	14.564(4) Å
a (90 K)	14.449(1) Å
formula	$Na_{8.38}C_{60}$
R_{wp}	3.33 %
$d_{Na(4b)-Na(32f)}$	2.449 Å

Table 3.3: Refined parameters of $Na_{10}C_{60}$ at 90 K and lattice constant at 300 K.

The analysis of $Li_{12}C_{60}$ by means of synchrotron radiation (ID15B, $\lambda = 0.22235$ Å) is more difficult, due to the low scattering factor of Li and mostly to the damping of the intensity at high angle (typical of X-rays). Anyway, the synchrotron pattern (not displayed here, but similar to the one reported in Fig. 3.2) shows the presence of a single (*fcc*-like) phase without any presence of polymeric features, expected from low stoichiometric compounds (such as Li_4C_{60}). Furthermore, there is no clear differences between the spectra recorded at 300 and 90 K (a part the usual thermal shift). Le Bail

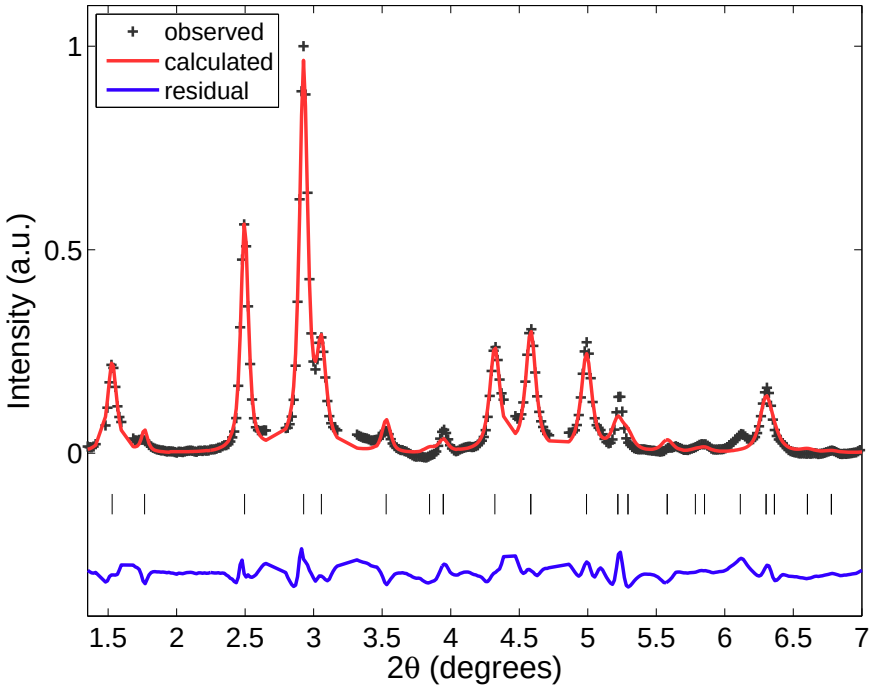

Figure 3.5: Final observed and calculated synchrotron diffraction profile for $Na_{10}C_{60}$ at 90 K (space group: $Fm\bar{3}$, a = 14.448(1) Å, $Na_{8.74}C_{60}$, R_{wp} = 3.1 %). The blue solid line shows the difference profile, and the tick marks highlight the allowed reflections.

analysis with the $Fm\bar{3}m$ space group of C_{60} leads to a lattice parameter of a = 13.997(4) at 300 K and 13.981(4) at 90 K. The contracted value of a, with respect to pristine C_{60}, is attributed to the high electrostatic attraction of Li ions with charged fullerenes. In order to overcome the problems related to the low quality of the X-rays pattern, a diffraction experiment were carried out by using neutrons instead of X-rays at the D20 beamline of the Institut Laue-Langevin (ILL). The sample was sealed in glove box in a cylindrical vanadium sample holder. The wavelength was fixed at λ = 1.36 Å and data were collected at 20 K (by using a cryostat) in order to decrease the Debye-Waller damping contribution and to freeze the librational motion of C_{60}, possibly present at room temperature. Although, at first sight, the

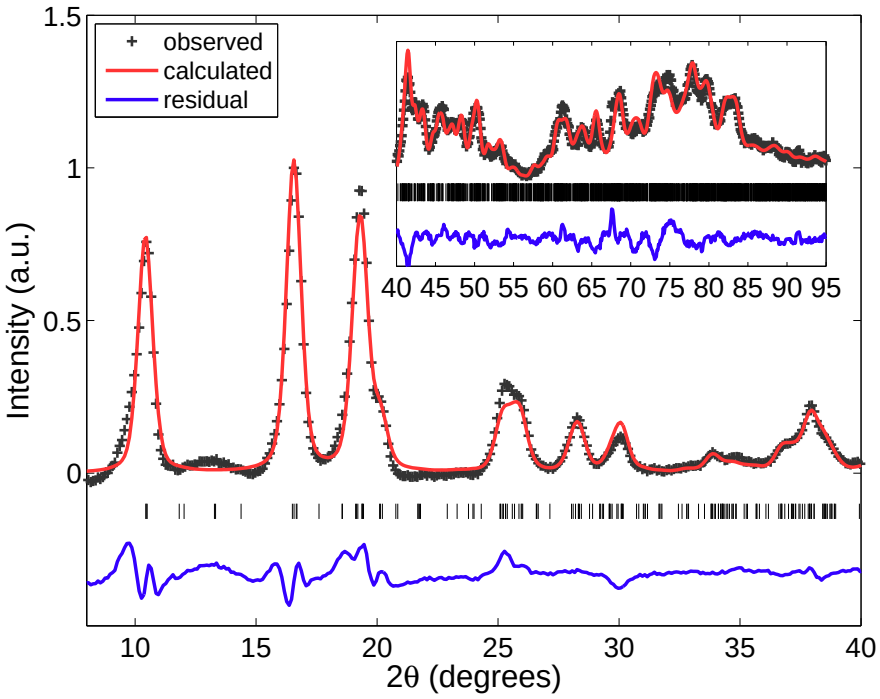

Figure 3.6: Final observed and calculated neutron diffraction profile for $Li_{12}C_{60}$ at 20 K (a = 9.8614(6) Å, b = 9.879(1) Å, c = 14.211(1) Å, $a = \gamma$ = 90°, β = 89.665(2)°, $Li_{10}C_{60}$, space group $P2_1/n$, R_{wp} = 6.52 %). The blue solid line shows the difference profile, and the tick marks highlight the allowed reflections.

pattern appears to depict the *fcc* structure, after a more careful study it was evident that the peaks at high angle can only be explained by a decrease of symmetry. A simulated annealing study of the pattern by using a primitive cell ($a = b = c$ = 13.981 Å and $\alpha = \beta = \gamma$ = 90°) and four C_{60} molecules as rigid bodies (located in the *fcc* positions), leads to a remarkable result: at the end of the computational routine, the C_{60} molecules were displaced in the same original positions of the *fcc* cell but with two different orientations (see Fig. 3.7(b)). At this stage of the analysis, the contribution of the alkali atoms was neglected, due to their low neutron cross-section. The final symmetry is well described in the $P2_1/n$ monoclinic group, achieved after a slight distortion of the *fcc* cell and rotation of fullerenes. The relative

Space group	$P2_1/n$
a	9.862
b	9.879
c	14.211
β	89.665 °
formula	$Li_{10}C_{60}$
R_{wp}	6.52 %
d_{Li-Li}	2.54 - 2.92 Å

Table 3.4: Refined parameters of $Li_{12}C_{60}$ from Rietveld refinement of neutron pattern at 20 K.

pseudo-cubic model can be achieved assuming a coordinate transformation to a tetragonal cell:

$$a = a'\sqrt{2} \qquad c = a,$$

where a' and a are the pseudo-cubic and the $P2_1/n$ lattice parameters, respectively. At this time, the structural model was refined and physically consistent positions for Li atoms were chosen by studying the solvent excluded surface around the volume occupied by the C_{60} molecules (assuming the solvent having a radius equal to the one of Li ion). The refined structure is displayed in Fig. 3.7(a). The Fourier map analysis excluded the presence of a lithium atom in the center of the octahedral void of the pseudo-*fcc* lattice. Conversely, a cluster of 5 Li atoms is formed centered in the pseudo-T_h void (see Fig. 3.7(c)) with an alkali atom fully occupying the center. The agreement for this model reaches the minimum value of $R_{wp} = 6.52$ %, with a chemical formula lower than $Li_{12}C_{60}$, due to the null occupancy of the pseudo-O_h void. In the refined model, the Li atom at the center of the cluster distances about 2.54 - 2.9 Å from the corners of the distorted tetrahedron. These distances are intermediate between the metallic bond (about 3 Å) and the hypothetical distance of two lithium ions (about 1.36 Å), but closer to those of the metal. Comparing this structure with the results of the Raman experiment, which shown a fullerene molecule charged with about 6 electrons (Fig. 3.4), is now possible to attribute a charge of about 4 electrons for the cluster, that in this way appears to be partially ionized.

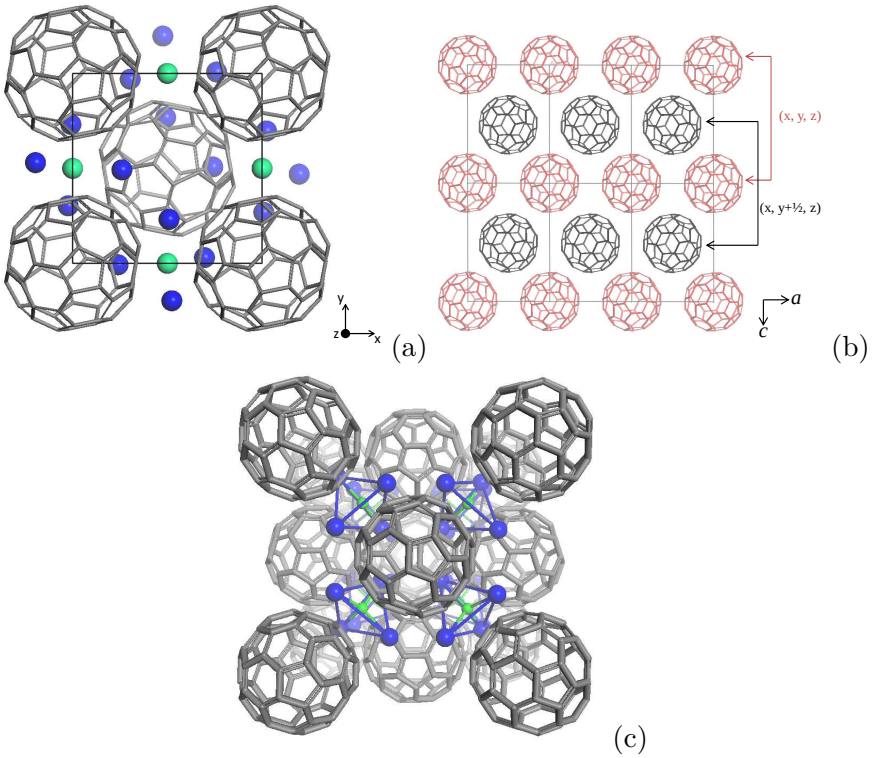

Figure 3.7: (a) Refined cell of $Li_{10}C_{60}$ (space group: $P2_1/n$, R_{wp} = 6.52 %). Green and blue spheres represent the lithium atoms. (b) View along the [010] direction: red and gray fullerenes belong to two different planes with molecules differently oriented. Lithium atoms are omitted for clarity. (c) The pseudo-cubic cell of $Li_{10}C_{60}$ with Li atoms linked in order to better display the tetrahedral cluster. Here the color of lithium atoms is maintained as in (a).

3.3 Study of the hydrogen sorption

The hydrogen absorption of the samples was investigated volumetrically by means of pcT (pressure, composition, Temperature) instrument [113]. Hydrogen/deuterium pressure (100-200 bar) was applied on the sample (200-400 mg) and subsequently a heating ramp of 0.5 °C/min was applied up to a temperature between 200 and 400 °C, depending on the experiment. The samples were kept at the final temperature between 1 and 67 h. The

amount of hydrogen absorbed was determined by the pressure change at known volumes and defined temperatures. In order to correct for the pressure increase in the heated sample holder a measurement consisting of a non absorbing silicon sample, occupying the same volume as the sample, was subtracted. After each hydrogenation experiment the hydrogen pressure was released from the samples. Hydrogen desorption was carried out either in vacuum ($<1 \cdot 10^3$ mbar) or at 1 bar of hydrogen by applying a heating ramp of 1 °C/min and by measuring the amount of desorbed hydrogen with a flow meter. Alternatively the pressure increase in a known volume was used to determine the amount of hydrogen. The $Na_{10}C_{60}$ and $Li_{12}C_{60}$ absorptions/desorptions were carried out at EMPA by Dr. Philippe Mauron using an home built dynamic pcT instrument while Li_6C_{60} was measured in Pavia by Dr. Chiara Milanese using a PCTPro-2000 (Hy-Energy) manometric instrument by Setaram.

3.3.1 Hydrogenation of $Na_{10}C_{60}$

The first hydrogen absorption measurement of $Na_{10}C_{60}$ was carried out on a multiphasic sample produced with the azide method. The starting material shows diffraction peaks corresponding to a major phase of *fcc* $Na_{10}C_{60}$ [64] and a minor phase of *bcc* Na_4C_{60} [60, 62], as can be seen in Fig. 3.8. The peak at $2\theta < 10°$ is typical of hexagonal distortion of C_{60}, previously observed also in Na_xC_{60} by Kobayashi *et al.* for x≥4 [63], and here is attributed to a minority phase. The peak at ∼10° is attributed to the (111) reflection of the fcc structure while the one at ∼11° is the (110) reflection of *bcc* Na_4C_{60}. By refinement of the as synthesized Na_xC_{60} with Le Bail analysis, a lattice parameter of $a = 14.49$ Å was calculated for the *fcc* majority phase, corresponding to $Na_{7.9}C_{60}$ when linearly interpolated [123] with the parameters of $Na_{5.9}C_{60}$ [59] and $Na_{9.7}C_{60}$ [64]. To determine the suitable working conditions, the first absorption was carried out on the synthesized sample under 200 bar of hydrogen pressure (heating rate 0.5 °C/min) and up to 350 °C and holding the $Na_{10}C_{60}$ at this temperature for 80 minutes before cooling. The measure of the absorbed hydrogen is

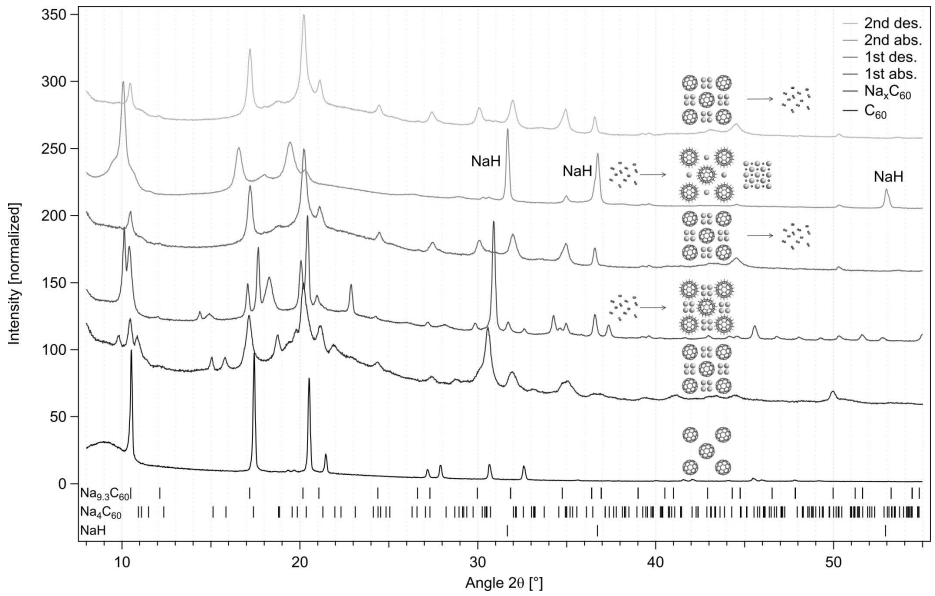

Figure 3.8: XRD patterns of C_{60} and Na_xC_{60} before and after the first and second hydrogen ab/de-sorption as measured at room temperature (the patterns are normalized and shifted in y-axis with a constant offset) [122].

reported as a function of temperature in graph of Fig. 3.9. The absorption process starts at about 150 °C which is significantly lower than for pure C_{60} [124]. A maximum amount of about 2 mass% H_2 is reached at 300 °C and above this temperature the sample starts the desorption process, also if the 200 bar pressure is still present. At the end of the experiment about 1.1 mass% H_2 was already absorbed by $Na_{10}C_{60}$. The XRD spectrum of this sample is shown in Fig. 3.8 (third from the bottom): after the first absorption the (1 1 1) peak of the *fcc* phase and the (1 1 0) of the *bcc* phase are downshifted meaning that the respective lattice now are expanded. The desorption measurement of this partially desorbed $Na_xC_{60}H_y$ was carried out in 1 bar of H_2 up to 400 °C (heating rate 1 °C/min) and the results are shown in Fig 3.10. The sample desorbs completely the 1.1 mass% H_2 in 2 subsequent processes: about 0.2 mass% are desorbed at ∼150 °C and full dehydrogenation is achieved at 250 °C. The second desorption presents a relatively sharp peak and finishes at ∼300 °C, reaching the maximum

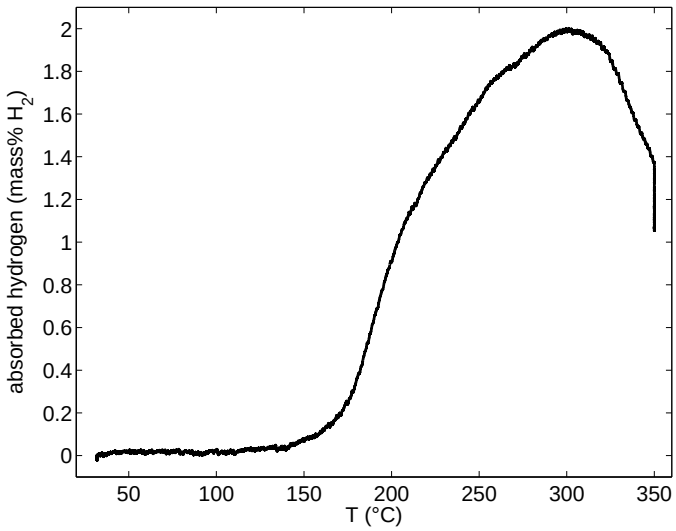

Figure 3.9: Absorbed hydrogen amount in $Na_xC_{60}H_y$ as a function of the temperature (heating rate 0.5 °C/min) during first absorption at 200 bar hydrogen [122].

value of 1.1 mass% H_2 indicating complete reversibility of this sample. The temperature of desorption is significantly lower with respect to hydrogenated C_{60} (treated at 400 °C in 120 bar H_2 for 50 h) which desorbs in vacuum above 400 °C (see Fig. 3.12(c-d)). After the second desorption, the peaks of

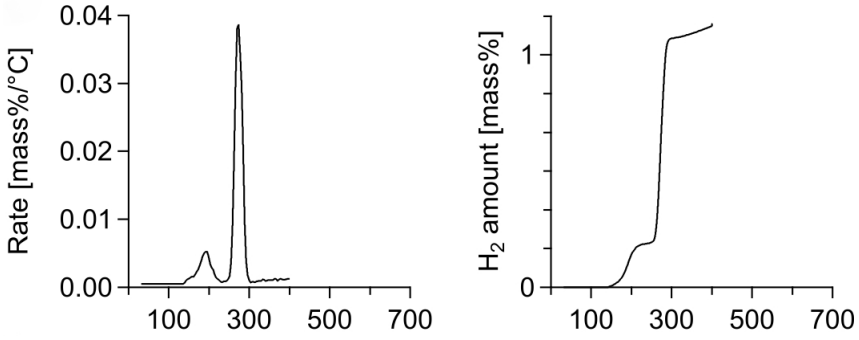

Figure 3.10: Desorption measurements in 1 bar H_2 of $Na_xC_{60}H_y$ that previously absorbed 1.1 mass% H_2. On the left the desorption rate is shown as a function of temperature while on the right the amount of desorbed hydrogen is reported in the same scale [122].

Na_4C_{60} phase disappear and the *fcc* phase has a lattice constant of $a = 14.49$ Å which is the same of the original structure ($Na_{7.9}C_{60}$), thus confirming the reversibility of the process.
A second hydrogenation was then made on the desorbed sample at 200 °C (0.5 °C/min) under 200 bar of H_2 and holding at this temperature for 67 h. As shown in Fig. 3.11, about 3.2 mass% H_2 were absorbed during the treatment. With this pressure the onset of hydrogenation starts already at ∼80 °C which is a relatively low temperature and significantly increase in rate above 150 °C. The full hydrogenation is not achieved immediately

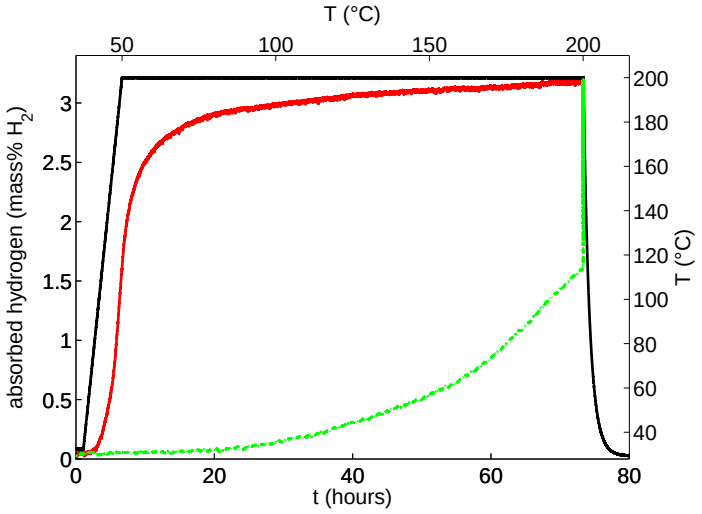

Figure 3.11: Absorbed hydrogen during the second hydrogenation of $Na_{7.9}C_{60}$ (200 °C, 200 bar H_2): left Y-scale: the amount of mass% H_2 absorbed is reported as a function of time (red solid line) and as a function of temperature (green dashed line). Right Y-scale: the thermal ramp is showed as a function of temperature (black solid line).

at 200 °C, while almost half of the total amount of hydrogen is absorbed during the temperature ramp. To gain the other ∼1.5 mass% the sample has to hold at 200 °C for almost 50 hours. The XRD spectrum of $Na_xC_{60}H_y$ after the second absorption is showed in Fig. 3.8 (second from the top). The second absorption was made at lower temperature than the first one, in order to avoid the partial desorption occurring a 300 °C, and on one single

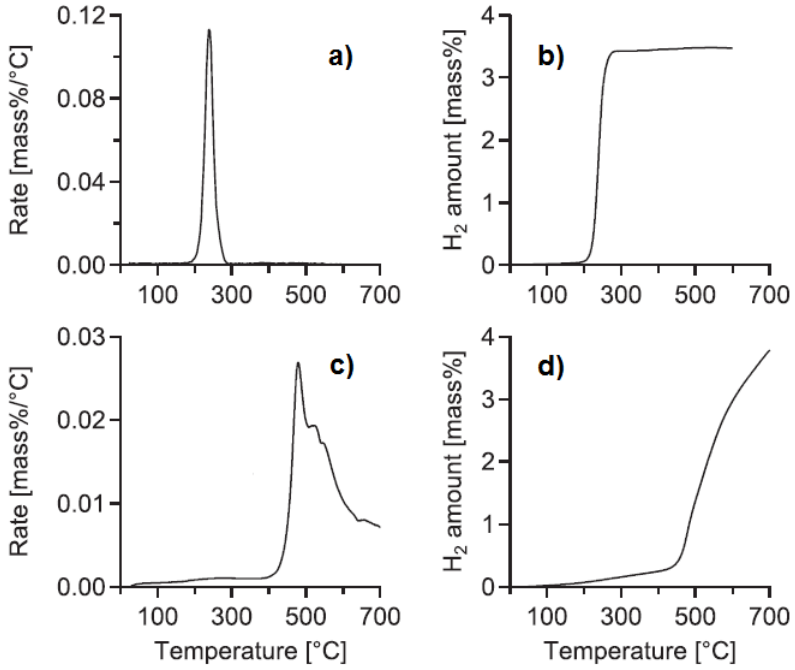

Figure 3.12: (a-b) rate of desorption and mass% desorbed hydrogen of $Na_xC_{60}H_y$ during the 5th desorption cycle in 1.8 bar H_2 up to 600 °C (heating rate 1 °C/min). (c-d) first dehydrogenation measurements for pure $C_{60}H_y$ in vacuum up to 700 °C (heating rate 2 °C/min) [122].

phase system. The most intense reflection at 2θ ∼11° presents 2 shoulders on the left and right proximity. Additionally sodium hydride (NaH) is also present as can be noted by the presence of typical reflections at 31.8, 36.8 and 53°. Since the other peaks are easily indexed with the $Fm\bar{3}$ space group, being the peak at ∼11° the (1 1 1), the 2 satellite reflections at low angle could be ascribed by the presence of a weak hexagonal distortion of a *fcc* structure. All the cubic peaks are downshifted resulting in a huge expansion of the lattice after the hydrogenation. The lattice constant of $Na_xC_{60}H_y$ was refined to be $a = 14.780(3)$ Å (Le Bail, $R_{wp} = 10.1$ %) which is significantly higher than 14.49 Å of $Na_{7.9}C_{60}$. The additional NaH could be formed during the hydrogenation by the deintercalation of Na from the hydrogenated sodium fulleride ($Na_8C_{60} \rightarrow Na_{8-x}C_{60} + Na$) and the

subsequent reaction with H_2 or it can be also created inside the structure of the hydrofulleride and successively segregated outside. It's well known that hydrofullerene tends to form *bcc* structures, like in the case of $C_{60}H_{36}$ which has a $Im\bar{3}$ symmetry with a lattice parameter of $a = 11.785(15)$ Å [96]. Moreover, if only Na reacted with hydrogen forming NaH with the following process:

$$Na_{10}C_{60}(s) + 5H_2(g) \Longrightarrow 10NaH(s) + C_{60}(s),$$

then the hydrogen absorbed would be ∼1.0 mass%. From these considerations it follows that the *fcc* phase formed after hydrogenation is likely still intercalated by a low stoichiometry of Na and the mechanism of reaction could be written as

$$Na_8C_{60} + H_2 \Longrightarrow Na_{8-x}C_{60}H_y + xNaH \tag{3.1}$$

The absorption/desorption process was repeated 5 times in order to study the reversibility of the system. The third and fourth cycle were performed at 100 bar hydrogen where 1.8 mass% and 0.4 mass% were absorbed at 200 °C (18 h) and 400 °C (12 h) respectively. The absorbed amount of hydrogen during the 5^{th} hydrogenation (not shown here) was 3.5 % (at 200 °C and 190 bar H_2 for 40 h) and it was completely discharged during the following desorption procedure (up to 600 °C, 1 °C/min, in a constant volume from vacuum to 1.8 bar), as can be seen in Fig. 3.12. Only one sharp peak of desorption is detected at about 220 °C (Fig. 3.12(a)): it is broader than in the first desorption because of the fact that the measurement wasn't done at constant pressure. The 600 °C temperature is relatively high for fullerene and the molecule can start to decompose. Nevertheless, a 6^{th} hydrogen cycle was reversible with 3.4 mass% H_2 (185 bar, 200 °C, 40 h) of hydrogen. The total amount of 3.5 mass% in $Na_{10}C_{60}$ corresponds to $C_{60}H_{34}$ and is very close in stoichiometry to $C_{60}H_{36}$ which is considered the most stable hydrofullerene molecule. However, to obtain the $C_{60}H_{36}$ fulleride starting from fullerite only chemical methods can be used (Birch reduction [90]). The

physical hydrogenation of pure C_{60} starts a very high temperature (above 300 °C in 190 bar H_2, 45 h), reaching about 2.5 mass% but the molecule decomposes during hydrogenation and dehydrogenation. Since NaH is a very stable phase (ΔH_f^0= -122.6 kJ/mol H_2) and decomposes at very high temperature (∼800 °C) the disappearing of NaH peaks after desorption could be attributed to the intercalation of NaH inside the hydrofulleride which allows a reduction of the energy barrier required for the dissociation ($Na_{8-x}C_{60}(s) + yNaH(s) \longrightarrow Na_8C_{60}(s) + \frac{y}{2}H_2(g)$), as suggested by Murphy *et al.* [58]. Ignoring the formation of NaH, the measured 3.5 mass% of hydrogen absorbed/desorbed in $Na_{10}C_{60}$ could be attributed to the following reaction:

$$Na_{10}C_{60} + 18H_2 \Longrightarrow Na_{10}C_{60}H_{36}.$$

This corresponds to about 3.7 mass% H_2. Supposing there is some deintercalation of NaH from the hydrofulleride, the reaction can be written as:

$$Na_{10}C_{60} + \left(\frac{36+x}{2}\right)H_2 \Longrightarrow Na_{10-x}C_{60}H_{36} + xNaH$$

and for $x = 4$ ($Na_6C_{60}H_{36}$) corresponds to 4.1 mass% of hydrogen which partially compensate the extra weight of Na. In comparison $C_{60}H_{36}$ has about 4.8 mass% hydrogen storage capacity.

3.3.2 Hydrogenation of lithium intercalated fullerides (Li_6C_{60} and $Li_{12}C_{60}$)

The study of hydrogen storage in Li_xC_{60} was undertaken after the encouraging results achieved on $Na_{10}C_{60}$. The advantages of lithium fullerides are mainly due to the following reasons:

- ≻ Lithium is lighter than sodium so that $Li_xC_{60}H_y$ will have gravimetrically more hydrogen absorbed than its equivalent sodium fulleride.
- ≻ Lithium ion has smaller radius than Na^+ and this fact facilitates the diffusion into C_{60}
- ≻ It is possible to achieve high stoichiometries of Li in Li_xC_{60}, while

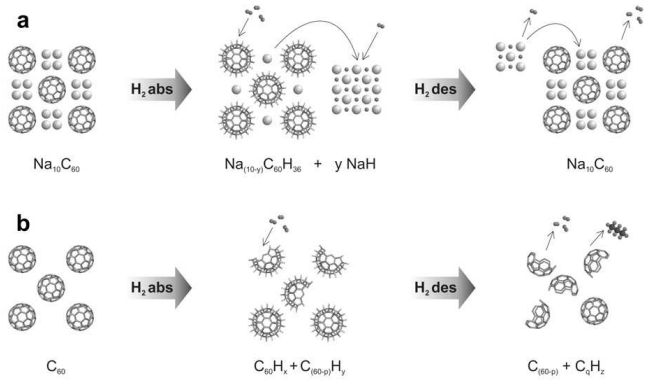

Figure 3.13: (a) Schematic representation of the mechanism of the reversible hydrogenation of $Na_{10}C_{60}$. During the hydrogenation, Na atoms reacts with H_2 and are deintercalated as sodium hydride while C_{60}^{n-} forms $C_{60}H_{36}$ hydrofullerene. Desorption process takes place through the decomposition of NaH which reintercalates into $Na_{(10-x)}C_{60}$. (b) Hydrogenation mechanism of pure C_{60} which decomposes during hydrogenation and dehydrogenation for high hydrogen content [122].

sodium doesn't exceed the x = 10-11 in Na_xC_{60}.

Nevertheless, there are also disadvantages in using lithium:

- The phase diagram of Li_xC_{60} for different x is not well known for $x >$ 4.
- The study of powder diffraction of lithium fullerides is not easy due to the very low scattering factor of lithium both with X-rays and neutrons.

The study of hydrogen storage in Li_xC_{60} compound was also stimulated on one part by the well established knowledge of these system by the group of the Carbon nanostructures Laboratory of Parma (which resulted in the publication of several articles in the past years [125, 56, 52, 50]) and on the other part by the recent publication of Teprovich *et al.* [100] which found that lithium-doped fullerane ($Li_x - C_{60} - H_y$) under optimized conditions can reversibly desorb up to 5 mass% H_2 with an onset temperature of ∼270 °C. In particular they measured the maximum uptake for a $Li : C_{60}$ molar

ratio of 6:1. Moreover, theoretical studies on $Li_{12}C_{60}$ demonstrated that this system could in principle achieve an approximate gravimetric density of molecular hydrogen of 9 mass% at low temperature by means of a small binding energy, useful for applications [75].
In this study, differently from what was done by Teprovich *et al.*, the starting material was pure Li_xC_{60} phase (in this work studied for $x = 6$ and 12). The material was synthesized as reported in paragraph 3.1. Laboratory diffraction of Li_6C_{60} and $Li_{12}C_{60}$ are reported in Fig. 3.2 and discussed in the same paragraph. The hydrogen absorption of $Li_{12}C_{60}$ and Li_6C_{60} was respectively measured by Dr P. Mauron (EMPA) and Dr. C. Milanese (Pavia H_2 Lab). Since Li_6C_{60} had been previously studied in depth by Teprovich *et al.* [100], only the first hydrogen absorption at 350 °C (0.5 °C/min, 100 bar H_2) was made, in order to check if the maximum amount of absorbed hydrogen was the same of the published one. The measure of hydrogen absorption of Li_6C_{60} is reported in Fig. 3.14. The measure was carried out in 100 bar of hydrogen pressure with a fast thermal ramp of 5 °C/min and up to 350 °C. The onset of hydrogen absorption starts below 100 °C and when the system reaches the maximum temperature (350 °C) the absorbed hydrogen is already about 2.8 mass% (in the case of $Na_{10}C_{60}$ was about 1.6 mass% at 200 °C and 200 bar H_2). After 10 hours about 5 mass% of H_2 is stored and maintained also at room temperature and ambient pressure. X-rays diffraction of the hydrogenated sample (not shown) confirms the formation of the *bcc* phase of the hydrofulleride, as reported by Teprovich *et al.* in the same experimental conditions [100].

The absorption of $Li_{12}C_{60}$ was carried out at the EMPA laboratories. Since the sample was scheduled to be studied with neutrons, deuterium was used instead of hydrogen. The first step of absorption was made under 190 bar D_2 with a thermal ramp of 0.5 °C/min up to 225 °C (the data are reported in Fig. 3.15). The onset of deuteration starts around 60-70 °C and at the maximum temperature (225 °C) the absorbed deuterium is equivalent to ∼3 mass% of H_2. An additional 1.5 mass% H_2 is absorbed during the isotherm (45 hours) leading to a total of 4.5 mass% H_2. Cooling down the sample to room temperature under pressure doesn't produce any

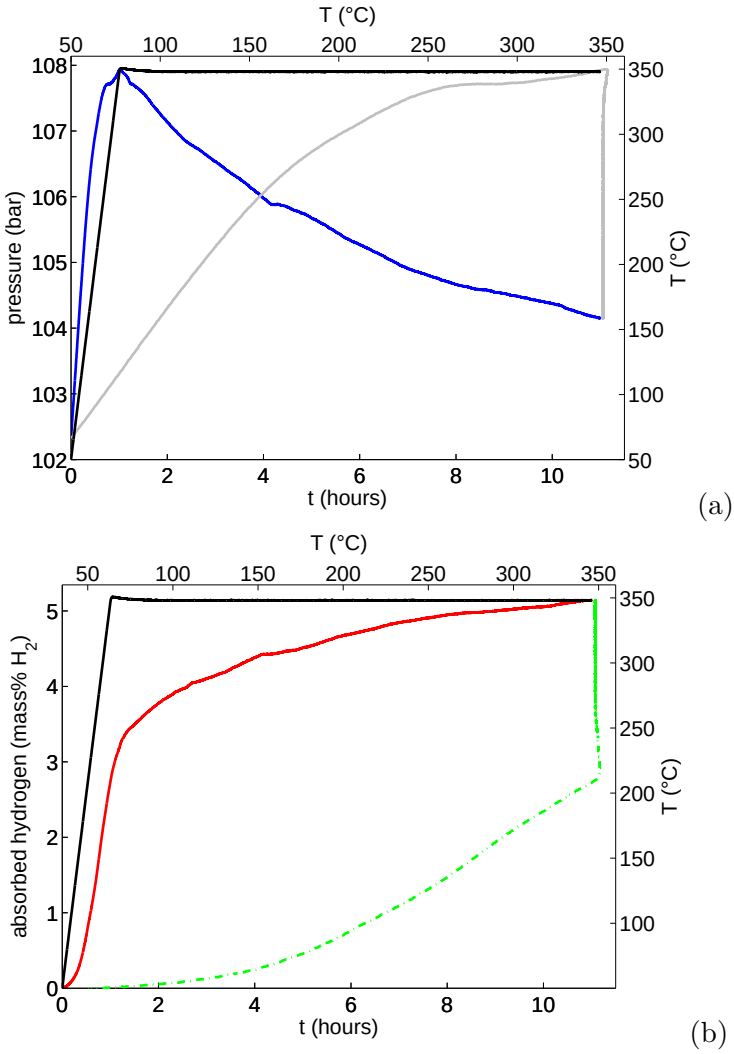

Figure 3.14: (a) Variation of pressure during the hydrogen absorption of Li_6C_{60} reported as a function of time (blue line) and temperature (grey line). The adopted thermal ramp (5 °/min) is displayed as a black line as a function of time. (b) Absorbed hydrogen during the hydrogenation of Li_6C_{60} (350 °C, 100 bar H_2): left Y-scale: the amount of mass% H_2 absorbed is reported as a function of time (red solid line) and as a function of temperature (green dashed line). Right Y-scale: the thermal ramp is showed as a function of temperature (black solid line).

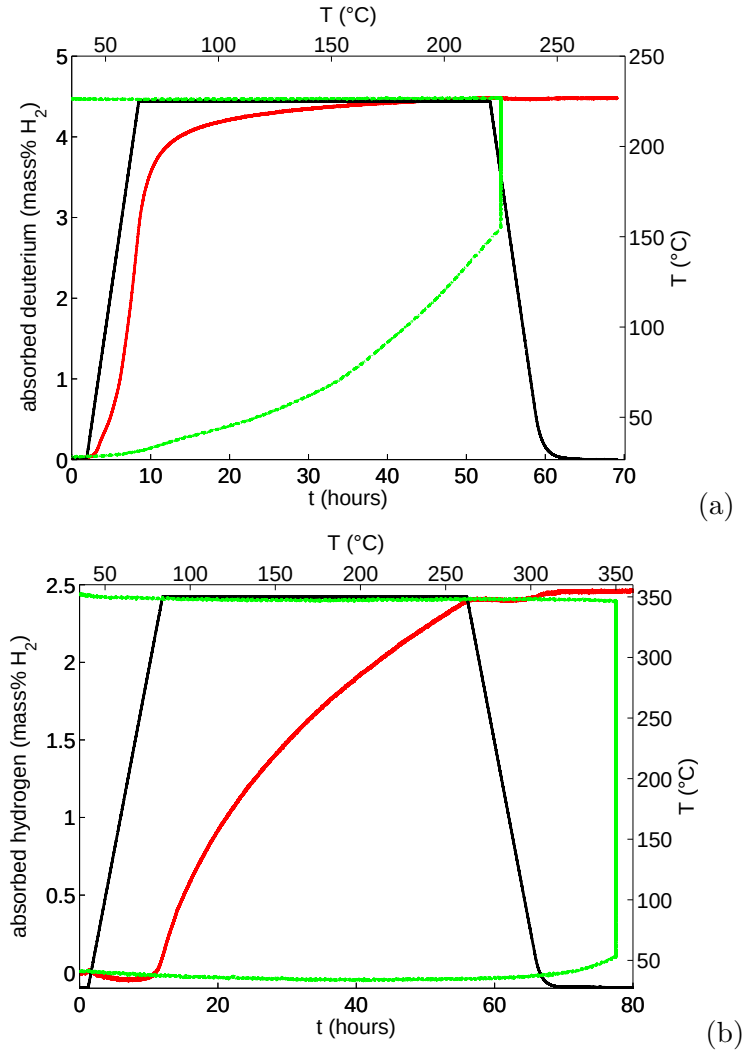

Figure 3.15: (a) Absorbed deuterium (expressed in terms of mass% hydrogen) during the hydrogenation of $Li_{12}C_{60}$ (225 °C, 190 bar H_2): left Y-scale: the amount of equivalent mass% H_2 absorbed is reported as a function of time (red solid line) and as a function of temperature (green dashed line). Right Y-scale: the thermal ramp is showed as a function of temperature (black solid line). (b) The same measure for pure C_{60} (350 °C, 185 bar H_2):

desorption. At the end of the cycle the pressure decreased from 190 to 173 bar. A second step of hydrogenation of $Li_{12}C_{60}$, made in similar conditions

to the one of the first absorption of Li_6C_{60}, up to 350 °C at 0.5 °C (under 100 bar D_2), led to an additional absorption of 0.5 mass% H_2, reaching about 5 mass% total (like for Li_6C_{60}). As can be seen in Fig. 3.16, after the hydrogenation at 225 °C the crystal considerably increases the lattice constant but without apparently changing its structure, which remain *fcc*, although it is difficult to establish because of the broad peaks. At the same time, the formation of a fraction of lithium deuteride (LiD peaks at 38.3 and 44.6°) is evident. The lattice constant of the *fcc* structure changes from $a = 13.880(9)$ Å for pure $Li_{12}C_{60}$ to $a = 14.394(2)$ Å if refined with Le Bail analysis using the structure of *fcc*-C_{60}. While the spectrum of $Li_{12}C_{60}$ was detailed also at high angle (see the zoom in Fig. 3.16), after the first hydrogenation only the low angle peaks are appreciable. This is indicative of disorder in the final structure, maybe due to different stoichiometries of hydrofullerene inside the crystal (*e.g.*: different y of $C_{60}D_y$, coexisting within the same cubic structure). After the second step of hydrogenation (the XRD is not shown here but can be found in [126]) the LiD phase is still present, the final structure of the $Li_{12}C_{60}H_y$ hydrofulleride becomes *bcc* and the lattice constant was refined to be $a = 11.79(2)$ Å, which is close to the one of $C_{60}D_{36}$ hydrofullerite [94, 96] ($a = 11.7(1)$ Å) and similar to $a = 11.924(2)$ Å determined for $C_{60}H_{41}$ (MER Corp.). Moreover the peaks are sharper and well defined.

Unfortunately, since the experimental conditions were quite different, a direct comparison between the absorption of $Li_{12}C_{60}$ and Li_6C_{60} can't be done. Nevertheless, a significative comparison can be done between the Li_xC_{60} and $Na_{10}C_{60}$. In fact, around 300 °C and under 200 bar H_2 the $Na_{10}C_{60}$ started the desorption process while the $Li_6C_{60} - H_y$ and $Li_{12}C_{60} - D_y$ are already hydrogenated/deuterated (also if the pressure is lower, *e.g.*: the desorption should occur at lower temperature). This is indicative of the fact that, while it is true that on one part they absorb more hydrogen than Na_xC_{60}, on the other the hydrogenated/deuterated phases of $Li_{12}C_{60}$ and Li_6C_{60} are more stable against dehydrogenation. If we consider the formula units of the sodium and lithium intercalated fullerides and their respective amounts of stored hydrogen, ignoring the formation

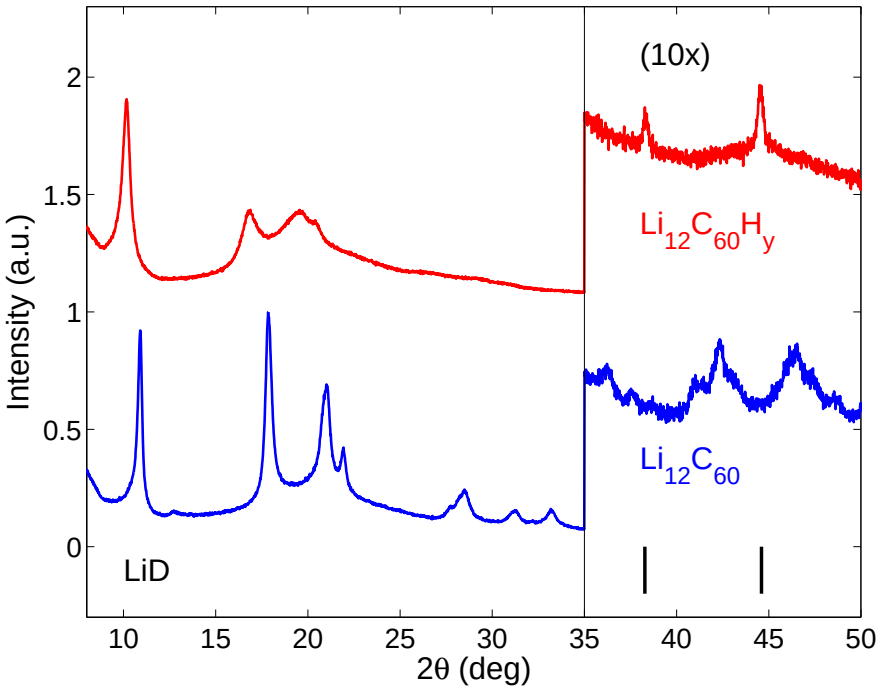

Figure 3.16: XRD patterns of the as synthesized $Li_{12}C_{60}$ (blue) and $Li_{12}C_{60}H_y$ (red) after the first step of deuterium absorption (225 °C, 190 bar). Patterns are normalized and shifted on y-axis.

of hydrides, we can approximately estimate the final stoichiometries of the formed hydrofullerides. As already said for Na_xC_{60} (3.5 mass% H_2 stored), the hydrogenated phase should corresponds to $Na_{10}C_{60}H_{34}$. Similarly, the hydrogenated phases of Li_6C_{60} (5 mass% H_2) and the $Li_{12}C_{60}$ (4.5 mass% H_2) corresponds to $Li_6C_{60}H_{40}$ and $Li_{12}C_{60}H_{38}$ respectively. All these stoichiometries have to be considered as an upper limit to the effective hydrogen stored in the fulleride. In fact, it was always detected a small amount of hydrides, formed during the hydrogen absorption process. As discussed in paragraph 3.3.1 the hydrogenation process of $Na_{10}C_{60}$ can be described by equation 3.1.

The formation of $C_{60}H_y$ is confirmed for $Na_{10}C_{60}$ and $Li_{12}C_{60}$ also by FT-IR experiment (as shown in [122] and [126]) that shown the presence of C-H stretching modes at 2800-3000 cm^{-1} for $Na_{10}C_{60}$ and the C-D stretching

modes at 2158 and 2105 cm^{-1} for $Li_{12}C_{60}$. The formation of $C_{60}H_y$ in Li_6C_{60} is confirmed also by Teprovich *et al.* [100]. Assuming that $C_{60}H_{36}$ ($C_{60}D_{36}$) is the more stable compound formed during the hydrogenation, in the case of Li_xC_{60} (where $x = 6$, 12) the absorption process can be described by:

$$Li_xC_{60} + \frac{(36+\delta+\alpha)}{2}H_2 \Longrightarrow Li_{(x-\alpha)}C_{60}H_{(36+\delta)} + \alpha LiH, \tag{3.2}$$

meaning that during hydrogenation/deuteration the Li atoms deintercalate from Li_xC_{60}, such as Na in $Na_{10}C_{60}$, and form LiD/LiH, in which deuterium/hydrogen is bound to Li and at the same time in the remaining $Li_{(x-\alpha)}C_{60}$ phase, hydrogen/deuterium covalently binds to C_{60}. If only the lithium reacted with hydrogen, in the process:

$$Li_{12}C_{60} + 6D_2 \Longrightarrow 12LiD + C_{60},$$

then the hydrogen capacity would be only 1.5 mass% H_2. Conversely, assuming a complete lithium deintercalation ($\alpha = 6$, 12 for Li_6C_{60} and $Li_{12}C_{60}$ respectively) and the formation of $C_{60}H_{36}$ ($\delta = 0$), then the material would have a total hydrogen capacity of 5.6 mass% ($12LiD + C_{60}D_{36}$). In comparison $C_{60}H_{36}$ has a hydrogen storage capacity of 4.8 mass% H_2. Therefore, the intercalation of Li not only improves the sorption properties but also increases the hydrogen storage capacity.
The reversibility of this process was investigated in desorption by means of neutron diffraction and will be discussed in paragraph 3.4.

3.4 *in-situ* neutron diffraction

In this chapter the investigation of samples by means of *in-situ* deuteration neutron diffraction is reported. A cylindrical 6 mm stainless steel sample holder (wall thickness of 1 mm) was filled inside a He glove box (< 1 ppm of O_2 and H_2O) with about 300-400 mg of sample and measured in

high intensity mode with $\lambda = 1.8857$ Å. The cell is placed, connected to a high pressure system, into a radiation-type furnace mounted on the HRPT diffractometer. During measurements, temperature was increased up to 450 °C. Diffraction patterns were collected in the angular range 2θ = 5-165° with a typical acquisition time of ∼3 hours subdivided into acquisition steps of few minutes each. Samples were stabilized until the normalized total counts of neutrons became constant, in order to monitoring the possible transitions occurring during the treatment, and only the data collected when the normalized counts were constant in time have been integrated.

3.4.1 *in-situ* study of $Na_{10}C_{60}$

The first investigated sample was $Na_{10}C_{60}$. The experiment was performed under 100 bar of D_2 and during treatment the temperature was increased up to 350 °C. The collected spectra are reported in Fig. 3.17. The analyzed sample was made in similar way of those measured by means of pcT, Raman and XRD but comes from a different batch. The first spectrum from the bottom was recorded on the as synthesized sample and clearly shows the *fcc* symmetry of $Na_{10}C_{60}$ which is present as single phase. Le Bail analysis at 25 °C confirms the $Fm\bar{3}$ space group and gives a lattice constant of a = 14.542(2) Å with an agreement factor of R_{wp} = 5.18 %, corresponding to $Na_{8.8}C_{60}$ when linearly interpolated with the parameters of $Na_{5.9}C_{60}$ [59] and $Na_{9.7}C_{60}$[64]. The most intense peaks at 53.95 and 63.18° and the smallest at 30.34 and 43.55° are originated by the steel sample holder and were not taken into account during analysis. As can be seen in Fig. 3.17, the insertion of 100 bar of D_2 at room temperature does not influences the overall spectrum. Rising the temperature up to 150 °C doesn't change significantly the recorded spectrum except for the little increasing in the lattice constant (see inset of Fig. 3.17) due to the natural thermal expansion. The pattern recorded at T = 250 °C, in presence of 100 bar of D_2, shows an abrupt change in the lattice constant of the cubic structure, with the simultaneously appearance of new reflections in the diffraction profile. The lattice parameter increased by $\Delta a \approx 0.4$ Å (Le Bail analysis*:* $a = 14.930(8)$

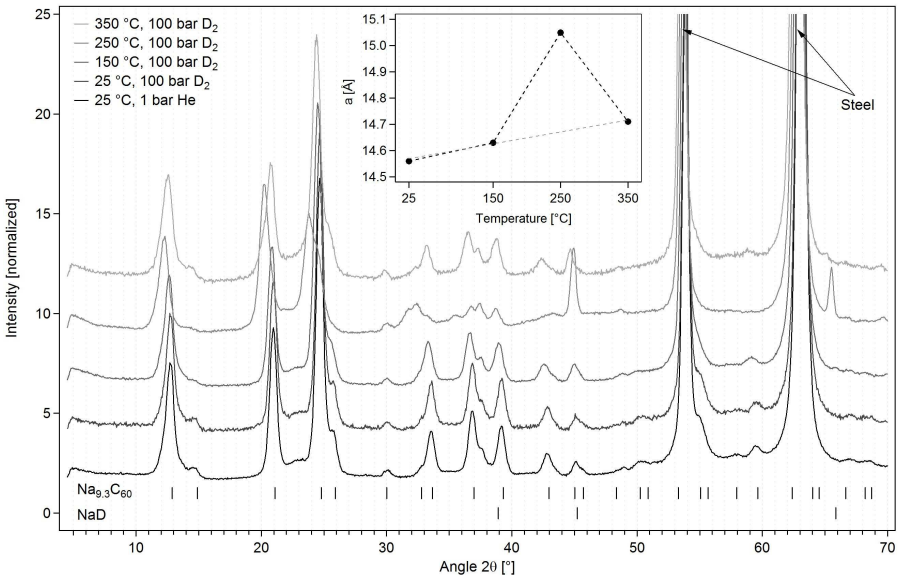

Figure 3.17: Neutron powder diffraction patterns of $Na_{10}C_{60}$ for different temperatures (patterns are normalized and shifted on y-axis). inset: lattice parameter, a, as a function of temperature for the data fitted with the $Fm\overline{3}$ cell of $Na_{9.3}C_{60}$ structure (dashed lines are guides for the eyes) [122].

Å, $R_{wp} = 11.16\%$) and such a big enlargement can't be explained by normal thermal expansion. The (311) peak at $\sim$24° is now splitted in two different peaks at 23.74° and 24.41° and at the same time new peaks at 44.9 and 65.5° arise. The last two can be easily ascribed by the presence of NaD phase while the splitting of the (311) is attributed to the formation of an expanded cubic structure (the one at 44.9°) which is accompanied to the original one (peak at 24.41°), already present during the experiment, and undergoing the normal thermal expansion. Since no Na peaks were detected in the original phase of $Na_{8.8}C_{60}$, the formation of sodium deuteride is accompanied by a leakage of sodium from the original cubic structure, as can be noted by the decrease of the relative intensities of the (311) and (222) peaks. However, the changing in relative intensities compared with the anomalous expansion of the lattice cannot be attributed to the simple de-intercalation of metal ions: while the structure already resemble the *fcc* phase of $Na_{10}C_{60}$, differ-

ences in the relative intensities could also be attributed to the introduction of deuterium atoms inside the cell, which modify the coherent scattering form factor of C_{60} due to the formation of hydrofullerene ($C_{60}D_y$) [90]. The fact that the (311) is splitted at 250 °C is attributed to the not complete reaction of the system in the time-scale of the experiment which produces the formation of two phases: the new deuterated $Na_{(10-\alpha)}C_{60}D_{(36\pm\delta)}$ and the original $Na_{8.8}C_{60}$ which slowly undergoes hydrogenation (the intensity of the two peaks was evolving during the experiment and the spectrum shown in Fig. 3.17 is the integration of the data collected when the normalized total counts of neutron was apparently constant in time). As a support to this interpretation is also the slow increase in mass% H_2 stored by $Na_{10}C_{60}$ occurring during the hydrogen absorption when the temperature was already 200 °C, as can be seen in Fig. 3.11 (about 1.6 mass% H_2 was slowly stored during the ∼60 hours of isotherm). By increasing the temperature from 250 to 350 °C the NaD peaks disappear (although the melting point of NaH is at 425 °C and it's known to decompose at 800 °C), the lattice constant deceases, going back to the initial linear trend (see inset of Fig. 3.17). This is in good agreement with what observed in the pcT experiment where, during the first hydrogenation, the sample starts the desorption process above 300 °C, also under 200 bar of H_2. The sample, cooled down at room temperature (avoiding reabsorption of deuterium) under 100 bar, was measured again at 300 K and the spectrum perfectly superimposed to the one of the as synthesized $Na_{8.8}C_{60}$, meaning that the deuterated sample underwent complete desorption at 350 °C.

Due to the fact that NaD peaks disappear when the sample was heated above 300 °C, it is supposed that NaD reacts with $Na_{(10-a)}C_{60}D_{(36\pm\delta)}$ phase by reintercalating sodium released from deuteride and this process involves reduction of $C_{60}D_{(36\pm\delta)}$ back to the original C_{60} in a reversible way:

$$Na_{10}C_{60} + \frac{(36+\alpha\pm\delta)}{2}D_2 \Longleftrightarrow Na_{(10-\alpha)}C_{60}D_{(36\pm\delta)} + \alpha NaD.$$

The exact number of α and δ is not easy to be determined from the neutron (or X-ray) diffraction, in fact, the refinement of the deuterated/hydrogenated fulleride will need to know the geometry of the deuterated/hydrogenated fullerene molecule. In the case of $C_{60}D_{36}$ ($C_{60}H_{36}$), for $\delta = 0$, there are roughly 10^{13} possible isomers but only few of them are considered effectively stable. In particular, only the symmetries T, T_h, S_6 and D_{3d} [93, 127, 94, 92] were assumed good candidates. A depth investigation of the $C_{60}H_y$ geometries will be discussed in paragraph 3.5.

3.4.2 Study of the $Li_{12}C_{60}$

The *in-situ* deuterium absorption of $Li_{12}C_{60}$ was investigated from room temperature up to 350 °C under 170 bar of D_2 (the maximum value allowed during the experiment but anyhow near the one of 190 bar adopted during the first pcT absorption), in a similar way to that illustrated at the beginning of paragraph. Unfortunately, the reaction of the system with deuterium in these condition was too slow to be recorded during the time-scale of the experiment (3 hours). The resulting spectra (not reported here) do not show significative differences and only the appearance of LiD peaks in the spectrum recorded at 350 °C deserves a note. While the XRD spectrum of deuterated $Li_{12}C_{60}$ of Fig. 3.16 showed the presence of LiD already after absorption at 225 °C, it should be noted which in that case the sample was held at 225 °C for almost 40 hours before cooling it down and measuring at room temperature. This fact may actually be of great relevance in discriminating the segregation of the phase of LiD from the formation of the $Li_{(12-\alpha)}C_{60}D_{(36+\delta)}$. In fact, if after 3 hours of deuteration at 250 °C the LiD is not already formed, while pcT measurements showed that at 225 °C and 190 bar of D_2 about 3 mass% of hydrogen were already stored in the sample and the presence of LiD was found with XRD only at the end of the treatment (when 4.5 mass% H_2 was achieved), it is possible to speculate that the formation of the hydride takes place only after the hydrogenation of C_{60}. Therefore, the formula of equation 3.2 for $Li_{12}C_{60}$ can be splitted

in the 2 subsequent steps:

$$Li_{12}C_{60} + \frac{y}{2}D_2 \Longrightarrow Li_{12}C_{60}D_y,$$

$$Li_{12}C_{60}D_y + \frac{(36 - y + \alpha + \delta)}{2}D_2 \Longrightarrow Li_{(12-\alpha)}C_{60}D_{(36-y+\delta)} + \alpha LiD.$$

Measurements of *in-situ* Inelastic Neutron Scattering (not shown here) recently carried out at IN4 beamline (ILL - Grenoble, France) seem to confirm this hypothesis. The data were collected from room temperature up to 250 °C under 100 bar of H_2 (High Resolution mode, $\lambda = 2.4$ Å). From the first raw analysis, the Density of State $G(\omega)$ evidenced a peak located at 150 meV (which is typical for the C-H bending modes in the hydrofullerite) at ∼180 °C, followed by the rising of the Li-H reticular mode, located near 100 meV starting around 225 °C. The same result can be expected also in the case of the hydrogenation of Li_6C_{60} and $Na_{10}C_{60}$, although a direct proof is missing. Discrimination between the process of hydrogenation of the C_{60} and the subsequent segregation of lithium hydride/deuteride is of fundamental importance in understanding the mechanism of hydrogenation and will be discussed in more detail in paragraph 3.6.

The sample of $Li_{(12-\alpha)}C_{60}D_y$, deuterated at 350 °C and 100 bar of D_2 (second step, other batch), was investigated by means of neutron powder diffraction and its desorption was monitored *in-situ* between room temperature and 450 °C. The sample was measured in a 6.3 mm diameter vanadium sample holder with a wall thickness of 0.25 mm, previously sealed in glove box in ∼1 bar He. The recorded neutron patterns are shown in Fig. 3.18(a), for different temperatures during the temperature ramp. At room temperature two phases can be easily identified: LiD phase and a *bcc* phase similar to $C_{60}D_{36}$ [94, 96] as already detected by XRD. The lattice parameter of $a = 11.848(1)$ Å determined at RT is similar to the one of 11.8(1) Å given by Hall *et al.* [94, 96] for $C_{60}D_{36}$. Up to a temperature of 325 °C the patterns looks similar and the only differences are due to the normal thermal expansion. At 350 °C all the LiD reflections disappear, although the melting point and desorption temperature of LiH are at 680 [128] and 943 °C

(calculated from thermodynamic values [128]), respectively. The *bcc* phase is not present anymore and it results evolved into a new crystal structure, with lower symmetry. Up to a temperature of 450 °C there is no major change in the spectra anymore. The new structure formed at 450 °C is still under investigation.

In Fig. 3.18(b) the lattice parameters of LiD and the $Li_{(12-\alpha)}C_{60}D_{(36+\delta)}$, fitted with the Le Bail method from the respectively cubic structures, are plotted as a function of temperature up to 325 °C. Due to thermal expansion the lattice parameters increase for LiD and $Li_{(12-\alpha)}C_{60}D_{(36+\delta)}$ by heating up from RT to 325 °C. Unlike the hydride, for $Li_{(12-\alpha)}C_{60}D_{(36+\delta)}$ the lattice expansion deviates from a linear behavior between 300 and 325 °C as desorption occurs in this temperature range and the lattice parameter decreases again. Due to the fact that, integrating the pattern, for a fixed temperature part of kinetic information got lost, normalized total counts (S_{tot}) for each pattern are therefore plotted in Fig. 3.19, as a function of time. Changing in S_{tot} is proportional to deuterium desorbed from sample, since D is essentially contributes to the total scattering cross section. It can be seen that desorption starts at 300 °C and that it is essentially terminated at 350 °C at a value of $S_{tot} = 70$ %. A calculated value of S_{tot}, considering the sample geometry (cylindrical sample, annular vanadium sample holder) with constant packing and mass densities of the sample [129], for the formal reaction $C_{60}D_{36} + 12LiD \rightarrow Li_{12}C_{60}$ gives $\Delta S_{tot} = 71\%$ after desorption, which is very close to the measured one.

These measurements suggest that, while in the first step of hydrogenation (225 °C, 190 bar, 4.5 mass% H_2 absorbed) only a fraction of lithium reacts with deuterium and segregates in form of LiD, when the "full" hydrogenation is achieved (after the second step protracted at 350 °C, 100 bar, 5 mass% H_2 absorbed), almost all (but not all) lithium is deintercalated from the $Li_{(12-\alpha)}C_{60}D_y$ ($x \lesssim 12$) forming the hydride. Assuming that the final hydrofullerene is $C_{60}D_{36}$ ($C_{60}H_{36}$), if the final product was

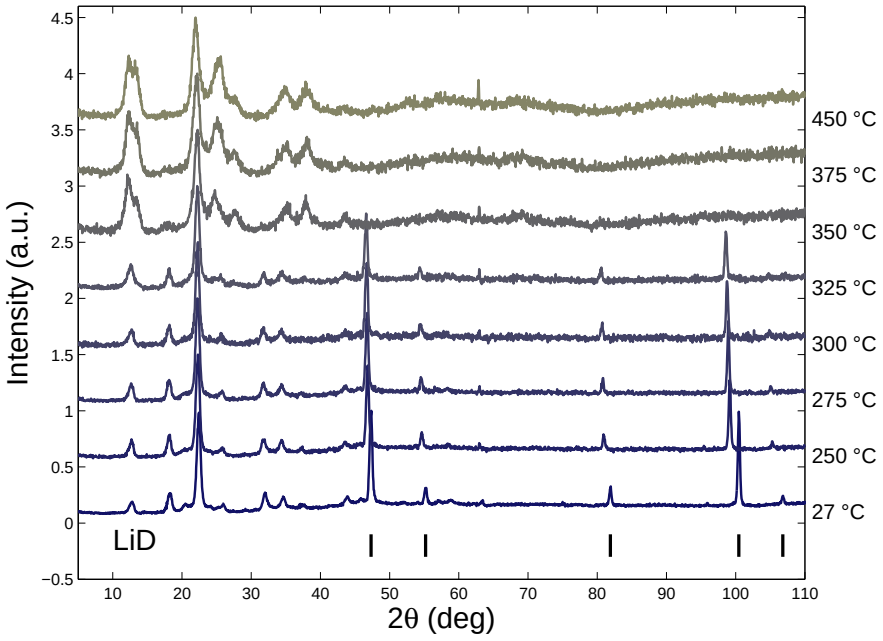

(a)

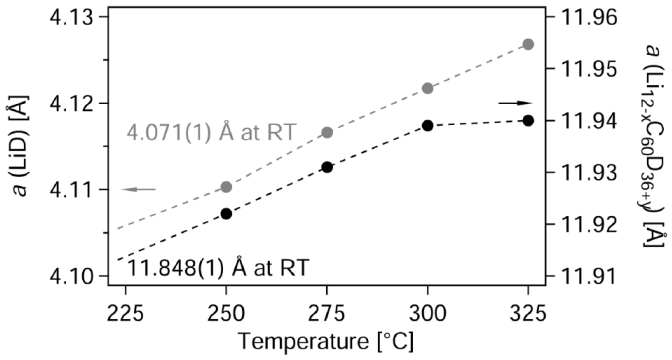

(b)

Figure 3.18: (a) Evolution of the lattice constants of *bcc*-$Li_{(12-\alpha)}C_{60}D_y$ phase (right Y-axis) and LiD (left Y-axis) after the second step of deuteration of $Li_{12}C_{60}$ (355 °C, 100 bar D_2) reported as a function of temperature from 225 °C to 325 °C [126].

$\alpha LiD + Li_{(12-\alpha)}C_{60}D_{36}$ for the 2 steps of hydrogenation it could be written:

$$\begin{array}{ll} Li_{12}C_{60} + \frac{38}{2}D_2 \Rightarrow 2LiD + Li_{10}C_{60}D_{36} & (1^{st} - step: \ 4.5 \ mass\% \ H_2) \\ Li_{12}C_{60} + \frac{44}{2}D_2 \Rightarrow 8LiD + Li_4C_{60}D_{36} & (2^{nd} - step: \quad 5 \ mass\% \ H_2) \end{array} .$$

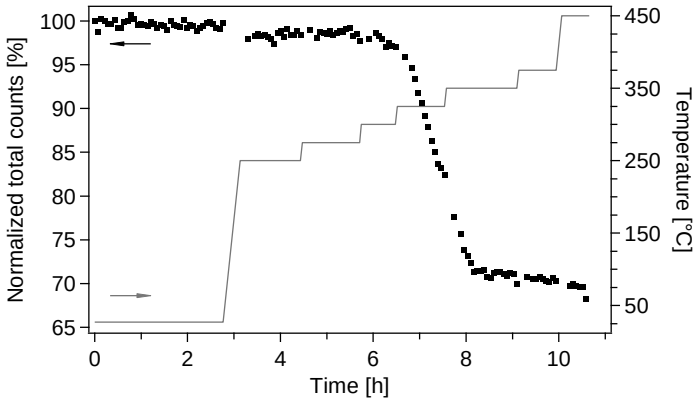

Figure 3.19: Normalized total counts (Left Y-axis:) and sample temperature (Right Y-axis) as function of time [126].

Conversely, if all the lithium reacted with deuterium (hydrogen) forming $12LiD$, then the final hydrofullerene would be $C_{60}D_{33}$ ($C_{60}H_{33}$). Actually, it is rather difficult to deduce the exact stoichiometries relying on these data and the error is certainly high.

As already said in the paragraph 3.3.2, lithium hydrofullerides turns out to be less stables against hydrogenation, although they can store more hydrogen. While $Na_{10}C_{60}$ reversibly stored its maximum amount of hydrogen without changing the initial *fcc* structure, also after the 5^{th} cycle, the same can't be said for the $Li_{12}C_{60}$ hydrogenated up to 350 °C, for which after desorption at 450 °C a new structure is formed.

3.5 Real space investigation of intercalated hydrofullerides

The structural study of hydrogenated/deuterated phases of alkali intercalated fullerides is complicated by many factors: first of all the low grade of symmetry in all the hydrogenated samples makes it difficult to analyze the diffraction patterns. While the space group of these crystals can be qualitatively attributed by indexing the most intense peaks at low angle and performing a Le Bail analysis, comparing the agreement factor of the

most probable choices, a structural refinement is hampered by the poor crystallinity, inferable, for example, from the large FWHM of the peaks and to the broadening of spectrum at high angle. Also in the case of lithium fullerides (as it was for sodium fulleride) the possible isomers of $C_{60}D_y$ are a cosmic number and this makes conclusions about the value of y purely speculative. Furthermore, there is also to take into account the possibility (which is consistent) that there is a distribution $P(y)$ of hydrofullerenes ($C_{60}H_y$), as indeed found, by means of mass spectroscopy, in some hydrogenated fullerenes [130, 88, 100]. In this complicated scenario, a quantitative

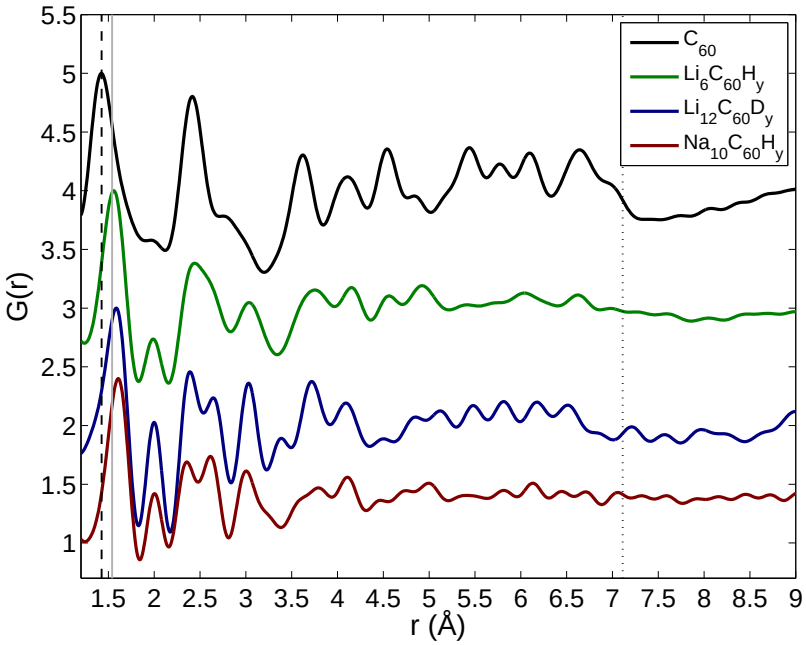

Figure 3.20: Pair Distribution Functions measured for pristine C_{60} and of hydrogenated/deuterated Li_6C_{60}, $Li_{12}C_{60}$ and $Na_{10}C_{60}$. The black dashed line at 1.44 Å highlights the average $C-C$ bond length in pristine C_{60}. The gray solid line underline the typical sp^3 $C-C$ distance. The black dotted line corresponds to the maximum $C-C$ length inside pristine C_{60}. Data are normalized and rigidly shifted in vertical for a better view.

analysis is hard to perform. Nevertheless, the low crystalline character of these materials can be exploited, in order to get informations about the

short-range order, in a total scattering experiment. In fact, while in the case of classic diffraction the long range order is easily measurable due to reflection of Miller planes, which is more efficient for low values of the h k l indexes, the short-range order is detectable only at high value of the exchanged momentum (Q) and if the crystal displays disorder the relative peaks (at high angle) are too broad to be deconvoluted and also too damped in a X-ray experiment. Conversely, the diffusive scattering (which is consistent for high values of Q) can be exploited to extrapolate the Pair Distribution Function (PDF). For this purpose, total scattering experiment was carried out on the hydrogenated/deuterated compounds on the high energy scattering beamline, ID15B (ESRF, Grenoble). The experimental setup was optimized in order to have scattering window from $Q_{min} = 0.5$ Å^{-1} and up to $Q_{max} = 21.8$ Å^{-1}. The wavelength was fixed at $\lambda = 0.22235$ Å (∼55.8 keV) and the area detector was placed very close to sample (20 cm). The sample was sealed in a boron-silicate capillary of 0.7 mm diameter and its background was removed from calculations with PDFgetX3 [106], in order to extract the PDF. The average values of $f(Q)$ were calculated by using atoms and stoichiometries adopted for the synthesis (*e.g.*: for $Li_{12}C_{60}$, 60 atoms of C and 12 atoms of Li were considered).

The extracted PDFs of pristine fullerite and hydrogenated Li_6C_{60}, $Li_{12}C_{60}$ and $Na_{10}C_{60}$ are displayed in Fig. 3.20. After the hydrogenation the PDF appears deeply changed for all samples: remarkable is the shift of the first peak toward higher values of r. This is the shortest measurable distance inside the compound (since the $C-H$ or $C-D$ bond lengths are too short to be detected in a PDF experiment) and is indicative of the $C-C$ bond length. This length should be 1.44 Å, on average, in pristine C_{60} and, in fact, the peak is centered at ∼1.44 Å for it. The broadening is mainly due to thermal motions and to the fact that this is not the only nearest neighbors distance whereas a distribution from 1.367 to 1.463 Å is present. In case of hydrogenated/deuterated samples, the binding between carbon atoms and hydrogen/deuterium turns the sp^2 hybridization to sp^3 which increases the average bond length up to ∼1.4-1.6 Å. This clearly happens in hydrogenated/deuterated alkali intercalated fullerides, where the first peak

is centered at 1.56 Å for $Li_6C_{60}H_y$, 1.59 Å for $Li_{12}C_{60}D_y$ and 1.61 Å in the case of $Na_{10}C_{60}H_y$. Moreover, is interesting to see that the PDF is limited between the diameter of a C_{60} molecule and no peaks are observed above 7.1 Å. This is attributed to rotational diffusion of the fullerene molecule for pristine C_{60}, which mediates to zero all the intermolecular correlations, while it is indicative of long range disorder in case of hydrofullerides (where no rotations are expected).

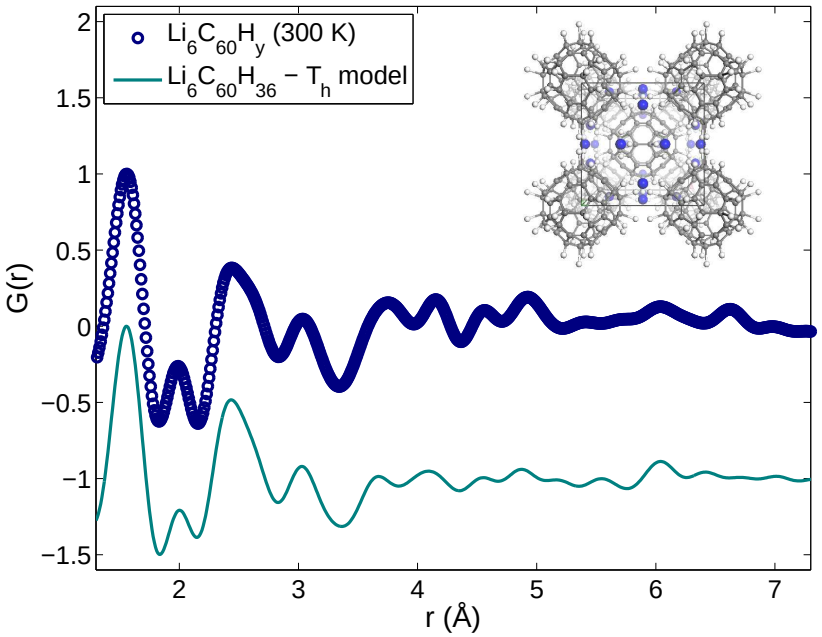

Figure 3.21: Measured room temperature PDF of $Li_6C_{60}H_y$ compared with the model fitted for the T_h isomer of $Li_6C_{60}H_{36}$ in the $Im\bar{3}$ cell. Inset: refined structure with Li (blue), carbon (gray) and hydrogen (white) atoms.

The extracted PDF of hydrogenated Li_6C_{60} (350 °C, 100 bar H_2) is displayed in Fig. 3.21. The diffraction pattern of this sample was in perfect agreement with the one previously published by Teprovich *et al.* [100], when a *bcc* arrangement of the hydrogenated C_{60} molecule was deduced by indexing the most intense peaks. The lattice parameter (a = 11.95 Å) results slightly increased from the one fitted for $C_{60}H_{36}$ (a = 11.785(15) Å [94, 96]) and this can be ascribed by the steric hindrance exerted by the

Li atoms, still intercalated inside the structure. The geometry of $C_{60}H_y$ in $Li_6C_{60}H_y$ will be reflected on its packing and the space group of the crystal will have to be consistent with the molecule point group. Several $Li_6C_{60}H_{36}$ models were simulated and compared with the data. In particular, D_{3d}, S_6, T and T_h punctual symmetries comply with the $m\bar{3}$ symmetry of the $Im\bar{3}$ space group and are considered to be the most stable isomers of $C_{60}H_{36}$ [95]. Hall *et al.* found that for $C_{60}D_{36}$ the most stable isomer was the one owning a T symmetry [96]. However, in the case of $Li_6C_{60}H_y$, the isomer who better describe the PDF is the one owning a T_h symmetry. For this reason, a $Im\bar{3}$ structure in which the center of a $T_h - C_{60}H_{36}$ was located in the *2a* (000) position and the Li atoms were placed in the *12e* ($x\frac{1}{2}0$) special positions, was simulated and the model was relaxed by fitting the position of atoms (according to the symmetry constraints) and the instrumental parameters (for a technical description of latter refer to the PDFgui user manual [107]). The fitted model is displayed in Fig. 3.21 and compared with experimental data. The profile qualitatively follows the $G(r)$, however, the agreement factor (R_{wp} = 33.01 %) is still too high and this is most probably due to the presence of different species of $C_{60}H_y$ and widespread disorder, which make a further analysis not feasible. The refined structure is showed in the inset of Fig. 3.21. It's important to observe how the presence or absence of hydrogen does not significantly alter the theoretical profile and for this reason its position in the refined model is only indicative. In the case of Li, although its small scattering factor, the influence on the profile function is more pronounced. However, the most significative contribution to the $G(r)$ is given by the position of carbon atoms which clearly distort the smoothed shape of C_{60} to a more sharpened molecule. This is indicative of sp^3 hybridization which involves the carbon bound to hydrogen. In particular, it was found that two of the five carbons of a pentagon ring are still sp^2 hybridized, with a bond length of 1.326 Å, while the three others are sp^3 hybridized and bound to hydrogen. The hexagon which shares two neighbors carbons with the double bond of the pentagon ring is slightly distorted toward a *boat* conformation and binds 4 hydrogens. The hexagon ring who shares only one carbon with one of the

two sp^2 pentagonal carbons shows a more pronounced distortion towards a *chair* conformation. Its carbon atoms are arranged in an alternated sp^2-sp^3 configuration and the sp^3 types bind 3 hydrogens.

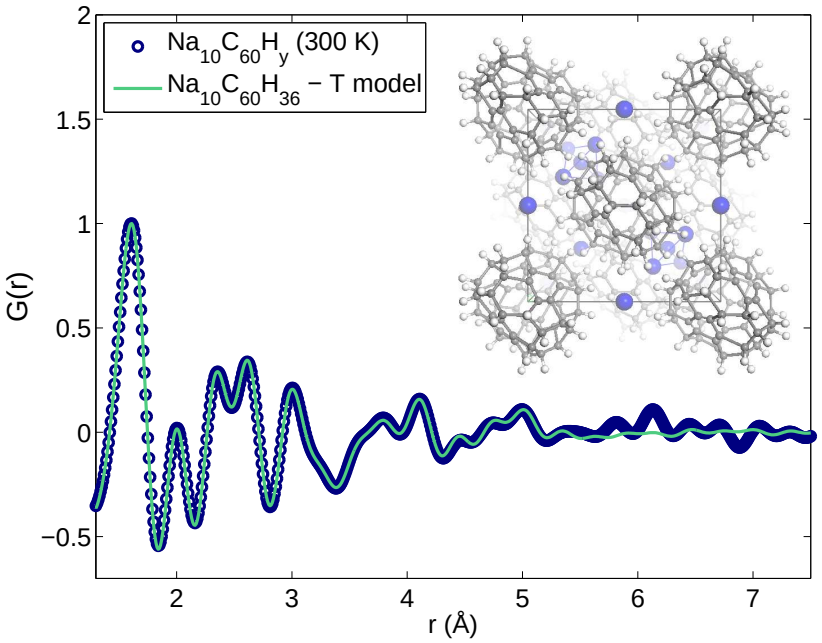

Figure 3.22: Measured room temperature PDF of $Na_{10}C_{60}H_y$ compared with the model fitted for the T isomer of $Li_6C_{60}H_{36}$ in the $F23$ cell. Inset: refined structure with Na (blue), carbon (gray) and hydrogen (white) atoms.

The PDF of hydrogenated $Li_{12}C_{60}$ presents features very similar to that of hydrogenated $Na_{10}C_{60}$, in particular for the position of the first 5 peaks. The refinement of $Li_{12}C_{60}H_y$ PDF is still in progress at the time of this work, but a model for the hydrogenated $Na_{10}C_{60}$ have been proposed: in fact, the analysis of the sodium hydrofulleride is simplified by the higher scattering factor of Na with respect lithium. Diffraction pattern of this compound is reported in Fig. 3.8 (2^{nd} absorption, 200 °C, 200 bar H_2). The structure for this phase is qualitatively *fcc*, although a minor hexagonal distortion is possible. A secondary NaH phase is also present and is, in principle, to take into account in calculations. A first attempt to refine the PDF was carried on a *fcc* arrangement of T_h isomers of $C_{60}H_{36}$ with Na ions occupying the

free volume of the cell in the *8c* and *4b* Wyckoff positions. The adopted cell has the $Fm\bar{3}$ space group and the lattice parameter was fixed to $a = 14.78$ Å, as refined from XRD data using the *fcc* cell of C_{60}. This model was not convincing and the shape of hydrofullerene did not resemble the PDF extracted for this compound. A more depth refinement improves the R_{wp} but leads to non physical results. A good refinement is achieved by starting from the T isomer of $C_{60}H_{36}$. In this case the $Fm\bar{3}$ space group can't be adopted due to the non centrosymmetric character of the T isomer, which is indeed well represented inside a $F23$ space group. By letting $a = 14.78$ Å and simulating the free volume accessible to a sphere of $r = 0.95$ Å (Na^+), the space left in the cell resides in the *4d* ($\frac{3}{4}\frac{3}{4}\frac{3}{4}$), *4c* ($\frac{1}{4}\frac{1}{4}\frac{1}{4}$), *4b* ($\frac{1}{2}\frac{1}{2}\frac{1}{2}$) and *16e* ($xxx$) Wyckoff positions. The refinement of this model is in good agreement with the measured PDF, as shown in Fig. 3.22, and a final $R_{wp} = 10.9$ % has been reached. The $T - C_{60}H_{36}$ isomer is slightly distorted respect the non intercalated compound [96] and is characterized by the presence of 4 non hydrogenated benzene rings. In the *fcc* packing these hexagons are faced along the [111] direction leaving a large space in four of the eight tetrahedral voids. This space can be filled by a cluster of five Na atoms, as shown in the inset of Fig. 3.22. The secondary NaH phase, detected by means of X-ray diffraction, was not detected in the PDF data and was therefore considered negligible.

3.6 The μSR study of the hydrogen storage mechanism in lithium and sodium fullerides

To follow the mechanism of hydrogenation of an absorbing system one has in principle to study separately the interaction of hydrogen molecule and atom. The *in-situ* diffraction and H_2 absorption experiments have been very useful in determining the final step of hydrogenation for Li_xC_{60} and Na_xC_{60}, allowing to understand that the intercalation of C_{60} with high stoichiometries of alkali metals (Li and Na) promotes the dissociation of H_2, also at moderate temperature. The final product is an alkali intercalated

hydrofullerides ($M_{x-\alpha}C_{60}H_{36\pm\delta}$) and it was found that the deintercalation of hydrides takes place only at the end of the process. In order to understand how hydrogen atoms are splitted from H_2 and subsequently interact with fulleride, the µSR technique has been used.

In addition to normal magnetic interactions that a muon can follow stopping into matter, briefly described in paragraph 2.3, in some cases it is also able to form paramagnetic species. When positive muons (μ^+) are implanted into insulating/semiconducting materials, they can bind an electron forming muonium ($Mu = \mu^+e^-$), a light isotope of hydrogen (equivalent on a chemical point of view). In metals, the formation of muonium atom is avoided due to effective screening of muon charge carried out by the Yukawa potential, which replaces the unscreened (electrostatic) Coulomb potential. The threshold of electron density at which bound states should appear has estimated to be $n_c \sim 3 \cdot 10^{22} cm^{-3}$. In some systems, like quartz (insulator), the Mu is very stable and is the only species which is formed [131]. In others, like graphite (semimetal with a small density of carrier, $n \sim 3 \cdot 10^{18} cm^{-3}$), when it is formed is so unstable that immediately reacts: binds to the plane and loses its electron, yielding a 100 % diamagnetic non decaying muon precession [132]. For these reasons, quartz and graphite are commonly used as reference materials in µSR experiments. In some cases, muonium atom can further interacts with an electron forming the negatively charged "hydride" ion (Mu^-), as happens in lithium hydride where the Mu^- occupies an H^- vacancy site [133]. Especially in organic π-systems, there is also the intermediate chance that Mu atom interacts with an aromatic carbon (owning a π-orbital) by binding to it and forming an adduct radical (ion/molecule with unpaired valence electrons).

Since the discovery of fullerite and superconducting fullerides, the µSR technique has been widely used to characterize the magnetic properties of these materials. The first study on pure C_{60} was made by Kiefl *et al.* [134] in low transverse field. Three distinct signals were observed: a small diamagnetic fraction and two muoniated species. About 12 % of them owning a large hyperfine parameter (4341(24) MHz), very close to the value for free muonium in vacuum (4463.3 MHz [135]), and a second signal (∼80 %) with

an isotropic hyperfine parameter of 325 MHz, typical of muoniated radicals. The former was attributed to a quasi-free muonium residing at the center of C_{60} (endohedral Mu, or $Mu@C_{60}$), where a minimum in the electrostatic potential is expected, and the latter was found to be a muonium bound to a carbon atom, exohedrally to C_{60} ($Mu - C_{60}$). When the same experiment was carried out on alkali doped fullerides *fcc*-A_3C_{60}, A_4C_{60} and *bcc*-A_6C_{60} ($A = Na$, K, Rb), it was found that only 2 species could be formed: 60-70 % of diamagnetic muons, which localize interstitially to fulleride lattice, and a small fraction of endohedral muonium, ~ 6 % [47, 136]. The production of radicals in alkali doped fullerides was determined to be suppressed, in both metal and insulating environments, due to the charged state of fullerene molecule (C_{60}^{n-}). Also in the case of superconducting K_3C_{60}, Na_2CsC_{60} and Rb_3C_{60} the formation of endohedral muonium was observed in the normal (metallic) state and the spin-exchange events between endohedral Mu and conducting electrons was found to be very weak, thus confirming the isolated nature of $Mu@C_{60}$ [136]. Although the formation of radicals in C_{60} was an important event, especially when one considers the implications for the hydrogen storage, at that time this had not aroused much interest, while great value was given to formation of endohedral muonium. This is mainly due to the fact that the community involved in these researches was basically interested in the electronic properties of C_{60}.

In the following section it will be shown how the formation of radicals on C_{60} can be retrieved when fullerite is intercalated with clusters of alkali metals and a possible mechanism of hydrogenation will be proposed [137]. At the time of the experiment only the Li_6C_{60} and the $Na_{10}C_{60}$ phases were available (in the pristine and hydrogenated form), while the synthesis of $Li_{12}C_{60}$ was still in progress. Nonetheless, results found for the four studied samples could be easily extended also for $Li_{12}C_{60}$.

3.6.1 The µSR experiment on $Na_{10}C_{60}$ and Li_6C_{60}

Zero and longitudinal magnetic field (ZF and LF) experiments were performed on the EMU spectrometer at the ISIS-Rutherford Appleton labora-

tory. About 350-400 mg of sample was pressed and sealed in an air tight aluminum cells closed by kapton windows. The windows has the double use as a sealant system with the purpose of keep the sample in a protected environment and as a medium for slowing the incoming muons allowing them to thermalize. For the latter reason a calibration with different thickness of kapton (usually in the order of 10^2 µm) is necessary so as to ensure that all the muons stop inside the sample. The bottom of the sample holder is coated with a silver slab (silver is diamagnetic with a very small nuclear momentum and doesn't change the muons polarization) in order to catch muons stopping outside the sample. The sample is made of pressed powder with large area and small thickness. The full asymmetry was determined with a transverse field measurement performed at room temperature on a pure silver plate and the total asymmetry was estimated to be $A_0 = 22.74(1)$ %. Since a fraction of the muon beam end up on the mask of the cell, it is necessary to measure the baseline of asymmetry due to that muons that end off the sample. This background was measured in transversal field on a quartz slab covered with a silver mask of the same diameter of the sample. Since quartz produces 100 % of muonium, all the muons stopping inside the space used for the sample give a missing fraction. The Zero Field asymmetries of pristine and hydrogenated Li_6C_{60} and $Na_{10}C_{60}$ are reported in Fig. 3.23. Both pristine and hydrogenated fullerides show basically two different components: the first one is a slowly decaying fraction, which was fitted with different decay functions and the fitting is reported in the graph as solid (dashed) lines for the pristine (hydrogenated) samples. The interpretation of this decays will be discussed later in this section. The second component is not directly visible in Fig. 3.23 since is possible to detect only by looking at the evident missing fraction which reduces the initial data asymmetry to a value lower than the instrument full one (A_0), which is reported as black dashed horizontal line at 22.74 %. The presence of a missing fraction indicates that the precession frequency of the correspondent fraction of muons exceeds the instrument pass-band ($\nu_{max} \sim 13$ MHz).

In absence of strong magnetic phenomena, this is the fingerprint of hyperfine interaction of a muon with an unpaired electron either in isolated

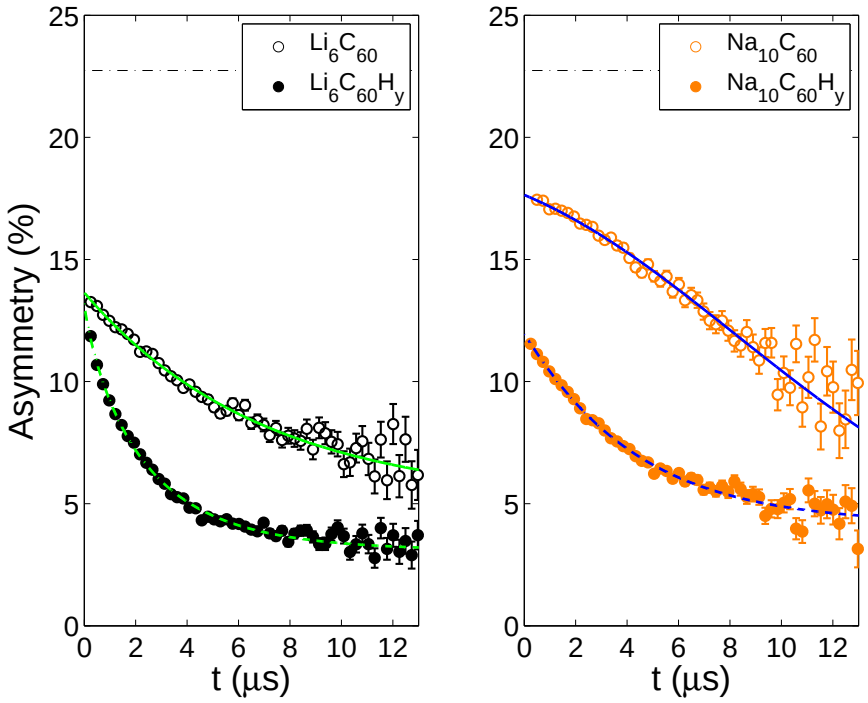

Figure 3.23: Zero field muon spin relaxation in pristine and hydrogenated Li_6C_{60} (left) and pristine and hydrogenated $Na_{10}C_{60}$ (right), measured at 5 K. Fitting curves for pristine (hydrogenated) samples are reported as solid (dashed) lines. Li_6C_{60} and $Na_{10}C_{60}H_y$ data have been fitted with a Lorentzian decay, $Na_{10}C_{60}$ with Gaussian and $Li_6C_{60}H_y$ according to a stretched exponential lineshape. The full asymmetry is represented as a black dashed line at 22.74 %.

muonium or in a muon substituted radical. Since it was known that metal intercalated fullerides could stabilize only the endohedral Mu and no radicals were expected, the first hypothesis was that in this case the missing fraction could be attributed to $Mu@C_{60}$. It has to be pointed out that the for pristine and hydrogenated Li_6C_{60} the initial asymmetry is about 40 % lower in amplitude than A_0 and also in the case of $Na_{10}C_{60}$ the hydrogenated sample has a similar missing fraction (while for the as synthesized crystal it is slightly smaller). Such big values of missing fraction are indicative of a significative fraction of muons forming muonium, while only ∼5-7 % of

the signal in fullerite and A_xC_{60} compounds was attributed to formation of $Mu@C_{60}$ [47, 134, 136]. So there are two possibilities:

- ≻ all the muons involved in the missing signal form endohedral Mu, as occurs almost for Na_2CsC_{60}, Rb_3C_{60}, K_3C_{60}, K_4C_{60} and K_6C_{60} [47, 136],
- ≻ for some reason, for Li_xC_{60} and Na_xC_{60} ($x \geq 6$) the production of radicals is not suppressed anymore.

In order to understand which paramagnetic species are formed in the samples it is necessary to repolarize the missing fraction by means of a longitudinal field. In fact, the hyperfine coupling between the muon and the paramagnetic electron can be estimated by the field dependence of the initial muon polarization. In case of isotropic coupling (as for free muonium, as it shown if Fig. 2.3(a) and (b)), by applying a field in the order of few thousand gauss parallel to the initial muon spins, $\mathbf{B}\| \langle \mathbf{I}_\mu(0) \rangle$, the muon and the electron spins can be decoupled and the average muon polarization at the time of the β decay is increased. The initial polarization goes from 50 % at zero field to a full 100 % at high longitudinal fields which fully decouple the muon and the electron. The functional behavior has the form:

$$P = \frac{1}{2} \cdot \left[1 + \frac{x^2}{1+x^2} \right], \tag{3.3}$$

where $B_{hyp} = A_\mu/(\gamma_e + \gamma_\mu)$ is the hyperfine field (the effective magnetic field exerted by the muon on the electron) and its value is about 1580 G for free muonium, $x = B/B_{Hyp}$. B_{hyp} could be considerably lower than 1580 G if the electron captured by the muon is delocalized around many nuclei (adduct radicals). Moreover, if the hyperfine interaction was anisotropic, like it is observed in most of the radicals, the zero field polarization would be quenched from 50 % to zero and equation 3.3 assumes the approximate form $P = x^2/(1+x^2)$ [138]. The repolarization of the muon spin for the four different samples is shown in Fig. 3.24. It is clear that the application of a field much lower than the hyperfine field of free Mu is sufficient to

fully repolarize the missing asymmetry in all the cases, since the expected inflection for free muonium at $1.58 \cdot 10^3$ G is not observed and at this field the polarization is already at 100 %. This demonstrates that the missing

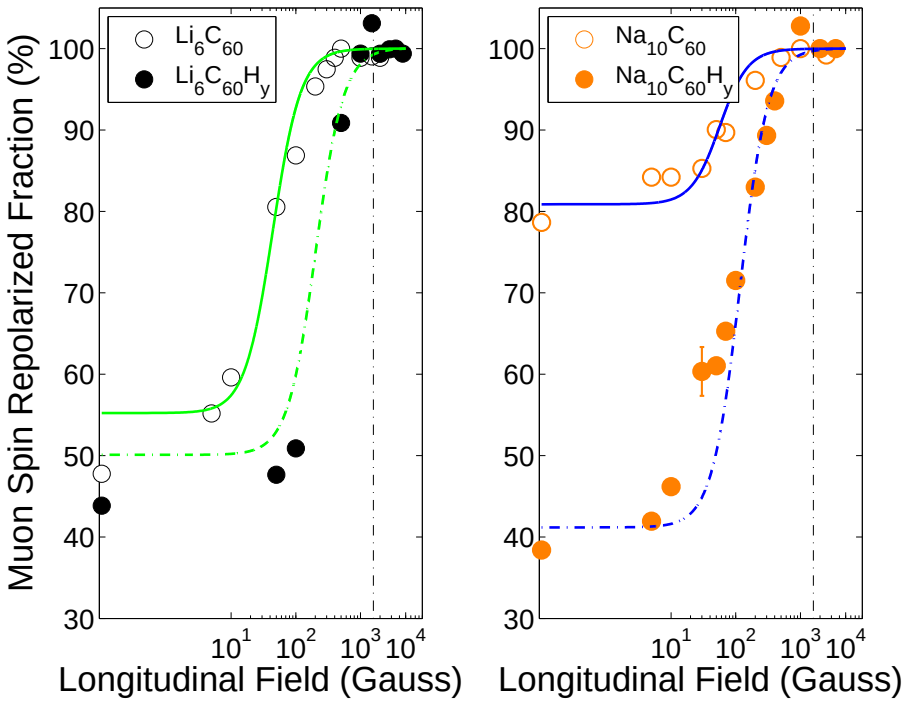

Figure 3.24: Muon spin repolarization experiment in pristine and hydrogenated Li_6C_{60} (left) and $Na_{10}C_{60}$ (right). The repolarized asymmetries have been fitted (here shown by solid/dashed lines) with equation 3.4 [116]. The vertical black dashed line represents the hyperfine field for free muonium.

fraction is due to the formation of radicals while no endohedral muonium is produced [139], contrary to what expected for alkali intercalated fullerides. The reaching of 100 % repolarization in Fig. 3.24 at the highest applied longitudinal field (*e.g.* to the full polarization measured in a transverse field experiment on a reference Ag sample) moreover guarantees that no other muon thermalization process contributes to the observed missing fraction.

The repolarization curves have been tentatively fitted with the function

$$P_{exp} = P_D + A_{rad} \cdot \left(\frac{x^2}{1+x^2} \right), \tag{3.4}$$

where P_D is the fraction of diamagnetic muons observed in zero field experiment while A_{rad} represents the amplitude of the radical fraction. Since the C_{60} crystal structure is described by many inequivalent carbon atoms (unlike many other fullerides the presence of large intercalated clusters hinders the fullerene rotational disorder and therefore C_{60} molecules are blocked [59, 64]), it is expected the hyperfine coupling to be anisotropic. For this reason the fit to function 3.4 allows just an estimation of the average hyperfine field as for this experiment (on powder samples) a more precise measurement of the coupling parameters is not allowed. From the mean square analysis, it was found that for Li_6C_{60} the radical hyperfine frequency rises from a value of 123(19) MHz in pristine sample to a value of 550(30) MHz in hydrogenated sample, while for $Na_{10}C_{60}$ it rises from 158(22) MHz to 325(27) MHz in the hydrogenated sample. Incidentally the value of the muonium substituted free radical in pure C_{60} is 325 MHz [140] but, due to different nature of $Na_{10}C_{60}H_y$ and C_{60}, this fact is attributed to coincidence rather than the formation of the same radical. A more precise investigation of the anisotropy of these radicals will be the topic of a next experiment. It should also be noted that in pristine Li_6C_{60} and $Na_{10}C_{60}$, the hyperfine coupling was found to be significantly lower than for pure C_{60} (for which it was about 325 MHz for the radical). The hyperfine field on the muon can be interpreted as an average value of the electron density sensed by muon in the radical state. Here, the presence of C_{60}^{n-} anions, in which the t_{1u} molecular orbital is completely filled, allows to efficiently delocalise the further radical electrons, hence decreasing the hyperfine interaction. On the contrary, as seen in paragraph 3.5, hydrogenation has the effect of deeply change the geometry of the molecule and therefore also of the electronic arrangement. The resulting reduction of point symmetry thus induces the localization of paramagnetic electrons, thereby preventing an efficient delocalization of the radical's electron. The final effect is a decrease in the average distance of the

radical's electron from μ^+ and therefore a relative increase of the hyperfine coupling.

The complex scenario depicted by the µSR experiment is helpful to better understand the hydrogenation process in alkali intercalated fullerides. In such systems, sizable hydrogen storage with reversible character is reached through the hydrogenation of C_{60}^{n-} molecule at much milder conditions as compared with those necessary to achieve the $C_{60}H_y$ hydrofullerite, as discussed in the previous paragraphs. This can be explained as due to the catalytic effect of intercalated alkali clusters, effective in dissociating the hydrogen molecule and to the subsequent migration of hydrogen atoms from the metallic clusters to the buckyball [122]. The slowly decaying component shown in Fig. 3.23 is attributed to a diamagnetic muon fraction (P_D in eq. 3.4) and is realistically originated to the dipolar interaction that muons experience passing near the Li or Na nuclear momenta. In the hydrogenated samples the presence of hydrogen nuclei (protons) would has the effect of increasing these dipolar interactions raising the decay rate. This is clearly observed in lithium compounds while the opposite behavior happens in sodium samples probably as a consequence of different dynamical regime. For Li_6C_{60} the zero field asymmetry was fitted with a simple Lorentzian decay. Muons, diffusing interstitially through the clusters, undergoes a random dynamic interaction with the local nuclear fields. The fitted Lorentzian (or stretched exponential) depolarization functions, which are shown for pristine Li_6C_{60}, originate from this diffusion and can be expressed by the following equation:

$$A(t) = P_D exp(-\lambda t).$$

In the case of $Na_{10}C_{60}$, dynamics is frozen and the asymmetry follows a Gaussian relaxation, indicative of random static interactions with Na nuclei:

$$A(t) = \frac{P_D}{\sqrt{2\pi\sigma^2}} exp(-t^2\sigma^2/2).$$

For hydrogenated samples the behavior is complicated by two main factors:

- presence of hydrogens (protons) bound to C_{60}

➢ and the presence of a small fraction of LiH or NaH.

Whilst the Gaussian and Lorentzian field distributions adequately describe the concentrated and dilute dipole moment limits respectively for Li_6C_{60} and $Na_{10}C_{60}$, in the case of $Li_6C_{60}H_y$ the distinction between the two limits is rather arbitrary and is generalized by using a stretched exponential decay:

$$A(t) = P_D exp\left(-(\lambda t)^{\beta}\right).$$

A simple Lorentzian decay was adopted in order to fit the $Na_{10}C_{60}H_y$ asymmetry. The different fitted decay rates and their temperature dependence

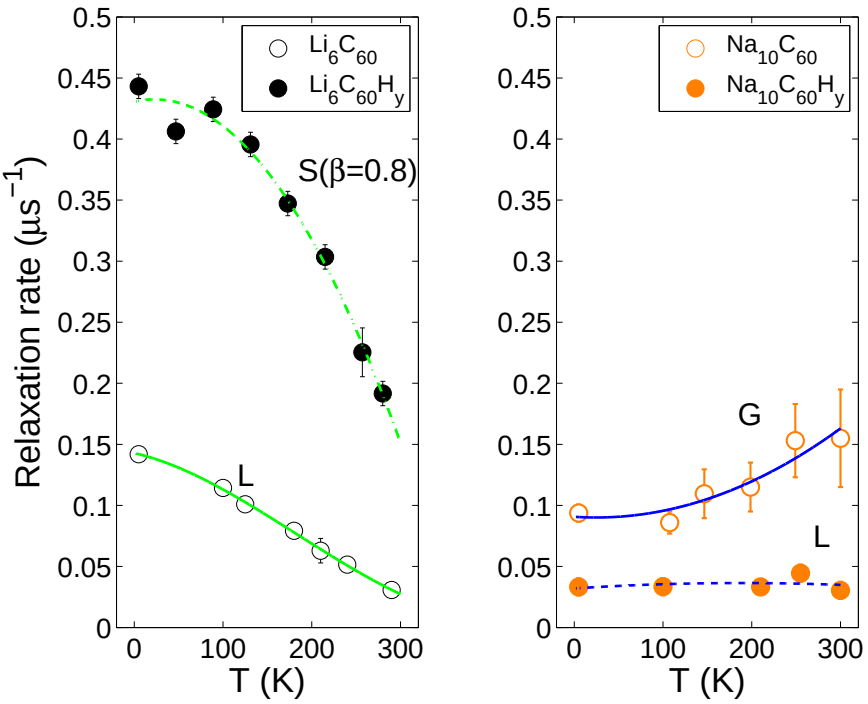

Figure 3.25: Temperature evolution of relaxation rates for pristine and hydrogenated Li_6C_{60} (left) and $Na_{10}C_{60}$ (right). Capital letters are reminder of relaxation functions used in the fit of the ZF experiments: i.e. Gaussian (G), Lorentzian (L) or stretched exponential (S). Solid/dashed lines are guides to the eye.

(see Fig. 3.25) are indicative of various diffusing regimes. For pristine

fullerides it is observed that relaxation decrease raising the temperature for Li_6C_{60} while the opposite happens for $Na_{10}C_{60}$. For $Li_6C_{60}H_y$ the behavior is similar than for the pristine sample (but faster). In the case of $Na_{10}C_{60}H_y$ the relaxation appears constant in the range of 5 to 300 K. It is difficult to assign this diamagnetic fraction to bare muons or to Mu^-, whose formation is commonly observed in alkali metals hydrides [141], however it was demonstrated that relaxation rate for Mu^- follows a thermally activated behavior in LiH and undergoes a decrease in NaH. Nonetheless, the hydrogenated Li_6C_{60} and $Na_{10}C_{60}$ (which certainly contain at least small fraction of hydride) show a different thermal behavior: the relaxation rate of $Li_6C_{60}H_y$ is not activated (as it should be for LiH) while for $Na_{10}C_{60}H_y$ is constant (whereas it should be decreasing in temperature). Moreover, the repolarized fraction of a Mu^- in the LF experiment should presents a hyperfine field around 1 kG (it is 1084 G for NaH [141]) while here it is well below 1 kG. Therefore, the presence of LiH and NaH in the hydrogenated samples is considered negligible in this experiment. However, nothing is known about a Mu^- interstitial to a cluster of few atoms of Li or Na, like it could happen in this samples. Other decay mechanisms like spin exchange (between the electron residing on μ^+ and another paramagnetic electron of the sample) can be ruled out in these systems where no paramagnetic centers are present.

The presence of muon adduct radicals in intercalated fullerides is itself remarkable as it proves that their absence in other known fullerides is probably due to the lack of interstitial Mu (although present endohedrally), and not to the instability of radicals in charged C_{60}, as previously thought [136]. Unlike the most common alkali intercalated fullerides, in these systems the interaction of partly ionized alkali metal clusters [55, 64] is probably at the origin of the observed peculiar behavior. Raman spectra of $Na_{10}C_{60}$ and Li_6C_{60} (shown in Fig. 3.4), proved the charged state of C_{60}^{n-} to be of about $n = 6$ electrons. The even number of electrons on the t_{1u} levels of C_{60} is also confirmed by the non paramagnetic character of $Na_{10}C_{60}$ and Li_6C_{60} as measured by means of SQuID magnetometry. It's easy to understand that, if "only" 6 electrons occupies the LUMO orbitals of C_{60}, at least for $Na_{10}C_{60}$, the remaining electrons have to be delocalized over the cluster

of sodium atoms. Therefore, the clusters are only partially ionized and can bring a residual charge. This fact is also confirmed by the distances between the sodium atoms of cluster in $Na_{10}C_{60}$ which are in an intermediate range between the ionized state and the metallic bond [64, 59]. When muons are implanted in the sample they can interact with the charge of the delocalized electrons residing on the clusters which can be captured leading to the formation of muonium. Surprisingly, differently to what observed in pure

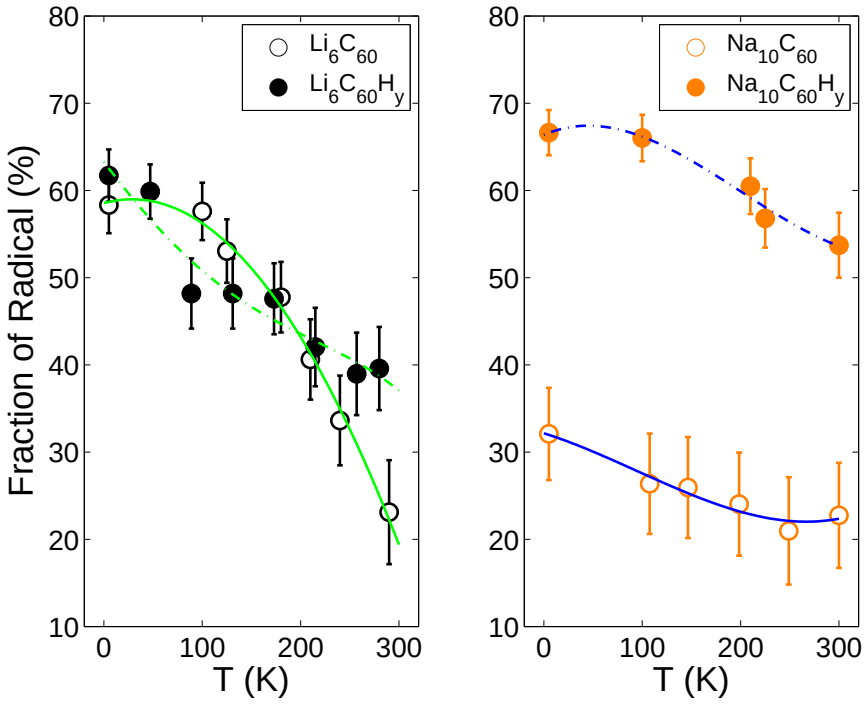

Figure 3.26: Temperature dependence of the fraction of muons producing a radical obtained as difference between full asymmetry and fitted zero field initial asymmetries (A_{rad} in equation 3.4) for pristine and hydrogenated Li_6C_{60} (left) and $Na_{10}C_{60}$ (right); solid lines are a guide to the eye.

C_{60} [134], the fraction of radicals here depends on temperature. Fig. 3.26 shows the temperature dependence of the observed missing fractions which were found to invariably increase on cooling for all the investigated samples. Such a behavior indicates that the propensity of C_{60} to bind atomic hydro-

gen and, therefore, to form hydrofullerite, is enhanced at cryogenic temperatures and it is already present also at room temperature. This suggests that also hydrogen absorption is expected to be enhanced at low T, as long as atomic H is available. Nevertheless, the hydrogen absorption experiments show that only at moderate temperature the hydrogenation occur, due to the required homolytic bond rupture of H_2, while the formation of $C_{60}H_y$ would be promoted at low temperature. The more convincing hypothesis is that at high temperature the dissociation of the H_2 molecule is mediated by the intercalated alkali clusters. The partial electronic charge present on the cluster may promote the dissociation of the hydrogen molecule. Moreover, it is likely that even the high charged state of Na_xC_{60} and Li_xC_{60} ($x \geq 6$) contributes to the overall process. In fact, the high degree of charge present on the antibonding orbitals of C_{60} would greatly increase the probability to attract a hydrogen atom on the molecule, significantly lowering the energy barrier required to form the $C-H$ bond. With this perspective, the μSR experiment results suggest that, in order to increase the storage capabilities of these materials, the assisted dissociation of the H_2 molecule must be improved. A possible way to achieve this result is the addition of transition metals, such as Ni, Pd or Pt, which are known to efficiently catalyze the H_2 dissociation at low temperature [142]. However, as discussed above and experimentally proved [143], the simple intercalation of transition metals would not be sufficient to reach the high uptake rates observed in $Na_{10}C_{60}$ and Li_6C_{60}, as the charged state of C_{60}, not achieved in transition metals intercalated fullerides, appears also to play an important role in inducing the observed high degree of hydrogenation.

It is also evident, that the fraction of adduct radicals appear larger in hydrogenated samples than in the pristine ones, as shown in Table 3.5. This happens in all the explored thermal range for pristine and hydrogenated $Na_{10}C_{60}$ while it is evident only near room temperature for the Li_6C_{60}. For understanding this result, one has to consider the fact that, after the hydrogenation, $C_{60}H_y$ molecule exhibits a more pronounced curvature than C_{60}. This was clearly demonstrated in paragraph 3.5 where the PDF of $Li_6C_{60}H_y$ and $Na_{10}C_{60}H_y$ were attributed to the T_h and T isomers of $C_{60}H_{36}$. In par-

	f_R at 5 K (%)	f_R at 300 K (%)	B_{hyp} (mT)	ν_{hyp}(MHz)
Li_6C_{60}	58(3)	23(6)	4.4	123(19)
$Li_6C_{60}H_y$	61(3)	39(5)	20.3	550(30)
$Na_{10}C_{60}$	32(5)	22(6)	5.7	158(22)
$Na_{10}C_{60}H_y$	66(4)	54(3)	11.6	325(27)

Table 3.5: Radical fraction percentage (f_R) relative to full asymmetry and fitted hyperfine fields in pristine and hydrogenated samples of Li_6C_{60} and $Na_{10}C_{60}$.

ticular, whereas carbons were almost completely sp^2 hybridized in Li_6C_{60} and $Na_{10}C_{60}$, after hydrogenation the hybridization turns into sp^3 for those carbons which have bound a hydrogen [95]. It is well known that the presence of local curvature in carbon based nanostructures has promoting effects on the H_2 binding energy and that H bond is shown to increase on sp^2 receptors [79], like graphene, by increasing the H coverage [144]. In this case the curvature of the partially hydrogenated fullerene cage is clearly greater than in bare C_{60}, due to the presence of sp^3 hybridized carbon atoms. Especially for $Na_{10}C_{60}H_y$, the T symmetry, found by means of PDF analysis (see Fig. 3.22), leaves four benzene rings available to be subsequently hydrogenated. This is in agreement with the greater increase in the radical fraction produced after hydrogenation of $Na_{10}C_{60}$, with respect to $Li_6C_{60}H_y$ which displays lower increase of radical fraction formed after its hydrogenation.

The hyperfine field on the muon can be interpreted as an average value of the electron density sensed by muon in the radical state. Although the extracted values were obtained with strong assumptions, they could still be interpreted on the basis of the following considerations. In pristine Li_6C_{60} and $Na_{10}C_{60}$, the hyperfine coupling was found to be significantly lower than in pure C_{60}. Here, the presence of C_{60}^{n-} anions, in which the t_{1u} molecular orbital is almost completely filled, allows to efficiently delocalise the further radical electrons, and hence to decrease the hyperfine interaction. As a matter of fact, it is known that light alkali metals intercalated in fullerenes only partially donate their charge to C_{60} [145]. On the other hand, after

the hydrogenation, the conversion to sp^3 of part of carbon atoms on the fullerene cage deeply affects the electronic arrangement of the molecule; this induces the localization of the paramagnetic electrons, thus also increasing the muon hyperfine coupling.

In order to endorse the hypothesis of the cluster's catalytic effect on cluster intercalated compounds a hydrogen absorption experiment was carried on the *bcc*-K_6C_{60}. In this compound the charge transfer on the t_{1u} molecular orbitals is complete [146] (as in the case for $Na_{10}C_{60}$, Li_6C_{60} and $Li_{12}C_{60}$) and the *bcc* structure avoids the formation of K^+ clusters. The sorption measurements on K_6C_{60} were made under the same conditions of Li_6C_{60}, but the amount of hydrogen absorbed/desorbed was too low to be detected. As previously discussed, in this system the formation of radicals in the µSR experiment is suppressed and this fact was tentatively explained as due to the charged state of C_{60} [47]. In the case of Li_6C_{60} the Raman spectrum evidenced a complete charge transfer of 6 electrons on the t_{1u} molecular orbitals. Under this point of view the K_6C_{60} and Li_6C_{60} can cautiously be compared (both are not electronic conductors and presents a C_{60}^{6-} anion). In such a systems the most prominent difference is the presence (or not) of an alkali intercalated cluster. The explanation given by the µSR experiment is effective if the clusters in $Na_{10}C_{60}$ and Li_6C_{60} hold some residual electronic charge on their orbitals (this is true for $Na_{10}C_{60}$ but apparently not for Li_6C_{60}, where all the lithium atoms seem to be ionized). The muonium is formed during the deceleration of μ^+. In this process muons cover long distances before thermalise and can easily undergo scattering events with electrons. In K_6C_{60}, for example, the formation of Mu occurs outside the fullerene molecule but if the energy is enough the pseudo hydrogen atom can break a carbon bond thus entering in the endohedral cavity (the broken carbon bonds can be easily reconstructed). This leads to a very small fraction of $Mu@C_{60}$. In Li_6C_{60} the endohedral muonium is not formed but a big fraction of radical is present. The high disorder of this phase, as confirmed by powder diffraction analysis, may be the main cause of the formation of Mu (as it is well known, the µSR is very sensitive to the presence of defects [147, 115]). In particular there can be two main source of disorder:

merohedral, as present in the high temperature phase of Li_4C_{60} [50], and the disorder due to a distribution of cluster's configurations.[1] In particular, the latter could be the responsible of scattering efficient in producing Mu, if one of the most frequent defects was a cluster in which part of the charge is maintained.

[1] as in the case of Na_6C_{60} [59] the symmetry of the cell allows different configurations of the same cluster. Moreover, if the occupancy of the alkaline atoms is not the same in all the cells, a distribution of the number of atoms constituting the clusters may be possible.

Chapter 4

Conclusions

In the present work, the lithium and sodium-cluster intercalated fullerides were synthesized and their structural, electronic and absorbing properties were investigated by means of *ex-situ* synchrotron diffraction, *in-situ* neutron diffraction, Raman spectroscopy, pressure-composition isotherms (pcT), analysis of the X-ray pair distribution function (PDF) and muon spin relaxation (μSR).

The interest in these materials was motivated by both theoretical [83, 75] and experimental works [100] who evidenced an increased interaction of these systems with hydrogen. A Kubas-like or electrostatic interaction was hypothesized in some theoretical works whereas a chemisorption of hydrogen onto C_{60}, forming hydrofullerene, was experimentally detected. Up to now, a clear mechanism of hydrogenation was not demonstrated for Na_xC_{60} and Li_xC_{60} absorbing systems.

The structural analysis of the pristine phases of Li_6C_{60}, $Li_{12}C_{60}$ and $Na_{10}C_{60}$ highlighted the presence of alkali intercalated clusters inside the lattice of C_{60} anions. While in $Na_{10}C_{60}$ the cluster (made of nine sodium atoms) resides in the octahedral voids of the C_{60} *fcc* structure, in the case of $Li_{12}C_{60}$ the rearrangement of C_{60} anions allows a cluster of 5 lithium atoms to be held within the pseudo tetrahedral voids of a $P2_1/n$ cell. The Li_6C_{60} appears characterized by intrinsic merohedral disorder and a fcc arrangement of C_{60} anions (similarly to pristine C_{60}) was hypothesized, allowing

a cluster of Li atoms to stay in the T_h or O_h voids. The detection of a maximum charge of 6 electrons, by means of Raman spectroscopy, on the fullerene anions of Li_6C_{60}, $Li_{12}C_{60}$ and $Na_{10}C_{60}$ leads to hypothesize the presence of electrons onto alkali clusters, compensating the residual charge.

The absorbing properties of these compounds were demonstrated to be remarkable if compared to pure fullerene, but also compared with commonly studied metal hydrides and complex metal hydrides. $Na_{10}C_{60}$ was able to store up to 3.5 mass% H_2 in a completely reversible process. Li_6C_{60} and $Li_{12}C_{60}$ were demonstrated to be able to absorb up to 5 mass% H_2, in optimized conditions, and the process is reversible. For both sodium and lithium fullerides hydrogenation involves the segregation of metal hydride minor fraction and the formation of a stable alkali intercalated hydrofulleride.

The investigation of hydrogenated compounds of sodium and lithium fullerides by means of total scattering technique allowed to detect the geometry of the hydrofullerene molecules and to hypothesize a possible structure of the alkali intercalated hydrofullerides.

Finally, the µSR experiment on pristine and hydrogenated Li_6C_{60} and $Na_{10}C_{60}$ highlighted an unusual tendency towards the formations of radicals on the C_{60} anions, not observed in A_xC_{60} parent compounds ($A = K$, Rb, Cs). Moreover, the radical fraction was demonstrated to increase by lowering the temperature and the hydrogenated compounds proved to be more reactive toward subsequent hydrogenation. A mechanism of hydrogenation was hypothesized, involving the presence of electrons localized far from the fullerene anions and possibly residing on the alkali clusters.

This research opens many outlooks towards the discovery of new hydrogen storage systems based on intercalated fullerene nanostructures that have demonstrated to be, once again, source of great interest thanks to their surprising properties.

Chapter 5

References

Bibliography

[1] A. Züttel, A. Borgschulte, and L. Schlapbach, *Hydrogen as a future energy carrier*, WILEY-VCH, Ed. WILEY-VCH, 2011. [Online]. Available: http://books.google.com/books?hl=en&lr=&id=t2RieE4Vz9AC&oi=fnd&pg=PR5&dq=Hydrogen+as+a+Future+Energy+Carrier&ots=grR8Xx2Pgg&sig=pOn7dEUhB-KQZ-iyI9ffRmoZFTc 3

[2] U.S. Department of Energy (DOE), "Hydrogen and Fuel Cells Program Plan," *internet version: [http://www.hydrogen.energy.gov/pdfs/program_plan2011.pdf]*, 2011. [Online]. Available: http://www.hydrogen.energy.gov/roadmaps_vision.html 4

[3] L. Schlapbach and A. Züttel, "Hydrogen-storage materials for mobile applications." *Nature*, vol. 414, no. 6861, pp. 353–8, Nov. 2001. [Online]. Available: http://www.ncbi.nlm.nih.gov/pubmed/11713542 5, 17

[4] I. Jain, P. Jain, and A. Jain, "Novel hydrogen storage materials: A review of lightweight complex hydrides," *Journal of Alloys and Compounds*, vol. 503, no. 2, pp. 303–339, Aug. 2010. [Online]. Available: http://linkinghub.elsevier.com/retrieve/pii/S0925838810011436 5

[5] B. Bogdanović, R. A. Brand, A. Marjanović, M. Schwickardi, and J. Tölle, "Metal-doped sodium aluminium hydrides as potential new hydrogen storage materials," *Journal of Alloys and Compounds*,

vol. 302, no. 1-2, pp. 36–58, Apr. 2000. [Online]. Available: http://linkinghub.elsevier.com/retrieve/pii/S0925838899006635 5

[6] J. Wang, A. D. Ebner, and J. a. Ritter, "Physiochemical pathway for cyclic dehydrogenation and rehydrogenation of LiAlH4." *Journal of the American Chemical Society*, vol. 128, no. 17, pp. 5949–54, May 2006. [Online]. Available: http://www.ncbi.nlm.nih.gov/pubmed/16637663 5

[7] M. Fichtner, O. Fuhr, and O. Kircher, "Magnesium alanate - a material for reversible hydrogen storage?" *Journal of Alloys and Compounds*, vol. 356-357, pp. 418–422, Aug. 2003. [Online]. Available: http://linkinghub.elsevier.com/retrieve/pii/S0925838802012367 5

[8] J. J. Vajo, S. L. Skeith, and F. Mertens, "Reversible storage of hydrogen in destabilized LiBH4." *The journal of physical chemistry. B*, vol. 109, no. 9, pp. 3719–22, Mar. 2005. [Online]. Available: http://www.ncbi.nlm.nih.gov/pubmed/16851415 5

[9] K. L. Lim, H. Kazemian, Z. Yaakob, and W. R. W. Daud, "Solid-state Materials and Methods for Hydrogen Storage: A Critical Review," *Chemical Engineering & Technology*, vol. 33, no. 2, pp. 213–226, Feb. 2010. [Online]. Available: http://doi.wiley.com/10.1002/ceat.200900376 6

[10] R. Ströbel, J. Garche, P. Moseley, L. Jörissen, and G. Wolf, "Hydrogen storage by carbon materials," *Journal of Power Sources*, vol. 159, no. 2, pp. 781–801, Sep. 2006. [Online]. Available: http://linkinghub.elsevier.com/retrieve/pii/S0378775306005829 6

[11] C. Otero Areán, D. Nachtigallová, P. Nachtigall, E. Garrone, and M. Rodríguez Delgado, "Thermodynamics of reversible gas adsorption on alkali-metal exchanged zeolites–the interplay of infrared spectroscopy and theoretical calculations." *Physical chemistry chemical physics : PCCP*, vol. 9, no. 12, pp. 1421–37, Mar. 2007.

[Online]. Available: http://www.ncbi.nlm.nih.gov/pubmed/17356750 6

[12] Y. Sun, L. Wang, W. a. Amer, H. Yu, J. Ji, L. Huang, J. Shan, and R. Tong, "Hydrogen Storage in Metal-Organic Frameworks," *Journal of Inorganic and Organometallic Polymers and Materials*, vol. 23, no. 2, pp. 270–285, Oct. 2012. [Online]. Available: http://link.springer.com/10.1007/s10904-012-9779-4 6

[13] G. J. Kubas, R. R. Ryan, B. I. Swanson, P. J. Vergamini, and H. J. Wasserman, "Characterization of the first examples of isolable molecular hydrogen complexes, M(CO)3(PR3)2(H2) (M = molybdenum or tungsten; R = Cy or isopropyl). Evidence for a side-on bonded dihydrogen ligand," *Journal of the American Chemical Society*, vol. 106, no. 2, pp. 451–452, Jan. 1984. [Online]. Available: http://pubs.acs.org/doi/abs/10.1021/ja00314a049 7

[14] D. M. Heinekey and W. J. Oldham, "Coordination chemistry of dihydrogen," *Chemical Reviews*, vol. 93, no. 3, pp. 913–926, May 1993. [Online]. Available: http://pubs.acs.org/doi/abs/10.1021/cr00019a004 8

[15] G. J. Kubas, "Metal-dihydrogen and σ-bond coordination: the consummate extension of the Dewar-Chatt-Duncanson model for metal-olefin π bonding," *Journal of Organometallic Chemistry*, vol. 635, no. 1-2, pp. 37–68, Oct. 2001. [Online]. Available: http://linkinghub.elsevier.com/retrieve/pii/S0022328X0101066X 8

[16] S. Khoobiar, "Particle to Particle Migration of Hydrogen Atoms on Platinum-Alumina Catalysts from Particle to Neighboring Particles," *The Journal of Physical Chemistry*, vol. 68, no. 2, pp. 411–412, Feb. 1964. [Online]. Available: http://pubs.acs.org/doi/abs/10.1021/j100784a503 8

[17] A. Singh, M. Ribas, and B. Yakobson, "H-spillover through the catalyst saturation: An ab initio thermodynamics study,"

Acs Nano, vol. 3, no. 7, pp. 1657–62, Jul. 2009. [Online]. Available: http://www.ncbi.nlm.nih.gov/pubmed/19534542http://pubs.acs.org/doi/abs/10.1021/nn9004044 9, 10

[18] P. A. Sermon and G. C. Bond, "Hydrogen Spillover," *Catalysis Reviews*, vol. 8, no. 1, pp. 211–239, Jan. 1974. [Online]. Available: http://www.tandfonline.com/doi/abs/10.1080/01614947408071861 10

[19] H. L. Gruber, "CHEMISORPTION STUDIES ON SUPPORTED PLATINUM," *The Journal of Physical Chemistry*, vol. 66, no. 1, pp. 48–54, Jan. 1962. [Online]. Available: http://pubs.acs.org/doi/abs/10.1021/j100807a010 10

[20] Boudart, M, A. W. Aldag, and M. A. Vannice, "On the slow uptake of hydrogen by platinized carbon," *Journal of Catalysis*, vol. 18, no. 1, pp. 46–51, Jul. 1970. [Online]. Available: http://linkinghub.elsevier.com/retrieve/pii/0021951770903106 10

[21] H. W. Kroto, J. R. Heath, S. C. O'Brien, R. F. Curl, and R. E. Smalley, "C60: Buckminsterfullerene," *Nature*, vol. 318, no. 6042, pp. 162–163, Nov. 1985. [Online]. Available: http://www.nature.com/doifinder/10.1038/318162a0 11

[22] W. Krätschmer, L. D. Lamb, K. Fostiropoulos, and D. R. Huffman, "Solid C60: a new form of carbon," *Nature*, vol. 347, no. 6291, pp. 354–358, Sep. 1990. [Online]. Available: http://www.nature.com/doifinder/10.1038/347354a0 12

[23] P. Heiney, J. Fischer, A. McGhie, W. Romanow, A. Denenstein, J. McCauley Jr., A. Smith, and D. Cox, "Orientational ordering transition in solid C_{60}," *Physical Review Letters*, vol. 66, no. 22, pp. 2911–2914, Jun. 1991. [Online]. Available: http://link.aps.org/doi/10.1103/PhysRevLett.66.2911 12, 15, 45

[24] H.-B. Bürgi, R. Restori, and D. Schwarzenbach, "Structure of C 60 : partial orientational order in the room-temperature

modification of C 60," *Acta Crystallographica Section B Structural Science*, vol. 49, no. 5, pp. 832–838, Oct. 1993. [Online]. Available: http://scripts.iucr.org/cgi-bin/paper?S0108768193004008 12

[25] L. Forró and L. Mihály, "Electronic properties of doped fullerenes," *Reports on Progress in Physics*, vol. 64, no. 5, pp. 649–699, May 2001. [Online]. Available: http://stacks.iop.org/0034-4885/64/i=5/a=202?key=crossref.58b092eeffcfe4f7a0049937cd832ce0 12, 16

[26] L. Degiorgi, "Fullerenes and carbon derivatives: From insulators to superconductors," *Advances in Physics*, vol. 47, no. 2, pp. 207–316, Mar. 1998. [Online]. Available: http://www.tandfonline.com/doi/abs/10.1080/000187398243555 13

[27] S. Saito and A. Oshiyama, "Cohesive mechanism and energy bands of solid C_{60}," *Physical Review Letters*, vol. 66, no. 20, pp. 2637–2640, May 1991. [Online]. Available: http://link.aps.org/doi/10.1103/PhysRevLett.66.2637 13

[28] D. Dubois, K. M. Kadish, S. Flanagan, R. E. Haufler, L. P. F. Chibante, and L. J. Wilson, "Spectroelectrochemical study of the C60 and C70 fullerenes and their mono-, di-, tri- and tetraanions," *Journal of the American Chemical Society*, vol. 113, no. 11, pp. 4364–4366, May 1991. [Online]. Available: http://pubs.acs.org/doi/abs/10.1021/ja00011a069 13

[29] C. Bruno, I. Doubitski, M. Marcaccio, F. Paolucci, D. Paolucci, and A. Zaopo, "Electrochemical generation of c 60 2+ and c 60 3+." *Journal of the American Chemical Society*, vol. 125, no. 51, pp. 15 738–9, Dec. 2003. [Online]. Available: http://pubs.acs.org/doi/pdf/10.1021/ja0388515http://www.ncbi.nlm.nih.gov/pubmed/14677952 13

[30] C. Bruno, M. Marcaccio, D. Paolucci, C. Castellarin-Cudia, A. Goldoni, A. V. Streletskii, T. Drewello, S. Barison, A. Venturini, F. Zerbetto, and F. Paolucci, "Growth of p- and n-dopable films from electrochemically generated C60 cations." *Journal of the American*

Chemical Society, vol. 130, no. 12, pp. 3788–96, Mar. 2008. [Online]. Available: http://www.ncbi.nlm.nih.gov/pubmed/18314972 13

[31] J. Cowley, M.-Q. Liu, B. Ramakrishna, T. Peace, A. Wertsching, and M. Pena, "A new type of metal-fulleride structure: C60Pd3," *Carbon*, vol. 32, no. 4, pp. 746–748, Jan. 1994. [Online]. Available: http://linkinghub.elsevier.com/retrieve/pii/0008622394900981 14

[32] M. H. Herbst, N. M. Pinhal, F. A. Demétrio, G. H. Dias, and N. V. Vugman, "Solid-state structural studies on amorphous platinum-fullerene[60] compounds [PtnC60]," *Journal of Non-Crystalline Solids*, vol. 272, no. 2-3, pp. 127–130, Aug. 2000. [Online]. Available: http://linkinghub.elsevier.com/retrieve/pii/S0022309300002295 14

[33] Y. Lin, R. Cai, Y. Chen, and Z. Huang, "Synthesis of transition-metal based nonlinear optical organometallic fullerene derivatives C60M2 (M= Pd, Pt)," *Journal of materials ...*, vol. 18, pp. 1383–1385, 1999. [Online]. Available: http://www.springerlink.com/index/T6881J7587025886.pdf 14

[34] L. Norin, U. Jansson, C. Dyer, P. Jacobsson, and S. McGinnis, "On the Existence of Transition-Metal Fullerides: Deposition and Characterization of Ti x C 60," *Chemistry of Materials*, vol. 10, no. 4, pp. 1184–1190, Apr. 1998. [Online]. Available: http://pubs.acs.org/doi/abs/10.1021/cm9707871 14

[35] D. K. Patel, D. M. Thompson, M. C. Baird, L. K. Thompson, and K. F. Preston, "Fulleride compounds of the transition metals: NaCoC60 - 3THF," *Journal of Organometallic Chemistry*, vol. 545-546, no. J 997, pp. 607–610, Jan. 1997. [Online]. Available: http://linkinghub.elsevier.com/retrieve/pii/S0022328X97004014 14

[36] a.V. Talyzin and U. Jansson, "A comparative Raman study of some transition metal fullerides," *Thin Solid Films*, vol. 429, no. 1-2, pp. 96–101, Apr. 2003. [Online]. Available: http://linkinghub.elsevier.com/retrieve/pii/S0040609003002785 14

[37] V. Venegas and J. Ortiz-Lopez, "Synthesis and characterization of Hg metal-doped C 60," *Chemical Physics ...*, no. March, pp. 655–661, 2000. [Online]. Available: http://www.sciencedirect.com/science/article/pii/S0009261400000737 14

[38] J. Arvanitidis, K. Papagelis, S. Margadonna, K. Prassides, and A. N. Fitch, "Temperature-induced valence transition and associated lattice collapse in samarium fulleride." *Nature*, vol. 425, no. 6958, pp. 599–602, Oct. 2003. [Online]. Available: http://www.ncbi.nlm.nih.gov/pubmed/14534581 14

[39] A. S. Ginwalla, A. L. Balch, S. M. Kauzlarich, S. H. Irons, P. Klavins, and R. N. Shelton, "Synthesis and Characterization of the Europium Fullerides Eu x C 60 (x = 1-6)," *Chemistry of Materials*, vol. 9, no. 1, pp. 278–284, Jan. 1997. [Online]. Available: http://pubs.acs.org/doi/abs/10.1021/cm960358n 14

[40] I. Margiolaki, S. Margadonna, K. Prassides, T. Hansen, K. Ishii, and H. Suematsu, "Magnetic Structure of the Europium Fulleride Ferromagnet Eu 6 C 60," *Journal of the American Chemical Society*, vol. 124, no. 38, pp. 11 288–11 289, Sep. 2002. [Online]. Available: http://www.ncbi.nlm.nih.gov/pubmed/12236741http://pubs.acs.org/doi/abs/10.1021/ja0274148 14

[41] M. J. Rosseinsky, "Fullerene intercalation chemistry," *Journal of Materials Chemistry*, vol. 5, no. 10, p. 1497, 1995. [Online]. Available: http://xlink.rsc.org/?DOI=jm9950501497 15

[42] J. Fox, G. Lopinski, J. Lannin, G. Adams, J. Page, and J. Fischer, "Neutron diffraction and structural models of RbC60 phases," *Chemical Physics Letters*, vol. 249, no. 3-4, pp. 195–200, Feb. 1996. [Online]. Available: http://linkinghub.elsevier.com/retrieve/pii/0009261495013776 15

[43] O. Chauvet, G. Oszlànyi, L. Forro, P. Stephens, M. Tegze, G. Faigel, and A. Jànossy, "Quasi-one-dimensional electronic

structure in orthorhombic RbC60," *Physical Review Letters*, vol. 72, no. 17, pp. 2721–2724, Apr. 1994. [Online]. Available: http://link.aps.org/doi/10.1103/PhysRevLett.72.2721 15

[44] P. Stephens, L. Mihaly, J. Wiley, S.-m. Huang, R. Kaner, F. Diederich, R. Whetten, and K. Holczer, "Structure of Rb:C60 compounds," *Physical Review B*, vol. 45, no. 1, pp. 543–546, Jan. 1992. [Online]. Available: http://link.aps.org/doi/10.1103/PhysRevB.45.543 15

[45] S. Pekker, L. Forró, L. Mihály, and A. Jánossy, "Orthorhombic A1C60: A conducting linear alkali fulleride polymer?" *Solid State Communications*, vol. 90, no. 6, pp. 349–352, May 1994. [Online]. Available: http://linkinghub.elsevier.com/retrieve/pii/003810989490796X 15

[46] S. C. Erwin and W. E. Pickett, "Theoretical Fermi-Surface Properties and Superconducting Parameters for K3C60." *Science (New York, N.Y.)*, vol. 254, no. 5033, pp. 842–5, Nov. 1991. [Online]. Available: http://www.ncbi.nlm.nih.gov/pubmed/17787174 15

[47] R. Kiefl, T. Duty, J. Schneider, A. MacFarlane, K. Chow, J. Elzey, P. Mendels, G. Morris, J. Brewer, E. Ansaldo, C. Niedermayer, D. Noakes, C. Stronach, B. Hitti, and J. Fischer, "Evidence for endohedral muonium in K_{x} C_{60} and consequences for electronic structure," *Physical Review Letters*, vol. 69, no. 13, pp. 2005–2008, Sep. 1992. [Online]. Available: http://link.aps.org/doi/10.1103/PhysRevLett.69.2005 14, 15, 85, 88, 97

[48] A. Maxwell, P. Brühwiler, S. Andersson, N. Må rtensson, and P. Rudolf, "Electronic structure study of KxC60 compounds with x $>$ 6," *Chemical Physics Letters*, vol. 247, no. 3, pp. 257–263, Dec. 1995. [Online]. Available: http://linkinghub.elsevier.com/retrieve/pii/0009261495012061 15, 49

[49] P. Strasser and M. Ata, "Electrochemical Synthesis of Polymerized LiC 60 Films," *The Journal of Physical Chemistry B*, vol. 102, no. 21, pp. 4131–4134, May 1998. [Online]. Available: http://pubs.acs.org/doi/abs/10.1021/jp980431s 15

[50] M. Riccò, M. Belli, D. Pontiroli, M. Mazzani, T. Shiroka, D. Arčon, a. Zorko, S. Margadonna, and G. Ruani, "Recovering metallicity in A4C60: The case of monomeric Li4C60," *Physical Review B*, vol. 75, no. 8, p. 081401, Feb. 2007. [Online]. Available: http://link.aps.org/doi/10.1103/PhysRevB.75.081401 15, 46, 63, 98

[51] M. Riccò, M. Belli, M. Mazzani, D. Pontiroli, D. Quintavalle, a. Jánossy, and G. Csányi, "Superionic Conductivity in the Li4C60 Fulleride Polymer," *Physical Review Letters*, vol. 102, no. 14, p. 145901, Apr. 2009. [Online]. Available: http://link.aps.org/doi/10.1103/PhysRevLett.102.145901 14, 15, 16, 46

[52] S. Margadonna, D. Pontiroli, M. Belli, T. Shiroka, M. Ricco, and M. Brunelli, "Li4C60: a polymeric fulleride with a two-dimensional architecture and mixed interfullerene bonding motifs." *Journal of the American Chemical Society*, vol. 126, no. 46, pp. 15 032–3, Nov. 2004. [Online]. Available: http://www.ncbi.nlm.nih.gov/pubmed/15547992 15, 16, 63

[53] T. Shiroka, M. Riccò, F. Barbieri, E. Zannoni, and M. Tomaselli, "Clustering and polymerization of Li15C60," *Physics of the Solid State*, vol. 44, no. 3, pp. 521–524, Mar. 2002. [Online]. Available: http://link.springer.com/10.1134/1.1462693 15, 17

[54] L. Cristofolini, M. Riccò, and R. De Renzi, "NMR and high-resolution x-ray diffraction evidence for an alkali-metal fulleride with large interstitial clusters: Li12C60," *Physical Review B*, vol. 59, no. 13, pp. 8343–8346, Apr. 1999. [Online]. Available: http://link.aps.org/doi/10.1103/PhysRevB.59.8343 15, 21

[55] M. Tomaselli, B. H. Meier, M. Riccò, T. Shiroka, and A. Sartori, "A multiple-quantum nuclear magnetic resonance study of interstitial Li clusters in Li_{x}C_{60}," *The Journal of Chemical Physics*, vol. 115, no. 1, p. 472, 2001. [Online]. Available: http://link.aip.org/link/JCPSA6/v115/i1/p472/s1&Agg=doi 15, 16, 93

[56] M. Tomaselli, B. Meier, M. Riccò, T. Shiroka, and a. Sartori, "NMR evidence for sp3 carbon in the low-temperature phase of LixC60," *Physical Review B*, vol. 63, no. 11, p. 113405, Mar. 2001. [Online]. Available: http://link.aps.org/doi/10.1103/PhysRevB.63.113405 15, 63

[57] Y. Kubozono, Y. Takabayashi, S. Fujiki, S. Kashino, T. Kambe, Y. Iwasa, and S. Emura, "Metal-insulator transition at 50 K in Na2C60," *Physical Review B*, vol. 59, no. 23, pp. 15 062–15 069, Jun. 1999. [Online]. Available: http://link.aps.org/doi/10.1103/PhysRevB.59.15062 15

[58] D. Murphy, M. Rosseinsky, R. Fleming, R. Tycko, A. Ramirez, R. Haddon, T. Siegrist, G. Dabbagh, J. Tully, and R. Walstedt, "Synthesis and characterization of alkali metal fullerides: AxC60," *Journal of Physics and Chemistry of Solids*, vol. 53, no. 11, pp. 1321–1332, Nov. 1992. [Online]. Available: http://linkinghub.elsevier.com/retrieve/pii/002236979290230B 15, 62

[59] M. J. Rosseinsky, D. W. Murphy, R. M. Fleming, R. Tycko, A. P. Ramirez, G. Dabbagh, and S. E. Barrett, "Structural and electronic properties of sodium-intercalated C60," *Nature*, vol. 356, no. 6368, pp. 416–418, Apr. 1992. [Online]. Available: http://www.nature.com/doifinder/10.1038/356416a0 15, 17, 21, 44, 45, 51, 56, 70, 90, 94, 98

[60] G. Oszlányi, G. Baumgartner, G. Faigel, and L. Forró, "Na4C60: An Alkali Intercalated Two-Dimensional Polymer," *Physical Review Letters*, vol. 78, no. 23, pp. 4438–4441, Jun. 1997. [Online]. Available: http://link.aps.org/doi/10.1103/PhysRevLett.78.4438 15, 16, 56

[61] G. Oszlányi, G. Baumgartner, G. Faigel, L. Gránásy, and L. Forró, "Polymer-monomer phase transition in Na4C60," *Physical Review B*, vol. 58, no. 1, pp. 5–7, Jul. 1998. [Online]. Available: http://link.aps.org/doi/10.1103/PhysRevB.58.5 15

[62] Y. Kubozono, Y. Takabayashi, T. Kambe, S. Fujiki, S. Kashino, and S. Emura, "Structure and physical properties of Na4C60 under ambient and high pressures," *Physical Review B*, vol. 63, no. 4, p. 045418, Jan. 2001. [Online]. Available: http://link.aps.org/doi/10.1103/PhysRevB.63.045418 15, 56

[63] M. Kobayashi, N. Kimata, and S. Heguri, "X-ray diffraction and magnetic susceptibility of sodium fullerides NaxC60," *Journal of Physics and Chemistry of Solids*, vol. 71, no. 4, pp. 689–691, Apr. 2010. [Online]. Available: http://linkinghub.elsevier.com/retrieve/pii/S0022369709004107 14, 15, 56

[64] T. Yildirim, O. Zhou, J. E. Fischer, N. Bykovetz, R. A. Strongin, M. A. Cichy, A. B. Smith III, C. L. Lin, and R. Jelinek, "Intercalation of sodium heteroclusters into the C60 lattice," *Nature*, vol. 360, no. 6404, pp. 568–571, Dec. 1992. [Online]. Available: http://www.nature.com/doifinder/10.1038/360568a0 15, 17, 21, 44, 45, 51, 56, 70, 90, 93, 94

[65] Y. Iwasa and T. Takenobu, "Superconductivity, MottÂ Hubbard states, and molecular orbital order in intercalated fullerides," *Journal of Physics: Condensed Matter*, vol. 15, no. 13, pp. R495–R519, Apr. 2003. [Online]. Available: http://stacks.iop.org/0953-8984/15/i=13/a=202?key=crossref.107289821c87ff77467178af37916104 14

[66] D. Pontiroli, M. Aramini, M. Gaboardi, M. Mazzani, A. Gorreri, M. Riccò, I. Margiolaki, and D. Sheptyakov, "Ionic conductivity in the Mg intercalated fullerene polymer Mg2C60," *Carbon*, vol. 51, pp. 143–147, Jan. 2013. [Online]. Available: http://linkinghub.elsevier.com/retrieve/pii/S0008622312006744 14

[67] J. Kohanoff, W. Andreoni, and M. Parrinello, "A possible new highly stable fulleride cluster: Li12C60," *Chemical Physics Letters*, vol. 198, no. 5, pp. 472–477, Oct. 1992. [Online]. Available: http://linkinghub.elsevier.com/retrieve/pii/000926149280030F 16

[68] G. K. Wertheim, D. N. E. Buchanan, and J. E. Rowe, "Charge Donation by Calcium into the t1g Band of C60," *Science*, vol. 258, no. 5088, pp. 1638–1640, 1992. [Online]. Available: http://www.sciencemag.org/content/258/5088/1638.abstract 16

[69] ——, "Electronic structure of barium fullerides," *Chemical Physics Letters*, vol. 206, no. 1-4, pp. 193–196, 1993. [Online]. Available: http://www.sciencedirect.com/science/article/pii/0009261493855405 16

[70] L. Jiang and B. Koel, "Charge transfer from potassium into the t1g band of C60," *Physical Review Letters*, vol. 72, no. 1, pp. 140–143, Jan. 1994. [Online]. Available: http://link.aps.org/doi/10.1103/PhysRevLett.72.140 16

[71] L. Cristofolini, M. Riccò, and R. De Renzi, "NMR and high-resolution x-ray diffraction evidence for an alkali-metal fulleride with large interstitial clusters: Li12C60," *Physical Review B*, vol. 59, no. 13, pp. 8343–8346, Apr. 1999. [Online]. Available: http://link.aps.org/doi/10.1103/PhysRevB.59.8343 17

[72] M. Yasukawa and S. Yamanaka, "Synthesis of LixC60(x=1-28) fullerides under high-pressure and high-temperature conditions and their electrical properties," *Chemical Physics Letters*, vol. 341, no. 5-6, pp. 467–475, Jun. 2001. [Online]. Available: http://linkinghub.elsevier.com/retrieve/pii/S0009261401005449 17

[73] A. Chambers, C. Park, R. T. K. Baker, and N. M. Rodriguez, "Hydrogen Storage in Graphite Nanofibers," *The Journal of Physical Chemistry B*, vol. 102, no. 22, pp. 4253–4256, May 1998. [Online]. Available: http://pubs.acs.org/doi/abs/10.1021/jp980114l 17

[74] M. Gaboardi, A. Bliersbach, G. Bertoni, M. Aramini, G. Vlahopoulou, D. Pontiroli, P. Mauron, G. Magnani, G. Salviati, A. Züttel, and M. Riccò, "Decoration of graphene with nickel nanoparticles: study of the interaction with hydrogen," *Journal of Materials Chemistry A*, vol. 2, no. 4, pp. 1039–1046, 2014. [Online]. Available: http://xlink.rsc.org/?DOI=c3ta14127f 17

[75] Q. Sun, P. Jena, Q. Wang, and M. Marquez, "First-principles study of hydrogen storage on Li12C60." *Journal of the American Chemical Society*, vol. 128, no. 30, pp. 9741–5, Aug. 2006. [Online]. Available: http://www.ncbi.nlm.nih.gov/pubmed/23160931http://www.ncbi.nlm.nih.gov/pubmed/16866529 18, 19, 20, 64, 99

[76] H. Cheng, A. C. Cooper, G. P. Pez, M. K. Kostov, P. Piotrowski, and S. J. Stuart, "Molecular dynamics simulations on the effects of diameter and chirality on hydrogen adsorption in single walled carbon nanotubes." *The journal of physical chemistry. B*, vol. 109, no. 9, pp. 3780–6, Mar. 2005. [Online]. Available: http://www.ncbi.nlm.nih.gov/pubmed/16851425 18

[77] P. Chen, "High H2 Uptake by Alkali-Doped Carbon Nanotubes Under Ambient Pressure and Moderate Temperatures," *Science*, vol. 285, no. 5424, pp. 91–93, Jul. 1999. [Online]. Available: http://www.sciencemag.org/cgi/doi/10.1126/science.285.5424.91 18

[78] R. T. Yang, "Hydrogen storage by alkali-doped carbon nanotubes-revisited," *Carbon*, vol. 38, no. 4, pp. 623–626, Jan. 2000. [Online]. Available: http://linkinghub.elsevier.com/retrieve/pii/S0008622399002730 18

[79] M. Yoon, S. Yang, E. Wang, and Z. Zhang, "Charged fullerenes as high-capacity hydrogen storage media." *Nano letters*, vol. 7, no. 9, pp. 2578–83, Sep. 2007. [Online]. Available: http://www.ncbi.nlm.nih.gov/pubmed/17718530 18, 96

[80] R. C. Lochan and M. Head-Gordon, "Computational studies of molecular hydrogen binding affinities: the role of dispersion forces, electrostatics, and orbital interactions." *Physical chemistry chemical physics : PCCP*, vol. 8, no. 12, pp. 1357–70, Mar. 2006. [Online]. Available: http://www.ncbi.nlm.nih.gov/pubmed/16633617 19

[81] T. Yildirim, J. Íñiguez, and S. Ciraci, "Molecular and dissociative adsorption of multiple hydrogen molecules on transition metal decorated C60," *Physical Review B*, vol. 72, no. 15, p. 153403, Oct. 2005. [Online]. Available: http://link.aps.org/doi/10.1103/PhysRevB.72.153403 19, 20

[82] M. Yoon, S. Yang, C. Hicke, E. Wang, D. Geohegan, and Z. Zhang, "Calcium as the Superior Coating Metal in Functionalization of Carbon Fullerenes for High-Capacity Hydrogen Storage," *Physical Review Letters*, vol. 100, no. 20, p. 206806, May 2008. [Online]. Available: http://link.aps.org/doi/10.1103/PhysRevLett.100.206806 19, 20

[83] K. R. S. Chandrakumar and S. K. Ghosh, "Alkali-metal-induced enhancement of hydrogen adsorption in C60 fullerene: an ab Initio study." *Nano letters*, vol. 8, no. 1, pp. 13–9, Jan. 2008. [Online]. Available: http://www.ncbi.nlm.nih.gov/pubmed/18085807 19, 20, 99

[84] W. H. Shin, S. H. Yang, W. a. Goddard, and J. K. Kang, "Ni-dispersed fullerenes: Hydrogen storage and desorption properties," *Applied Physics Letters*, vol. 88, no. 5, p. 053111, 2006. [Online]. Available: http://link.aip.org/link/APPLAB/v88/i5/p053111/s1&Agg=doi 19

[85] Q. Sun, Q. Wang, P. Jena, and Y. Kawazoe, "Clustering of Ti on a C60 surface and its effect on hydrogen storage." *Journal of the American Chemical Society*, vol. 127, no. 42, pp. 14 582–3, Oct. 2005. [Online]. Available: http://www.ncbi.nlm.nih.gov/pubmed/16231905 21

[86] Y. Li, J. Patrin, M. Chander, J. Weaver, L. Chibante, and R. Smalley, "Real-space imaging of CaxC60 using scanning tunneling microscopy," *Physical Review B*, vol. 46, no. 19, pp. 12 914–12 917, Nov. 1992. [Online]. Available: http://link.aps.org/doi/10.1103/PhysRevB.46.12914 21

[87] B. Palpant, Y. Negishi, M. Sanekata, K. Miyajima, S. Nagao, K. Judai, D. M. Rayner, B. Simard, P. a. Hackett, A. Nakajima, and K. Kaya, "Electronic and geometric properties of exohedral sodium- and gold-fullerenes," *The Journal of Chemical Physics*, vol. 114, no. 19, p. 8459, 2001. [Online]. Available: http://link.aip.org/link/JCPSA6/v114/i19/p8459/s1&Agg=doi 21

[88] S. M. Luzan, Y. O. Tsybin, and A. V. Talyzin, "Reaction of C 60 with Hydrogen Gas: In Situ Monitoring and Pathways," *The Journal of Physical Chemistry C*, vol. 115, no. 23, pp. 11 484–11 492, Jun. 2011. [Online]. Available: http://pubs.acs.org/doi/abs/10.1021/jp202715g 22, 78

[89] S. M. Luzan, Y. O. Tsybin, and A. V. Talzyin, "IN SITU MONITORING OF C 60 HYDROGENATION," in *Nanomaterials: Applications and Properties*, vol. 2, 2011, pp. 109–115. [Online]. Available: http://essuir.sumdu.edu.ua/bitstream/123456789/20618/1/19.pdf 22

[90] R. E. Haufler, J. Conceicao, L. P. F. Chibante, Y. Chai, N. E. Byrne, S. Flanagan, M. M. Haley, S. C. O'Brien, C. Pan, and . Et al., "Efficient production of C60 (buckminsterfullerene), C60H36, and the solvated buckide ion," *The Journal of Physical Chemistry*, vol. 94, no. 24, pp. 8634–8636, Nov. 1990. [Online]. Available: http://pubs.acs.org/doi/abs/10.1021/j100387a005 22, 61, 72

[91] K. Balasubramanian, "Enumeration of isomers of polysubstituted C60 and application to NMR," *Chemical Physics Letters*, vol. 182, no. 3-4, pp. 257–262, Aug. 1991. [Online]. Available: http://linkinghub.elsevier.com/retrieve/pii/000926149180211F 22

[92] B. I. Dunlap, D. W. Brenner, J. W. Mintmire, R. C. Mowrey, and C. T. White, "Geometric and electronic structures of C60H60, C60F60, and C60H36," *The Journal of Physical Chemistry*, vol. 95, no. 15, pp. 5763–5768, Jul. 1991. [Online]. Available: http://pubs.acs.org/doi/abs/10.1021/j100168a012 22, 73

[93] S. J. Austin, R. C. Batten, P. W. Fowler, D. B. Redmond, and R. Taylor, "A prediction of the structure of C60H36," *J. Chem. Soc.{,} Perkin Trans. 2*, no. 7, pp. 1383–1386, 1993. [Online]. Available: http://dx.doi.org/10.1039/P29930001383 22, 73

[94] L. E. Hall, D. R. McKenzie, M. I. Attalla, A. M. Vassallo, R. L. Davis, J. B. Dunlop, and D. J. H. Cockayne, "The structure of hydrogenated fullerene (C60H36)," *The Journal of Physical Chemistry*, vol. 97, no. 21, pp. 5741–5744, May 1993. [Online]. Available: http://pubs.acs.org/doi/abs/10.1021/j100123a046 22, 67, 73, 74, 80

[95] B. I. Dunlap, D. W. Brenner, and G. W. Schriver, "Symmetric Isomers of Hydrofullerene C60H36," *The Journal of Physical Chemistry*, vol. 98, no. 7, pp. 1756–1757, Feb. 1994. [Online]. Available: http://pubs.acs.org/doi/abs/10.1021/j100058a006 22, 81, 96

[96] L. E. Hall, D. R. McKenzie, R. L. Davis, M. I. Attalla, and a. M. Vassallo, "Structural Determination of the Hydrofullerene C60D36 by Neutron Diffraction," *Acta Crystallographica Section B Structural Science*, vol. 54, no. 3, pp. 345–350, Jun. 1998. [Online]. Available: http://scripts.iucr.org/cgi-bin/paper?S0108768198000093 22, 61, 67, 74, 80, 81, 83

[97] A. V. Okotrub, L. G. Bulusheva, I. P. Asanov, A. S. Lobach, and Y. M. Shulga, "X-ray Spectroscopic and Quantum-Chemical Characterization of Hydrofullerene C 60 H 36," *The Journal of Physical Chemistry A*, vol. 103, no. 6, pp. 716–720, Feb. 1999. [Online]. Available: http://pubs.acs.org/doi/abs/10.1021/jp983043z 22

[98] J. Nossal, R. K. Saini, A. K. Sadana, H. F. Bettinger, L. B. Alemany, G. E. Scuseria, W. E. Billups, M. Saunders, A. Khong, and R. Weisemann, "Formation, Isolation, Spectroscopic Properties, and Calculated Properties of Some Isomers of C 60 H 36," *Journal of the American Chemical Society*, vol. 123, no. 35, pp. 8482–8495, Sep. 2001. [Online]. Available: http://pubs.acs.org/doi/abs/10.1021/ja010818022

[99] A. a. Gakh, A. Y. Romanovich, and A. Bax, "Thermodynamic Rearrangement Synthesis and NMR Structures of C 1 , C 3 , and T Isomers of C 60 H 36," *Journal of the American Chemical Society*, vol. 125, no. 26, pp. 7902–7906, Jul. 2003. [Online]. Available: http://www.ncbi.nlm.nih.gov/pubmed/12823010http://pubs.acs.org/doi/abs/10.1021/ja035332t 22

[100] J. A. Teprovich, M. S. Wellons, R. Lascola, S.-j. Hwang, P. A. Ward, R. N. Compton, and R. Zidan, "Synthesis and characterization of a lithium-doped fullerane (Li(x)-C60-H(y)) for reversible hydrogen storage." *Nano letters*, vol. 12, no. 2, pp. 582–9, Mar. 2012. [Online]. Available: http://www.ncbi.nlm.nih.gov/pubmed/22206302 22, 63, 64, 69, 78, 80, 99

[101] J. A. Teprovich, D. A. Knight, M. S. Wellons, and R. Zidan, "Catalytic effect of fullerene and formation of nanocomposites with complex hydrides: NaAlH4 and LiAlH4," *Journal of Alloys and Compounds*, vol. 509, pp. S562–S566, Sep. 2011. [Online]. Available: http://linkinghub.elsevier.com/retrieve/pii/S0925838810025211 23

[102] T. Hahn, Ed., *International Tables for Crystallography, vol. A (SPACE-GROUP SYMMETRY)*, fifth edit ed. SPRINGER, 2002. 24

[103] A. C. Larson and R. B. V. Dreele, "General Structure Analysis System (GSAS)," *Los Alamos National Laboratory Report LAUR 86-748*, 2004. 27

[104] P. Fischer, G. Frey, M. Koch, M. Könnecke, V. Pomjakushin, J. Schefer, R. Thut, N. Schlumpf, R. Bürge, U. Greuter, S. Bondt, and E. Berruyer, "High-resolution powder diffractometer HRPT for thermal neutrons at SINQ," *Physica B: Condensed Matter*, vol. 276-278, pp. 146–147, Mar. 2000. [Online]. Available: http://linkinghub.elsevier.com/retrieve/pii/S092145269901399X 29, 42

[105] T. C. Hansen, P. F. Henry, H. E. Fischer, J. Torregrossa, and P. Convert, "The D20 instrument at the ILL: a versatile high-intensity two-axis neutron diffractometer," *Measurement Science and Technology*, vol. 19, no. 3, p. 034001, Mar. 2008. [Online]. Available: http://stacks.iop.org/0957-0233/19/i=3/a=034001?key=crossref.b4899607c4d372db5e0060580ce3a5af 29

[106] P. Juhás, T. Davis, C. L. Farrow, and S. J. L. Billinge, "PDFgetX3 : a rapid and highly automatable program for processing powder diffraction data into total scattering pair distribution functions," *Journal of Applied Crystallography*, vol. 46, no. 2, pp. 560–566, Mar. 2013. [Online]. Available: http://scripts.iucr.org/cgi-bin/paper?S0021889813005190 31, 79

[107] C. L. Farrow, P. Juhas, J. W. Liu, D. Bryndin, E. S. Bozin, J. Bloch, T. Proffen, and S. J. L. Billinge, "PDFgui user guide," no. April, 2009. [Online]. Available: http://totalscattering.lanl.gov/tutorial/docs/pdfgui.pdf 31, 81

[108] S. J. Billinge and M. F. Thorpe, *Local Structure from Diffraction*, M. F. Thorpe, Ed. KLUWER ACADEMIC PUBLISHERS, 2002. [Online]. Available: http://www.springer.com/materials/characterization+%26+evaluation/book/978-0-306-45827-9 31

[109] T. Egami and S. J. Billinge, "UNDERNEATH THE BRAGG PEAKS Structural Analysis of Complex Materials," *Pergamon Materials Series*, vol. 7, pp. 3–404, 2003. [Online]. Available: http://www.sciencedirect.com/science/bookseries/14701804/7 31

[110] I.-K. Jeong, R. Heffner, M. Graf, and S. Billinge, "Lattice dynamics and correlated atomic motion from the atomic pair distribution function," *Physical Review B*, vol. 67, no. 10, p. 104301, Mar. 2003. [Online]. Available: http://link.aps.org/doi/10.1103/PhysRevB.67.104301 31

[111] a. Sartbaeva, S. Wells, M. Thorpe, E. Božin, and S. Billinge, "Quadrupolar Ordering in LaMnO3 Revealed from Scattering Data and Geometric Modeling," *Physical Review Letters*, vol. 99, no. 15, p. 155503, Oct. 2007. [Online]. Available: http://link.aps.org/doi/10.1103/PhysRevLett.99.155503 31

[112] V. Petkov, "Nanostructure by high-energy X-ray diffraction," *Materials Today*, vol. 11, no. 11, pp. 28–38, Nov. 2008. [Online]. Available: http://dx.doi.org/10.1016/S1369-7021(08)70236-0http://linkinghub.elsevier.com/retrieve/pii/S1369702108702360 31

[113] M. Bielmann, S. Kato, P. Mauron, A. Borgschulte, and A. Züttel, "Characterization of hydrogen storage materials by means of pressure concentration isotherms based on the mass flow method." *The Review of scientific instruments*, vol. 80, no. 8, p. 083901, Aug. 2009. [Online]. Available: http://www.ncbi.nlm.nih.gov/pubmed/19725661 32, 43, 55

[114] D. E. Groom, "Lepton summary table," *The European Physical Journal C*, vol. 15, no. 1-4, pp. 23–25, Mar. 2000. [Online]. Available: http://www.springerlink.com/index/10.1007/BF02683391 34

[115] S. F. J. Cox, "Muonium as a model for interstitial hydrogen in the semiconducting and semimetallic elements," *Reports on Progress in Physics*, vol. 72, no. 11, p. 116501, Nov. 2009. [Online]. Available: http://stacks.iop.org/0034-4885/72/i=11/a=116501?key=crossref.ce6d2acc8d75ace555b554ef00e9e661 38, 97

[116] A. Schenck, *Muon spin rotation spectroscopy*, 1985. [Online]. Available: http://books.google.it/books?id=b6dPAQAAIAAJ 41, 89

[117] P. Heiney, J. Fischer, A. McGhie, W. Romanow, A. Denenstein, J. McCauley Jr., A. Smith, and D. Cox, "Orientational ordering transition in solid C_{60}," *Physical Review Letters*, vol. 66, no. 22, pp. 2911–2914, Jun. 1991. [Online]. Available: http://link.aps.org/doi/10.1103/PhysRevLett.66.2911 44

[118] L. Akselrod, H. Byrne, C. Thomsen, and S. Roth, "Reversible photochemical processes in fullerenes. A Raman study," *Chemical Physics Letters*, vol. 215, no. 1-3, pp. 131–136, Nov. 1993. [Online]. Available: http://linkinghub.elsevier.com/retrieve/pii/000926149389275M 46

[119] T. Wå gberg, P. Stenmark, and B. Sundqvist, "Structural aspects of two-dimensional polymers: Li4C60, Na4C60 and tetragonal C60. Raman spectroscopy and X-ray diffraction," *Journal of Physics and Chemistry of Solids*, vol. 65, no. 2-3, pp. 317–320, Mar. 2004. [Online]. Available: http://linkinghub.elsevier.com/retrieve/pii/S0022369703004128 48

[120] Y. Chen, F. Stepniak, J. Weaver, L. Chibante, and R. Smalley, "Fullerides of alkaline-earth metals," *Physical Review B*, vol. 45, no. 15, pp. 8845–8848, Apr. 1992. [Online]. Available: http://link.aps.org/doi/10.1103/PhysRevB.45.8845 49

[121] A. P. Hammersley, "FIT2D V10.3 Reference Manual V4.0," Tech. Rep., 1998. [Online]. Available: http://www.csb.yale.edu/userguides/datamanip/fit2d/fit2d_ref.pdf 50

[122] P. Mauron, A. Remhof, A. Bliersbach, A. Borgschulte, A. Züttel, D. Sheptyakov, M. Gaboardi, M. Choucair, D. Pontiroli, M. Aramini, A. Gorreri, and M. Riccò, "Reversible hydrogen absorption in sodium intercalated fullerenes," *International Journal of Hydrogen Energy*, vol. 37, no. 19, pp. 14 307–14 314, Oct. 2012. [Online]. Available: http://linkinghub.elsevier.com/retrieve/pii/S0360319912016229 57, 58, 60, 63, 68, 71, 91

[123] W. Andreoni, P. Giannozzi, J. F. Armbruster, M. Knupfer, and J. Fink, "Anomalous electronic behaviour of Na superfullerides: theory and experiment," *Europhysics Letters (EPL)*, vol. 34, no. 9, pp. 699–704, Jun. 1996. [Online]. Available: http://stacks.iop.org/0295-5075/34/i=9/a=699?key=crossref.823175e56fb22e53d486b43d06b7aff4 56

[124] D. V. Schur, S. Y. Zaginaichenko, A. F. Savenko, V. a. Bogolepov, N. S. Anikina, A. Zolotarenko, Z. a. Matysina, T. N. Veziroglu, and N. E. Skryabina, "Experimental evaluation of total hydrogen capacity for fullerite C60," *International Journal of Hydrogen Energy*, vol. 36, no. 1, pp. 1143–1151, Jan. 2011. [Online]. Available: http://linkinghub.elsevier.com/retrieve/pii/S0360319910012681 57

[125] L. Cristofolini, P. Facci, and M. Fontana, "Lithium diffusion and C_ {60} dynamics by quasielastic and inelastic neutron scattering in Li_ {12} C_ {60} fulleride," *Physical Review B*, vol. 61, no. 5, pp. 3404–3409, 2000. [Online]. Available: http://prb.aps.org/abstract/PRB/v61/i5/p3404_1 63

[126] P. Mauron, M. Gaboardi, A. Remhof, A. Bliersbach, D. Sheptyakov, M. Aramini, G. Vlahopoulou, F. Giglio, D. Pontiroli, M. Riccò, and A. Züttel, "Hydrogen Sorption in Li 12 C 60," *The Journal of Physical Chemistry C*, vol. 117, no. 44, pp. 22 598–22 602, Nov. 2013. [Online]. Available: http://pubs.acs.org/doi/abs/10.1021/jp408652t 67, 68, 76, 77

[127] M. I. Attalla, A. M. Vassallo, B. N. Tattam, and J. V. Hanna, "Preparation of hydrofullerenes by hydrogen radical induced hydrogenation," *The Journal of Physical Chemistry*, vol. 97, no. 24, pp. 6329–6331, Jun. 1993. [Online]. Available: http://pubs.acs.org/doi/abs/10.1021/j100126a001 73

[128] E. Lide, D. R., *CRC Handbook of Chemistry and Physics, 89th Edition (Internet Version)*, F. CRC Press/Taylor and Francis: Boca Raton, Ed., Jul. 2009, vol. 15, no. 3. 74, 75

[129] R. T. Azuah, L. R. Kneller, Y. Qiu, P. L. W. Tregenna-Piggott, C. M. Brown, J. R. D. Copley, and R. M. Dimeo, "DAVE: A Comprehensive Software Suite for the Reduction, Visualization, and Analysis of Low Energy Neutron Spectroscopic Data," *Journal of Research of the National Institute of Standards and Technology*, vol. 114, no. 6, p. 341, Nov. 2009. [Online]. Available: http://nvlpubs.nist.gov/nistpubs/jres/114/6/V114.N06.A04.pdf 75

[130] A. D. Darwish, A. K. Abdul-Sada, G. J. Langley, H. W. Kroto, R. Taylor, and D. R. M. Walton, "Polyhydrogenation of [60]- and [70]-fullerenes," *Journal of the Chemical Society, Perkin Transactions 2*, no. 12, p. 2359, 1995. [Online]. Available: http://xlink.rsc.org/?DOI=p29950002359 78

[131] J. Brewer, D. Beder, and D. Spencer, "Quadrupole Splitting of Muonium Precession in α-Quartz," *Physical Review Letters*, vol. 42, no. 12, pp. 808–811, Mar. 1979. [Online]. Available: http://link.aps.org/doi/10.1103/PhysRevLett.42.808 84

[132] S. F. J. Cox, S. P. Cottrell, M. Charlton, P. A. Donnelly, C. Ewels, M. Heggie, and B. Hourahine, "A molecular radical model for hydrogen and muonium in graphite," *Journal of Physics: Condensed Matter*, vol. 13, no. 10, pp. 2169–2175, Mar. 2001. [Online]. Available: http://stacks.iop.org/0953-8984/13/i=10/a=312?key=crossref.7e833020a9e48ada20e5c20cbac5212e 84

[133] W. G. Williams, S. R. Brown, and S. P. Cottrell, "Muon implantation in alkali metal hydrides," *Hyperfine Interactions*, vol. 106, no. 1-4, pp. 105–110, 1997. [Online]. Available: http://link.springer.com/article/10.1023/A:1012625504691 84

[134] R. Kiefl, J. Schneider, A. MacFarlane, K. Chow, T. Duty, T. Estle, B. Hitti, R. Lichti, E. Ansaldo, C. Schwab, P. Percival, G. Wei, S. Wlodek, K. Kojima, W. Romanow, J. McCauley, N. Coustel, J. Fischer, and A. Smith, "Molecular dynamics of

μˆ{+}-C_{60} radical in solid C_{60},” *Physical Review Letters*, vol. 68, no. 9, pp. 1347–1350, Mar. 1992. [Online]. Available: http://link.aps.org/doi/10.1103/PhysRevLett.68.1347 84, 88, 94

[135] W. Liu, M. Boshier, S. Dhawan, O. van Dyck, P. Egan, X. Fei, M. Grosse Perdekamp, V. Hughes, M. Janousch, K. Jungmann, D. Kawall, F. Mariam, C. Pillai, R. Prigl, G. zu Putlitz, I. Reinhard, W. Schwarz, P. Thompson, and K. Woodle, “High Precision Measurements of the Ground State Hyperfine Structure Interval of Muonium and of the Muon Magnetic Moment,” *Physical Review Letters*, vol. 82, no. 4, pp. 711–714, Jan. 1999. [Online]. Available: http://link.aps.org/doi/10.1103/PhysRevLett.82.711 84

[136] W. MacFarlane, R. Kiefl, S. Dunsiger, J. Sonier, J. Chakhalian, J. Fischer, T. Yildirim, and K. Chow, “Muon-spin-relaxation studies of the alkali-fulleride superconductors,” *Physical Review B*, vol. 58, no. 2, pp. 1004–1024, Jul. 1998. [Online]. Available: http://link.aps.org/doi/10.1103/PhysRevB.58.1004 85, 88, 93

[137] M. Aramini, M. Gaboardi, G. Vlahopoulou, D. Pontiroli, C. Cavallari, C. Milanese, and M. Riccò, “Muon spin relaxation reveals the hydrogen storage mechanism in light alkali metal fullerides,” *Carbon*, vol. 7, pp. 2–7, Oct. 2013. [Online]. Available: http://linkinghub.elsevier.com/retrieve/pii/S0008622313009172 85

[138] F. L. Pratt, “Repolarization of anisotropic muonium in orientationally disordered solids,” *Philosophical Magazine Letters*, vol. 75, no. 6, pp. 371–380, Jun. 1997. [Online]. Available: http://www.tandfonline.com/doi/abs/10.1080/095008397179444 88

[139] E. Roduner and J. C. Walton, “The positive muon as a probe in free radical chemistry,” *Magnetic Resonance in Chemistry*, vol. 27, no. 5, pp. 507–507, May 1989. [Online]. Available: http://doi.wiley.com/10.1002/mrc.1260270518 89

[140] E. J. Ansaldo, C. Niedermayer, and C. E. Stronach, "Muonium in fullerite," *Nature*, vol. 353, no. 6340, pp. 121–121, Sep. 1991. [Online]. Available: http://www.nature.com/doifinder/10.1038/353121a0 90

[141] S. Cottrell, J. Lord, and W. Williams, "Muon charge state and dynamics in the alkali metal hydrides," *Physica B: Condensed Matter*, vol. 289-290, pp. 570–573, Aug. 2000. [Online]. Available: http://linkinghub.elsevier.com/retrieve/pii/S0921452600002593 93

[142] M. Pozzo and D. Alfè, "Hydrogen dissociation and diffusion on transition metal (=Ti, Zr, V, Fe, Ru, Co, Rh, Ni, Pd, Cu, Ag)-doped Mg(0001) surfaces," *International Journal of Hydrogen Energy*, vol. 34, no. 4, pp. 1922–1930, Feb. 2009. [Online]. Available: http://linkinghub.elsevier.com/retrieve/pii/S0360319908015516 95

[143] A. S. Lobach, B. P. Tarasov, Y. M. Shul'ga, A. A. Perov, and A. N. Stepanov, "Reaction of D2 with palladium fulleride C60Pd4.9," *Russian Chemical Bulletin*, vol. 45, no. 2, pp. 464–465, Feb. 1996. [Online]. Available: http://link.springer.com/10.1007/BF01433997 95

[144] Y. Lin, F. Ding, and B. I. Yakobson, "Hydrogen storage by spillover on graphene as a phase nucleation process," *Physical Review B*, vol. 78, no. 4, p. 041402, Jul. 2008. [Online]. Available: http://link.aps.org/doi/10.1103/PhysRevB.78.041402 96

[145] M. Kosaka, K. Tanigaki, K. Prassides, S. Margadonna, A. Lappas, C. Brown, and A. Fitch, "Superconductivity in LixCsC60 fullerides," *Physical Review B*, vol. 59, no. 10, pp. R6628–R6630, Mar. 1999. [Online]. Available: http://link.aps.org/doi/10.1103/PhysRevB.59.R6628 96

[146] K. L. Akers and M. Moskovits, "Raman spectra and electrical resistivity measurements of KxC60 (x = 0,3 and 6) thin films," *Journal of Electron Spectroscopy and Related Phenomena*, vol. 64-65, pp. 871–876, Dec. 1993. [Online]. Available: http://linkinghub.elsevier.com/retrieve/pii/036820489380162F 97

[147] M. Riccò, D. Pontiroli, M. Mazzani, M. Choucair, J. A. Stride, and O. V. Yazyev, "Muons probe strong hydrogen interactions with defective graphene." *Nano letters*, vol. 11, no. 11, pp. 4919–22, Nov. 2011. [Online]. Available: http://www.ncbi.nlm.nih.gov/pubmed/21988328 97

Acknowledgments

Thanks are due to my supervisor, Prof. Mauro Riccò, for teaching me the way of scientific research (at least you tried).

I acknowledge the financial support of the SNSF Sinergia HyCarbo project and of the IRSES Mag-Non-Mag project.

Many thanks to Daniele Pontiroli, big man in a little world, for putting up with me all this time. Thanks to Matteo Aramini and his dark humor, able to alleviate (worsen, sometimes) the more dramatic situations. Thanks to all my laboratory-mates, for every dis/adventure we had: especially to Sandra Gorreri, Marcello Mazzani, Moahmmad Choucair (for offering me a Lebanese breakfast in Australia) and Gina Vlahopoulou (for having set up the coffee break).

Many thanks to all my external collaborators, in particular Philippe Mauron, Andreas Bliersbach (for every virtual beer), Chiara Cavallari, Chiara Milanese and Giovanni Bertoni.

A great thanks to Sara, the only one able to hold off my cynicism.

I wish to thank my officemates of Area 51, for countless distractions and useful discussions (but above all distractions): Elena, Giacomo, Pietro, Ale and Titti. Thanks are due to Chiara Pernechele for her assistance in the SQuID laboratory.

Thanks to all the coffee machines I had the pleasure to meet.

Finally, I wish to express my gratitude and thanks to my family for having trust in me for all these years.